

FOURIER-BASED IMAGE SHARPNESS SENSOR FOR ADAPTIVE OPTICS  
CORRECTION

by

Kristin Nicole Walker

A dissertation submitted to the faculty of  
The University of North Carolina at Charlotte  
in partial fulfillment of the requirements  
for the degree of Doctor of Philosophy in  
Optical Science and Engineering

Charlotte

2009

Approved by:

---

Dr. Robert K. Tyson

---

Dr. Michael A. Fiddy

---

Dr. Gregory J. Gbur

---

Dr. Susan R. Trammell

---

Dr. Susan M. Sell

©2009  
Kristin Nicole Walker  
ALL RIGHTS RESERVED

## ABSTRACT

KRISTIN NICOLE WALKER. Fourier-based image sharpness sensor for adaptive optics correction. (Under the direction of DR. ROBERT K. TYSON)

Adaptive optics reduces undesirable turbulence effects present during propagation and imaging through the atmosphere or another random medium. Within an adaptive optics system, wavefront sensing determines the incoming wavefront errors. Image sharpening is one method of wavefront sensing where the sharpness value is measured from the image intensity based on a given sharpness metric. The wavefront correction device is then perturbed until the sharpness value is maximized. The key to image sharpening is defining sharpness with a sharpness metric that reaches a maximum when wavefront error is zero.

Present image sharpness metrics often use the image intensity. In contrast, this dissertation introduces four novel sharpness metrics based on the Fourier transform of the image. Since high spatial frequencies carry information about the image's edges and fine details, taking the Fourier transform and maximizing the high spatial frequencies sharpens the image. Coherence of the illumination source and the sharpness metric choice determine which of the presented optical system configurations to use.

Performances of the Fourier-based sharpness metrics are observed and compared by measuring the sharpness value while adding defocus to the system. If the sharpness value reaches a maximum with zero wavefront error then the sharpness metric is successful. This investigation continues by adding astigmatism, coma, and spherical aberration and measuring the sharpness value to see the affect of these higher order aberrations. The sharpness metrics are then implemented into a simple manual closed-loop correction system. This dissertation presents successful performance results of these novel Fourier-based sharpness metrics showing great promise for use in adaptive optics correction.

## ACKNOWLEDGMENTS

First I would like to acknowledge my advisor, Dr. Bob Tyson, for posing the question that led to this dissertation topic and for offering excellent instruction and guidance along the way. Thank you for providing opportunities outside of the lab to attend, present, and network at several conferences, especially the one held in Ireland. Thank you for making this research experience pleasant and instructive.

To Dr. Mike Fiddy, Dr. Greg Gbur, Dr. Susan Trammell, and Dr. Susan Sell; I thank you for providing thoughtful insight and serving on my committee.

I would like to thank Mikhail Loktev and Oleg Soloviev from OKO Flexible Optical for their technical support in setting up the OKO deformable mirror and the wavefront sensor.

In addition, I would like to thank the Giles Foundation for providing financial support this past year through the dissertation year fellowship.

I truly appreciate the faculty and graduate students of the Department of Physics and Optical Science at UNCC who have provided many resources along the way. I would like to thank my professors for sharing their vision and passion for optics as they have instructed and inspired me inside and outside of the classroom. To my classmates I thank you for all the help and collaboration through classes, research, and SPIE student chapter activities. Thank you for contributing to my graduate experience by developing nontechnical skills including student chapter budgeting, teamwork, event planning, and outreach experiences.

I am extremely grateful to my parents and my two brothers for their continual support and encouragement over the years. Thank you for loving me and shaping me into

who I am today. I also want to thank my biological extended family and the extended families that have adopted me at Mint Hill and CIF. Thank you for the extended care and encouragement you have provided. To the many friends who have walked with me along the way, I owe special thanks for bringing much joy and much needed diversions during times of stress and frustration. To all my family and friends, thank you for listening to my research discussion. It is all your love and understanding, and the strength and drive that comes from my heavenly Father, that has given me the ability to complete this work.

## TABLE OF CONTENTS

LIST OF FIGURES	ix
LIST OF TABLES	xi
CHAPTER 1: INTRODUCTION	1
1.1 Motivation	1
1.2 Objectives	2
CHAPTER 2: INTRODUCTION TO ADAPTIVE OPTICS	3
2.1 Introduction	3
2.1 Adaptive Optics System Components	4
2.3 Brief History of Adaptive Optics	5
2.4 Applications	7
CHAPTER 3: ADAPTIVE OPTICS PRINCIPLES	10
3.1 Aberration Representation with Zernike Polynomials	10
3.2 Wavefront Sensors	11
3.3 Wavefront Correction	13
3.4 Measurement of Optical Quality and Image Evaluation	14
CHAPTER 4: IMAGE SHARPENING	16
4.1 Introduction	16
4.2 History of Image Sharpening	17
4.3 Advantages of Image Sharpening	20
CHAPTER 5: THEORY	21
5.1 Introduction	21
5.2 Scalar Diffraction Theory	22

5.2.1	Fresnel Diffraction	24
5.2.2	Fraunhofer Diffraction	26
5.3	Fourier Transforming Property of a Single Lens	27
5.4	Imaging Using Linear Systems Theory	31
5.4.1	Coherent Imaging System	32
5.4.2	Incoherent Imaging System	33
5.5	Spatial Filtering	34
CHAPTER 6: FOURIER-BASED IMAGE SHARPNESS SENSOR		37
6.1	Introduction	37
6.2	Image Sharpness Sensor Configuration	38
6.3	Sharpness Metrics	38
6.4	Optical Components	43
6.5	Search Algorithm	45
CHAPTER 7: PERFORMANCE OF THE FOURIER-BASED IMAGE SHARPNESS SENSOR IN INCOHERENT IMAGING		46
7.1	Introduction	46
7.2	Sharpness Metrics	46
7.3	System Configuration	47
7.4	Sharpness versus Defocus Experimental Results	51
7.4.1	Optics Table Experimental Results	54
7.4.2	Telescope Experimental Results	59
7.4.3	Summary	68
7.5	Sharpness versus higher order aberrations	69
7.6	Performance in a closed-loop system	75

7.7	Conclusions	81
CHAPTER 8: PERFORMANCE OF THE FOURIER-BASED IMAGE SHARPNESS SENSOR IN COHERENT IMAGING		82
8.1	Introduction	82
8.2	Sharpness Metrics	82
8.3	Optical System Configurations	84
8.4	Sharpness versus Defocus Experimental Results	89
8.4.1	Camera at the Image Plane	89
8.4.2	Camera at the Fourier Plane	95
8.4.3	Physical mask at the Fourier plane	100
8.4.4	Summary	102
8.5	Sharpness versus higher order aberrations	104
8.5.1	Camera at the Image Plane	104
8.5.2	Camera at the Fourier Plane	108
8.5.3	Physical mask at the Fourier plane	110
8.6	Performance in a closed-loop system	112
8.7	Conclusions	114
CHAPTER 9: CONCLUSIONS		116
9.1	Discussion	116
9.2	Future Work	117
REFERENCES		119



## LIST OF FIGURES

FIGURE 2.1: Adaptive Optics System	5
FIGURE 3.1: Adaptive Optics System with Direct and Indirect Wavefront Sensing	12
FIGURE 4.1: Image Sharpening Adaptive Optics System	17
FIGURE 5.1: Point-source Illumination of a Plane Screen	23
FIGURE 5.2: Diffraction Geometry for Fresnel Diffraction	25
FIGURE 5.3: Thickness Function of a Lens	27
FIGURE 5.4: Configuration for the transforming property of a single lens	29
FIGURE 5.5: 4-F system; light incident on the object is a plane wave of coherent and monochromatic light	35
FIGURE 5.6: Spatial filtering using a 4-f system. (a) image plane, (b) Fourier plane, (c) image plane with a low-pass filter at the Fourier plane, and (d) image plane with a high-pass filter at the Fourier plane	36
FIGURE 6.1: Image Sharpness Sensor Configuration	37
FIGURE 6.2: MTF cross-section plots with varying aberration strengths of (a) defocus, (b) astigmatism, (c) coma, and (d) spherical aberration	41
FIGURE 6.3: AgilOptics Deformable Mirror Profile	44
FIGURE 6.4: AgilOptics Actuator Array	44
FIGURE 7.1: Experimental schematic with an incoherent source and the camera at the image plane. All numbers are in units of millimeters.	49
FIGURE 7.2: Optics table experimental setup. Incoherent LED source with the camera at the image plane.	49
FIGURE 7.3: Telescope experimental setup with a Celestron NexStar 11 inch telescope and a CCD camera mounted at the image plane.	50
FIGURE 7.4: Experimental schematic with the added Shack Hartmann wavefront sensor.	52

FIGURE 7.5: Telescope images of the UNC Charlotte logo with the telescope at (a) defocus and (b) focus	60
FIGURE 8.1: Experimental schematic with a coherent source and the camera at the image plane. All numbers are in units of millimeters.	85
FIGURE 8.2: Optics table experimental setup. Coherent HeNe laser source with the camera located at the image plane.	85
FIGURE 8.3: Experimental schematic with a coherent source and the camera at the Fourier plane. All numbers are in units of millimeters.	86
FIGURE 8.4: Optics table experimental setup. Coherent HeNe laser source with the camera located at the Fourier plane.	87
FIGURE 8.5: Experimental schematic with a coherent source and high-pass mask at the Fourier plane. Cameras are located at the image planes to capture the spatially filtered image and the normal image. All numbers are in units of mm.	88
FIGURE 8.6: Optics table setup of the spatially filtering configuration	88
FIGURE 8.7: Image plane captured images of the spatially filtered high frequency bar chart object at (a) focus and (b) defocus	100

## LIST OF TABLES

TABLE 3.1: Zernike Polynomials	11
TABLE 4.1: Image Sharpness Metric Definitions and Performances	18
TABLE 6.1: CCD Camera Specifications	43
TABLE 6.2: Deformable Mirror Specifications	45
TABLE 7.1: Image plane intensity distributions and digital Fourier transforms on linear and logarithmic scales for an incoherent source and optics table setup.	53
TABLE 7.2: $S_2$ mask sensitivity for the medium frequency bar chart object illuminated with an incoherent source and optics table setup.	57
TABLE 7.3: Sharpness vs. defocus plots for an incoherent source and optics table setup. Comparison of the three image plane sharpness metrics. $S_2$ uses a mask size of 20 pixels.	58
TABLE 7.4: $S_2$ sharpness vs. defocus plots with various mask sizes for the UNC Charlotte logo object with the telescope setup.	60
TABLE 7.5.: Sharpness vs. defocus plots for 22 extended objects. Comparison of the three sharpness metrics. $S_2$ uses a mask size of 5 pixels.	65
TABLE 7.6: Telescope images of the incoherent point sources at focus.	67
TABLE 7.7: Sharpness vs. defocus plots for the incoherent point source with the telescope setup. Comparison of the three image plane sharpness metrics. $S_2$ uses a mask size of 5 pixels.	68
TABLE 7.8: Computing times of the three image plane sharpness metrics.	69
TABLE 7.9: Sharpness vs. astigmatism plots for an incoherent source and optics table setup. Comparison of the three image plane sharpness metrics. $S_2$ uses a mask size of 20 pixels.	72
TABLE 7.10: Sharpness vs. coma plots for an incoherent source and optics table setup. Comparison of the three image plane sharpness metrics. $S_2$ uses a mask size of 20 pixels.	73
TABLE 7.11: Sharpness vs. spherical aberration plots for an incoherent source and optics table setup. Comparison of the three image plane sharpness metrics. $S_2$ uses a mask size of 20 pixels.	75

TABLE 7.12: Closed-loop images for the high frequency bar chart object on the optics table with an incoherent source. Mask size of 20 pixels used for $S_2$ .	77
TABLE 7.13: Closed-loop images of brick located at a distance of about 60 m taken with the telescope. Image plane sharpness metrics used. Mask size of 5 pixels used for $S_2$ .	78
TABLE 7.14: Closed-loop images of trees located at a distance of about 300 m taken with the telescope. Image plane sharpness metrics used. Mask size of 5 pixels used for $S_2$ .	79
TABLE 7.15: Closed-loop images of a window located at a distance of about 1 km taken with the telescope. Image plane sharpness metrics used. Mask size of 5 pixels used for $S_2$ .	80
TABLE 8.1: $S_2$ mask sensitivity for the medium frequency bar chart object illuminated by a coherent source.	91
TABLE 8.2: Sharpness vs. defocus plots for a coherent source and optics table setup. Comparison of the three image plane sharpness metrics. $S_2$ uses a mask size of 5 pixels.	93
TABLE 8.3: Images of the coherent point sources at a distance of 90 taken with the telescope.	94
TABLE 8.4: Sharpness vs. defocus plots for coherent point sources with the telescope setup. Comparison of the three image plane sharpness metrics. $S_2$ uses a mask size of 5 pixels.	94
TABLE 8.5: $S_3$ mask sensitivity for the medium frequency bar chart object illuminated by a coherent source.	97
TABLE 8.6: Sharpness vs. defocus plots for a coherent source and optics table setup. Use of the $S_3$ sharpness metric with mask sizes of 15 and 20 pixels.	99
TABLE 8.7: Sharpness vs. defocus plots for a coherent source and optics table setup using the $S_4$ sharpness metric.	102
TABLE 8.8: Computing time of the sharpness metrics.	104
TABLE 8.9: Sharpness vs. astigmatism plots for a coherent source and optics table setup. Comparison of the three image plane sharpness metrics. $S_2$ uses a mask size of 20 pixels.	106

TABLE 8.10: Sharpness vs. coma plots for a coherent source and optics table setup. Comparison of the three image plane sharpness metrics. $S_2$ uses a mask size of 20 pixels.	107
TABLE 8.11: Sharpness vs. spherical aberration plots for a coherent source and optics table setup. Comparison of the three image plane sharpness metrics. $S_2$ uses a mask size of 20 pixels.	108
TABLE 8.12: Sharpness vs. aberration strength plots for a coherent source and optics table setup with all higher order aberrations. Use of sharpness metric $S_2$ with a mask size of 20 pixels (10 pixels for circle object).	110
TABLE 8.13: Sharpness vs. aberration strength plots for a coherent source and optics table setup with all higher order aberrations. Sharpness metric $S_4$ was used.	112
TABLE 8.14: Closed-loop images of the high frequency object using the image plane sharpness metrics. Mask size of 5 pixels used for $S_2$ .	113
TABLE 8.15: Closed-loop images of the high frequency object using sharpness metric $S_3$ . Mask sizes of 15 and 20 pixels were used.	114

## CHAPTER 1: INTRODUCTION

### 1.1 Motivation

Image sharpening is one method of wavefront sensing within adaptive optics where the sharpness value is measured from the image intensity based on a given sharpness metric. The wavefront correction device, such as a deformable mirror, is then perturbed until sharpness is maximized. Image sharpening is advantageous in fields where optical components need to be minimized for space and cost constraints. Since no additional wavefront sensing equipment is needed, sharpness measurements can be made using the camera already present to capture images. In image sharpening, one key factor is selecting a sharpness metric, or sharpness definition, that reaches an absolute maximum with zero wavefront error.

Image sharpening has been successfully used in adaptive optics correction. Present image sharpness metrics often use the image intensity to calculate the sharpness value. The motivation of this research is to create and develop sharpness metrics based on the Fourier spectrum of the image and to implement in a closed-loop adaptive optics system. The Fourier transform of the image can be generated digitally from the captured image or optically, and essentially instantaneously, by using the Fourier transforming property of a single lens. This dissertation introduces four novel sharpness metrics based on the Fourier transform of the image.

## 1.2 Objectives

The main objectives of this dissertation project are to develop Fourier-based sharpness metrics, investigate the performance of these metrics with added aberrations, and to demonstrate their feasibility in a closed-loop adaptive optics system. This dissertation investigates both incoherent and coherent imaging system configurations.

Chapters 2 through 5 present the background and theory information related to the Fourier-based sharpness metrics. This leads up to chapter 6 introducing the Fourier-based image sharpness sensor and all the components required, including the sharpness metrics. Results and discussion for the sharpness metric performance investigations are presented in two chapters based on if the imaging system is incoherent (chapter 7) or coherent (chapter 8). Calculations of the sharpness value for a given sharpness metric as aberrations are added to the system determines the performance of the metric, first with defocus and later with the addition of higher order aberrations. For a given imaging configuration, object type, and aberration, the sharpness value is calculated and plotted versus aberration strength to determine if the sharpness value is maximum when wavefront error is zero. Performance and sensitivity of each metric are determined from these plots and then compared to the other sharpness metrics. Feasibility of the sharpness metrics in a closed-loop adaptive optics system is found by implementing the metrics in a preliminary, simple, and manual closed-loop system.

## CHAPTER 2: INTRODUCTION TO ADAPTIVE OPTICS

### 2.1 Introduction

Atmospheric temperature fluctuations and wind velocities cause variations in the refractive index which alters the optical beam path of light propagating through the atmosphere. Astronomical seeing and atmospheric propagation are limited by turbulence effects including scintillation, beam wander, and beam broadening. Adaptive optics counters these effects through a closed-loop optical system correcting in real-time the distortions caused by propagating light through a turbulent medium such as the atmosphere. Post-processing techniques to restore and enhance degraded images by methods including deconvolution<sup>1</sup> are not considered adaptive optics because they do not correct in real-time. Adaptive optics is not equivalent to, but a subset of active optics. Active optics consists of any method of controlling the beam or path of light over time such as correcting for telescope aberrations and misalignments caused by mechanical stresses and temperature fluctuations throughout a night of observing. While active optics generally corrects for quasi-static errors in the optical system itself, adaptive optics corrects dynamic errors introduced by the atmosphere or other random media using a closed-loop real-time system. Generally, adaptive optics systems perform at much higher frequencies than active optics systems. Adaptive optics is not only used when propagating light through the atmosphere, but it is used to correct for distortions created when propagating light through any turbulent medium.



## 2.1 Adaptive Optics System Components

Adaptive optics systems consist of three key components: a device to measure the incoming wavefront, a wavefront correcting element, and a control computer to interface the wavefront measurements and needed corrections. A typical adaptive optics schematic can be seen in figure 2.1. A portion of the incoming aberrated wavefront is directed to the wavefront sensor where the wavefront errors are measured. Once the wavefront errors are known the control computer drives the correction device (i.e. the deformable mirror) to correct for the aberrations of the incoming wavefront. These components will be further discussed in chapter 3 or for further details refer to one of the available textbooks<sup>2,3,4,5,6</sup> These components must work together at a correction frequency greater than the frequency at which the turbulence changes the wavefront based on the application. In astronomical applications the Greenwood frequency<sup>7,8,9</sup> measures the temporal rate at which the atmosphere turbulence changes and is in the range of tens to hundreds of hertz. As a general rule of thumb for light propagating through the atmosphere, the closed-loop system bandwidth should be ten times the Greenwood frequency ranging from hundreds to thousands of hertz.<sup>10</sup> In other applications, such as vision science, the needed system bandwidth is much less.

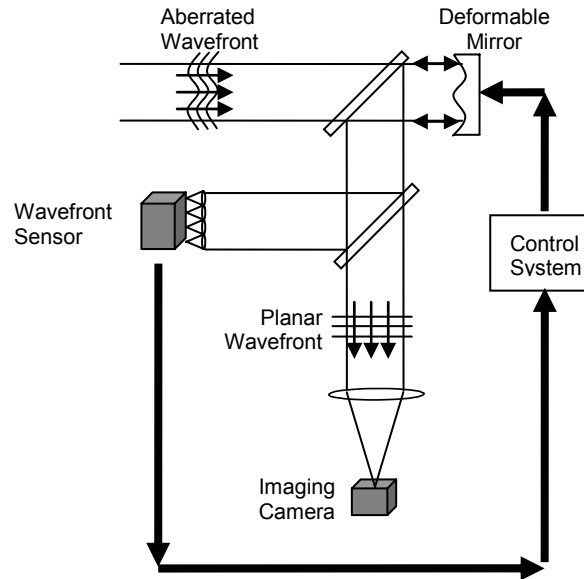


FIGURE 2.1: Adaptive Optics System

### 2.3 Brief History of Adaptive Optics

The real-time closed-loop adaptive optics system known today was first introduced by Babcock<sup>11</sup> in 1953. Babcock used a rotating knife edge at the focus to measure the deviation rays across the wavefront. An Eidophor, consisting of a mirror covered with a thin oil layer with electric charge deposited on the surface to electrostatically deviate the oil surface, was used as the wavefront correcting device. Two limitations mentioned by Babcock, that still plague adaptive optics systems today, are the small angular field of compensation and the need for a control star of a large enough magnitude.

Though initially proposed in 1953, adaptive optics systems did not produce experimental results until the 1970s. Some of the first systems used Coherent Optical Adaptive Techniques (COAT) to maximize the outgoing laser energy on a target in real-time. By measuring the glint of the target the COAT systems primarily used a

multidither<sup>12,13,14</sup> or phase conjugation<sup>15</sup> algorithm to maximize the intensity of the target glint. Systems were being developed not only to maximize laser beam energy but to also improve the resolution when imaging through the atmosphere. The real-time atmospheric compensation (RTAC) system by Hardy *et. al.* at Itek was first developed in 1973 and produced initial experimental results in 1977<sup>16</sup>. Another image compensation adaptive optics system was image sharpening described by Muller and Buffington<sup>17</sup> in 1974. First observatory results of image correction with the image-sharpening telescope were reported by Buffington *et. al.*<sup>18</sup> in 1977.

During the 1980s several adaptive optics image and laser compensation systems were being developed and tested<sup>19</sup>. In 1982 the Compensated Imaging System was installed on the AMOS telescope in Maui, Hawaii. This system was the first image compensation system using adaptive optics to be implemented on a telescope. This adaptive optics system consisted of a shearing interferometer as the wavefront sensor and a monolithic piezoelectric mirror for wavefront correction<sup>19</sup>. Due to the continuing problem of too few photons available from natural stars to overcome wavefront sensor noise, investigations of using synthetic beacons began.

In 1991 the Department of Defense declassified information on laser guide star systems and experiments that began in the mid 1980s.<sup>20,21</sup> This led to an explosion of adaptive optics related research focusing more on the applications and implementations of adaptive optics systems and less of the development of individual adaptive optics components. To this day, an increasing number of applications for adaptive optics are being discovered and implemented. To see the progression of adaptive optics refer to one of the many adaptive optics review papers.<sup>19,22,23,24,25,26,27,28</sup>

## 2.4 Applications

Adaptive optics was first proposed<sup>11</sup> for astronomical imaging through the turbulent atmosphere. During its developmental stage adaptive optics was used for two primary applications: imaging and laser beam propagation through atmospheric turbulence. Defense applications such as satellite imaging, maximizing laser beam power density and laser communications were and continue to be a driving force behind adaptive optics development. When propagating high power laser beams through the atmosphere the goal is to maximize the beam intensity by correcting for effects such as scintillation, thermal blooming, and beam wander.<sup>29</sup> In free-space laser communication, adaptive optics corrects the distortions that stretch pulses, distort pulse shape, and corrupt the modulation. Low order adaptive optics compensation have been applied<sup>30,31</sup> and have shown significant improvement by reducing the bit-error rate.<sup>32</sup> Astronomical seeing is perhaps the most well known application of adaptive optics as it has played a large role in improving the spatial resolution of ground-based telescopes.

Over the last fifteen years adaptive optics has appeared in applications where light is no longer propagated through the turbulent atmosphere but through other random media such as eye fluid and biological samples. Use of adaptive optics in vision science began in 1994 when Liang *et. al.*<sup>33</sup> used the Shack-Hartmann wavefront sensor to measure the aberrations of the eye. This led to the imaging of the retina through the eye fluid using a closed-loop adaptive optics system.<sup>34,35</sup> The ability to measure the aberrations of the eye and to image the retina have many implementations in the field of vision science such as custom eye correction devices and imaging of intraretinal layers. Adaptive optics aids laser eye surgery procedures through laser beam shaping and

measuring aberrations of the eye before and after surgery. High-resolution *in vivo* retinal imaging provides earlier detection and improved diagnosis of retinal diseases. Adaptive optics is also being used in current ophthalmic imaging devices such as the scanning laser ophthalmoscope<sup>36</sup> (SLO) and optical coherence tomography<sup>37</sup> (OCT) to improve the lateral and axial resolutions<sup>38</sup> of both devices. Further details on principles of adaptive optics in vision science can found in the available textbook.<sup>39</sup>

Adaptive optics is also being applied to the field of microscopy.<sup>40</sup> The nature and origin of aberrations in microscopy differ from telescope aberrations requiring a different approach to adaptive optics especially in wavefront sensing. Aberrations in microscopy are created both by the optical system and the specimen. Use of a high numerical aperture objective lens to focus laser pulses into the specimen and the index mismatch of the specimen, immersion fluid, and cover slip introduce spherical aberration. Scanning of the specimen also introduces off-axis aberrations. These static off-axis aberrations have been corrected with a deformable mirror and a genetic algorithm<sup>41</sup> so that for every position of the scanning objective there is an optimal correction shape to put on the deformable mirror. Dynamic specimen-induced aberration corrections with a closed-loop real-time adaptive optics system have been implemented in two-photon,<sup>42,43,44,45</sup> confocal,<sup>46,47</sup> and optical<sup>48</sup> microscopy. Because it is difficult to directly measure the wavefront at the focus of a high numerical aperture objective, indirect wavefront sensing methods are often used. Indirect wavefront sensing methods used in microscopy are modal wavefront sensing,<sup>49,50</sup> genetic algorithm,<sup>41,43</sup> hill-climbing algorithm,<sup>44</sup> and coherence-gated wavefront sensing.<sup>51,45</sup>

Other fields including 3D optical memory devices,<sup>52,53</sup> optical tweezers,<sup>54,55</sup> and coupling light into optical fibers<sup>56</sup> are using adaptive optics systems to correct for aberrations caused by focusing light deep into optical data storage media or refractive index mismatch in microscopy.

## CHAPTER 3: ADAPTIVE OPTICS PRINCIPLES

### 3.1 Aberration Representation with Zernike Polynomials

Aberrations can be represented with Zernike polynomials. Zernike created an orthogonal set of polynomials defined on a unit circle<sup>57</sup> so that, unlike with the power series, the phase can be represented by a unique set of coefficients. The even and odd Zernike polynomials in polar coordinates on a unit circle are defined as:

$$Z_n^m(\rho, \theta) = R_n^m(\rho) \cos(m\theta) \quad (3.1)$$

$$Z_n^{-m}(\rho, \theta) = R_n^m(\rho) \sin(m\theta) \quad (3.2)$$

where radial order  $n$  and azimuthal order  $m$  are nonnegative integers such that  $n \geq m$ .

The  $R_n^m$  term is the radial polynomial defined as

$$R_n^m(\rho) = \sum_{s=0}^{\frac{n-m}{2}} (-1)^s \frac{(n-s)!}{s! \left(\frac{n+m}{2} - s\right)! \left(\frac{n-m}{2} - s\right)!} \rho^{n-2s}. \quad (3.3)$$

Any wavefront phase can be represented as a summation of the present Zernike polynomials with their corresponding strengths. The first 21 Zernike polynomials with their corresponding aberration names are shown in table 3.1. Rigorous aberration theory can be found in Born and Wolf<sup>58</sup>.

Mode	n – radial order	m – azimuthal order	$Z_n^m$	Polynomial	Aberration
0	0	0	$Z_0^0$	1	Piston
1	1	1	$Z_1^1$	$\rho \cos \theta$	Tip
2	1	1	$Z_1^{-1}$	$\rho \sin \theta$	Tilt
3	2	0	$Z_2^0$	$2\rho^2 - 1$	Defocus
4	2	2	$Z_2^{-2}$	$\rho^2 \sin 2\theta$	Astigmatism (45°)
5	2	2	$Z_2^2$	$\rho^2 \cos 2\theta$	Astigmatism (0° and 90°)
6	3	1	$Z_3^{-1}$	$(3\rho^3 - 2\rho) \sin \theta$	Coma
7	3	1	$Z_3^1$	$(3\rho^3 - 2\rho) \cos \theta$	Coma
8	3	3	$Z_3^{-3}$	$\rho^3 \sin 3\theta$	Trefoil
9	3	3	$Z_3^3$	$\rho^3 \cos 3\theta$	Trefoil
10	4	4	$Z_4^{-4}$	$\rho^4 \sin 4\theta$	Spherical aberration
11	4	4	$Z_4^4$	$\rho^4 \cos 4\theta$	Spherical aberration
12	4	2	$Z_4^2$	$(4\rho^4 - 3\rho^2) \sin 2\theta$	
13	4	2	$Z_4^{-2}$	$(4\rho^4 - 3\rho^2) \cos 2\theta$	
14	4	0	$Z_4^0$	$6\rho^4 - 6\rho^2 + 1$	
15	5	1	$Z_5^{-1}$	$(10\rho^5 - 12\rho^3 + 3\rho) \sin \theta$	
16	5	1	$Z_5^1$	$(10\rho^5 - 12\rho^3 + 3\rho) \cos \theta$	
17	5	3	$Z_5^{-3}$	$(5\rho^5 - 4\rho^3) \sin 3\theta$	
18	5	3	$Z_5^3$	$(5\rho^5 - 4\rho^3) \cos 3\theta$	
19	5	5	$Z_5^{-5}$	$\rho^5 \sin 5\theta$	
20	5	5	$Z_5^5$	$\rho^5 \cos 5\theta$	

TABLE 3.1: Zernike Polynomials

### 3.2 Wavefront Sensors

One key component of an adaptive optics system is the wavefront sensor.<sup>59</sup> As its name suggests, the wavefront sensor measures the shape of the incoming wavefront to determine what wavefront errors are present. Wavefront sensing methods can be divided into one of two categories, direct (pupil-plane) and indirect (image-plane) wavefront



sensing. Direct wavefront sensors, such as the Shack-Hartmann sensor, curvature sensor<sup>60</sup>, or pyramid sensor<sup>61</sup>, directly measure the localized slope and curvature of the incoming wavefront across the exit pupil. From these measurements the control computer reconstructs the wavefront and forms the conjugate shape on the deformable mirror. Indirect wavefront sensors, such as phase diversity<sup>62</sup> and image sharpening<sup>17</sup>, do not calculate the wavefront directly. Instead measurements are taken from the image plane that are related the wavefront error and the deformable mirror alters the wavefront phase until the error is reduced. Whether the wavefront is measured directly or indirectly, the wavefront sensor provides information about the corrections needed and when correction is complete.

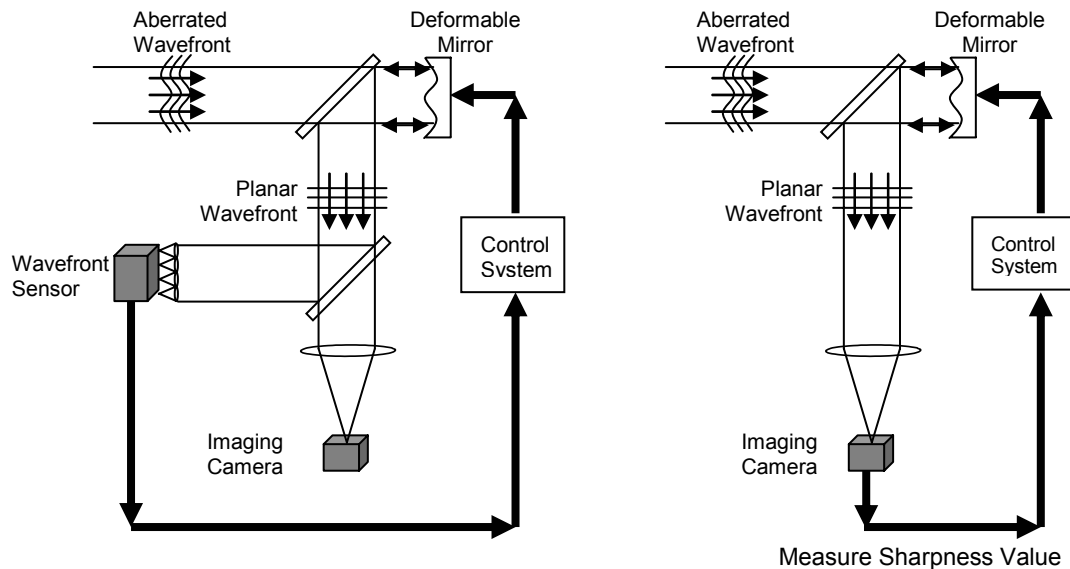


FIGURE 3.1: Adaptive Optics System with Direct and Indirect Wavefront Sensing.  
 a) Direct wavefront sensing with a Shack Hartmann  
 b) Indirect wavefront sensing with image sharpening

### 3.3 Wavefront Correction

The first wavefront correction device introduced by Babcock<sup>11</sup> was an Eidophor. This device consisted of a mirror covered with a thin oil layer on which a rastered electric charge was deposited allowing electrostatic charges to distort the oil film. Over the years a variety of wavefront correcting devices have been developed. Today in adaptive optics, the most common correction devices used are deformable mirrors and liquid-crystal spatial light modulators.<sup>63,64</sup>

Deformable mirrors are the most widely used correction devices. Two main advantages of membrane mirrors are their reflective nature, and thus little light loss, and their achromatic nature, as opposed to liquid-crystal spatial light modulators. There are several types of deformable mirrors including segmented, membrane, bimorph, and micro-electromechanical (MEM) mirrors. The focus of this section will be membrane deformable mirrors since they were used in this project.

Membrane deformable mirrors were first introduced in the late 1970's<sup>65,66</sup>. The first micromachined electrostatic, actuated membrane mirror was fabricated in the early 1990's by NASA's Jet Propulsion Laboratory<sup>67</sup>. A membrane deformable mirror consists of a thin (.5-1  $\mu\text{m}$  thick), silicon nitride micro-machined membrane with an aluminum reflective coating suspended over a hexagonal array of high-voltage electrodes. When voltage is applied to the electrodes they act as actuators as the electrostatic forces deflect the thin membrane. The membrane can only be pulled toward the electrodes so an initial bias voltage is applied to the actuators allowing the membrane to deform in both directions, toward and away from the electrodes. This bias voltage introduces defocus that must be compensated for additional optics. Unlike the bimorph mirror, this type of

mirror exhibits no hysteresis. The mean deflection of the membrane<sup>68,69</sup> follows Poisson's equation

$$\Delta U(x, y) = \nabla^2 U(x, y) = \frac{\partial^2 U(x, y)}{\partial x^2} + \frac{\partial^2 U(x, y)}{\partial y^2} = -P(x, y)/T \quad (3.4)$$

where U is the deflection, P is the load or pressure, and T is the tension. For electrostatic actuation the load is

$$P(x, y) = \frac{\epsilon_0 (V(x, y))^2}{d(x, y, P)^2} \quad (3.5)$$

where  $\epsilon_0$  is the dielectric constant of air, V is the electric potential distribution across the electrodes, and d is the distance between the membrane and the electrodes. As can be seen the mean deflection of the membrane is proportional to the applied voltage squared.

### 3.4 Measurement of Optical Quality and Image Evaluation

According to the Rayleigh limit no more than one-quarter wavelength of optical path difference (OPD) across the wavefront with respect to a reference sphere is acceptable<sup>70</sup>. Peak-to-valley (P-V) measures the maximum departure from a reference sphere. Root-mean-square (RMS) squares the OPD measurements across the aperture and takes the square root of the average of these squares about the mean. P-V works best for smooth wavefronts, while RMS is a better measurement when the wavefront is irregular. The Strehl ratio is the ratio of the intensity at the center of the Airy disk between that of an aberrated wavefront and that of a perfect wavefront. If the wavefront error variance is known the Strehl ratio is approximately,

$$S \cong \exp\left[-\left(\frac{2\pi}{\lambda}\right)^2 (\Delta\phi)^2\right] \cong \exp\left[-(2\pi\omega)^2\right] \quad (3.6)$$

where  $(\Delta\phi)^2$  is the wavefront error variance in units of optical path difference and  $\omega$  is the RMS OPD in waves. This calculation of Strehl ratio is convenient when aberrations are represented by wavefront or phase error variance. The wavefront error variance in units of radians squared is,

$$\sigma^2 = \left(\frac{2\pi}{\lambda}\right)^2 (\Delta\phi)^2. \quad (3.7)$$

An optical system is deemed acceptable if the Rayleigh limit is met such that P-V is less than one-quarter wave, RMS OPD is less than one-fourteenth to one-twentieth of a wave, or a Strehl ratio greater than 80 percent for spherical aberration. For other primary aberrations a quarter-wave does not necessarily produce a Strehl ratio of 0.80<sup>71</sup>.

## CHAPTER 4: IMAGE SHARPENING

### 4.1 Introduction

Image sharpening was first introduced by Muller and Buffington<sup>17</sup> as a technique for atmospheric correction of telescope images. With image sharpening, as seen in figure 4.1, a single sharpness value is measured from image plane information based on the sharpness metric, or sharpness definition. Once the sharpness value is measured a correction device such as a deformable mirror alters the incoming wavefront until the sharpness is maximized. This closed-loop system corrects the image in real-time as the wavefront changes. The key to image sharpening is choosing a sharpness metric that reaches a maximum sharpness value when no wavefront error is present and is sensitive to the introduction of aberrations. Several sharpness metrics have been successfully developed and implemented as will be discussed in this chapter.

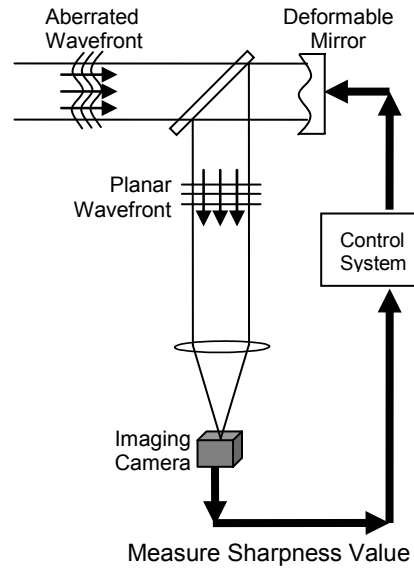


FIGURE 4.1: Image Sharpening Adaptive Optics System

## 4.2 History of Image Sharpening

Muller and Buffington presented several image plane sharpness metrics listed in table 4.1. Several metrics were tested with computer simulations of a simple closed-loop feedback adaptive optics system with corrective elements to maximize the sharpness. These simulations used the Fresnel-Kirchhoff equation to calculate the image irradiance for monochromatic light. Most of the metrics tested showed dramatic improvement in image quality after one or two iteration cycles. Proofs that the sharpness function reaches a maximum for the restored image were presented for metrics  $S_i$ ,  $S_{iii}$ ,  $S_{iv}$ ,  $S_v$ , and  $S_{viii}$ . These proofs evaluated the image irradiance using the Fresnel-Kirchhoff integral for monochromatic light over the surface of the telescope objective. Additional proofs of  $S_i$  and  $S_{iv}$  are presented by Hamaker *et al.*<sup>72</sup> using Fourier optics.

Definition	Computer Simulation	Comments
$S_i = \iint I^2(x, y) dx dy$	Satisfactory	Proved
$S_{ii} = I(x_o, y_o)$	Satisfactory	Satisfactory only for bright objects
$S_{iii} = \iint I(x, y) M(x, y) dx dy$	Satisfactory for M=round hole I=single or multiple stars	Proved if M represents the undistorted image
$S_{iv} = \iint \left  \frac{\partial^{l+m} I(x, y)}{\partial x^l \partial y^m} \right ^2 dx dy$	Untried	Proved
$S_v = \iint I^n(x, y) dx dy$ $n \geq 2$	Satisfactory for n=2,3,4	Proved only for unresolved star
$S_{vi} = -\iint I(x, y) r^2 dx dy$ $r^2 = x^2 + y^2$	Poor	Moment of inertia function. Proved
$S_{vii} = -\iint I(x, y) \ln(I(x, y)) dx dy$	Satisfactory	Minimizes entropy of the image
$S_{viii} = -\iint  I - I_o ^2 dx dy$	Untried	Defect function. Proved

TABLE 4.1: Image Sharpness Metric Definitions and Performances

Image sharpening was first implemented on a telescope by Buffington *et al.*<sup>18</sup> in 1977. A 30 x 5 cm aperture telescope was built with six movable mirrors as the correction device. Laser and white-light objects were imaged horizontally through 250 m of turbulent atmosphere. Sharpness metrics  $S_i$  and  $S_{iii}$  were used to obtain essentially diffraction-limited images as the computer simulations predicted. The mask used for metric  $S_{iii}$  was a slit with a width slightly less than the full-width half-maximum of the diffraction pattern at that location. This image-sharpening telescope was then installed at both the Leushner and Lick Observatory to obtain the first observatory results.<sup>18</sup> Image sharpening was successful in producing diffraction-limited images of a single star.

Image compensation has not only been performed by adaptive optics alone but also by post-detection image processing and a hybrid approach combining adaptive optics

with image post-processing. In the post-processing and hybrid approaches a large data set of short-exposure images are captured and processed to create a single image. Roggemann *et al.*<sup>73</sup> used image sharpness metrics listed in table 4.1 to select the best image frames to include in the post-processing. Using this method to select image frames resulted in greater signal-to-noise ratios (SNR) than processing the entire data set. A new

sharpness metric,  $S_{S1} = \int_0^{2\pi\rho_0} \int_0^{\rho_0} |I_F(\rho, \theta)|^2 d\rho d\theta$ , was presented where  $I_F$  is the Fourier

transform of the image intensity and  $\rho_0$  is the cutoff spatial frequency defined at

$\rho_0 = \frac{D}{\lambda f}$ . This metric ignores spatial frequencies above the cutoff frequency that are

caused by noise.

Vorontosov *et al.*<sup>74</sup> introduced a sharpness metric based on the Fourier spectrum of the image. After an image was formed with a coherent or incoherent optical system the image was sent to a spatial light modulator (SLM). The SLM is used with coherent illumination to optically generate the Fourier transform of the image. Image quality is characterized by a wide spatial spectrum and thus a small speckle size. The speckle field is produced by projecting the image spatial frequency spectral distribution onto a rotating frosted glass. The speckle field was measured by a photo-receiver where the photocurrent was related to the speckle size. Experimental results show improvement in imaging extended objects by minimizing the speckle size. This study was performed with particular interest in imaging extended objects for ground-to-ground and ground-to-air applications.

Image sharpening has been applied to coherent imaging with synthetic-aperture radar (SAR). Maximizing the sharpness using gradient search techniques has been used



to develop SAR autofocus algorithms<sup>75</sup>. Fienup and Miller<sup>76</sup> explored the use of sharpness metrics in SAR applications and found the best metric depends on the characteristics of the scene being imaged. When using the  $S_v$  power metric it was found that for scenes with bright and prominent points, large  $n$  powers worked better, where for scenes with dark regions and no prominent points, smaller  $n$  powers worked better. It was also found that the behavior of a sharpness metric depends on the second derivative of its point nonlinearity as a function of the image intensity.

#### 4.3 Advantages of Image Sharpening

Image sharpening is advantageous in fields where optical components need to be minimized for space and cost constraints since little to no additional wavefront sensing equipment is needed. Often the sharpness value is calculated from the image plane intensity that is captured with the imaging camera already present. Sensor speed is primarily dependant upon the control computer. Speed will continue to increase as faster computers are more readily available.

Another advantage is no point source is needed since this technique uses light from the object itself. Image sharpening works for extended objects as long as the object lies within the isoplanatic patch. Finally, the reconstruction stage of the wavefront, present with direct wavefront methods, is eliminated and thus reducing the computations necessary and increasing the speed.

## CHAPTER 5: THEORY

### 5.1 Introduction

Before discussing the necessary theory some basic definitions and theorems are presented. The Fourier transform of the function  $g(x,y)$  is defined as

$$G(f_x, f_y) = \mathcal{F}\{g(x,y)\} = \int \int_{-\infty}^{\infty} g(x,y) \exp[-i2\pi(f_x x + f_y y)] dx dy \quad (5.1)$$

and the inverse Fourier transform is

$$g(x,y) = \mathcal{F}^{-1}\{G(f_x, f_y)\} = \int \int_{-\infty}^{\infty} G(f_x, f_y) \exp[i2\pi(f_x x + f_y y)] df_x df_y . \quad (5.2)$$

The convolution between two functions,  $f(x)$  and  $h(x)$ , can be found by

$$f(x) * h(x) = g(X) = \int_{-\infty}^{\infty} f(x) h(X - x) dx . \quad (5.3)$$

The autocorrelation of a function is defined to be

$$f(x) \diamond f(x) = f(x) * f^*(-x) = \int_{-\infty}^{\infty} f(x) f^*(x - X) dx . \quad (5.4)$$

For the shift theorem, if  $G(f_x, f_y) = \mathcal{F}\{g(x,y)\}$ , then

$$\mathcal{F}\{g(x-a, y-b)\} = G(f_x, f_y) \exp[-i2\pi(f_x a + f_y b)] \quad (5.5)$$

where a translation in the space domain introduces a phase shift in the spatial frequency domain. In the same sense a phase shift in the space domain introduces a translation in the spatial frequency domain.

Parseval's theorem states if  $G(f_x, f_y) = \mathcal{F}\{g(x, y)\}$ , then

$$\int \int_{-\infty}^{\infty} |g(x, y)|^2 dx dy = \int \int_{-\infty}^{\infty} |G(f_x, f_y)|^2 df_x df_y . \quad (5.6)$$

The convolution theorem is if  $G(f_x, f_y) = \mathcal{F}\{g(x, y)\}$  and  $H(f_x, f_y) = \mathcal{F}\{h(x, y)\}$ , then

$$\mathcal{F}\{g(x, y) * h(x, y)\} = \mathcal{F}\left\{ \int \int_{-\infty}^{\infty} g(x, y) h(X - x, Y - y) dx dy \right\} = G(f_x, f_y) H(f_x, f_y). \quad (5.7)$$

Finally the autocorrelation theorem states if  $G(f_x, f_y) = \mathcal{F}\{g(x, y)\}$ , then

$$\mathcal{F}\left\{ \int \int_{-\infty}^{\infty} g(x, y) g^*(x - X, y - Y) dx dy \right\} = |G(f_x, f_y)|^2. \quad (5.8)$$

## 5.2 Scalar Diffraction Theory

Scalar diffraction theory<sup>58,77</sup> considers the scalar amplitude of either the electric or magnetic field transverse component neglecting the coupled nature of electric and magnetic field vectors. As long as the wavelength is much smaller than the diffracting aperture and diffracted fields are not observed too close to the aperture then the scalar theory produces accurate results. The Huygens-Fresnel principle states the optical field amplitude at any point beyond an obstruction is the superposition of all secondary spherical wavelets created by every unobstructed point on the wavefront. Kirchhoff later showed the Huygens-Fresnel principle is derivable from the scalar differential wave equation.

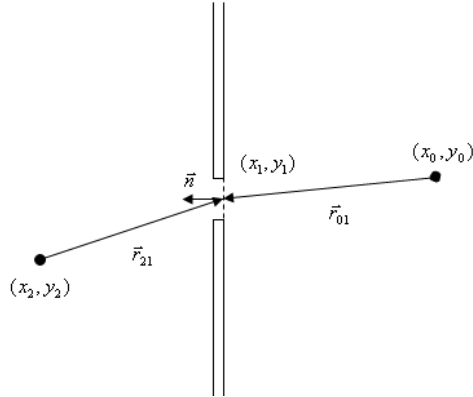


FIGURE 5.1: Point-source Illumination of a Plane Screen

Suppose a point-source is located at  $(x_2, y_2)$  in figure 5.1, illuminating the aperture,  $\Sigma$ , with a single spherical wave of amplitude  $A$ , then the field amplitude at the aperture is

$$U(x_1, y_1) = \frac{A \exp(ikr_{21})}{r_{21}}. \quad (5.9)$$

The field amplitude at the point of observation  $(x_0, y_0)$  can be found using the Fresnel-Kirchhoff diffraction equation:

$$U(x_0, y_0) = \frac{A}{2i\lambda} \iint_{\Sigma} \frac{\exp[ik(r_{21} + r_{01})]}{r_{21}r_{01}} [\cos(\vec{n}, \vec{r}_{01}) - \cos(\vec{n}, \vec{r}_{21})] ds. \quad (5.10)$$

Though the Kirchhoff theory experimentally has been found to yield accurate results there are inconsistencies for certain boundary conditions. These inconsistencies were removed by Sommerfeld producing the Rayleigh-Sommerfeld diffraction equation for point source illumination:

$$U(x_0, y_0) = \frac{A}{i\lambda} \iint_{\Sigma} \frac{\exp[ik(r_{21} + r_{01})]}{r_{21}r_{01}} \cos(\vec{n}, \vec{r}_{01}) ds. \quad (5.11)$$

The diffraction equation can be written more generally as

$$U(x_0, y_0) = \frac{1}{i\lambda} \iint_{\Sigma} U(x_1, y_1) \frac{\exp[ik(r_{01})]}{r_{01}} \cos(\vec{n}, \vec{r}_{01}) ds \quad (5.12)$$

where  $U(x_1, y_1)$  is the field amplitude at the aperture. Using linear systems theory later discussed in section 5.4 the diffraction equation can also be written as a superposition integral,

$$U(x_0, y_0) = \iint_{\Sigma} h(x_0, y_0; x_1, y_1) U(x_1, y_1) dx_1 dy_1 \quad (5.13)$$

where  $h$  is the weighting function defined as

$$h(x_0, y_0; x_1, y_1) = \frac{1}{i\lambda} \frac{\exp(ikr_{01})}{r_{01}} \cos(\vec{n}, \vec{r}_{01}). \quad (5.14)$$

### 5.2.1 Fresnel Diffraction

Using the linear systems representation of scalar diffraction in equations 5.13 and 5.14 some assumptions are made to derive Fresnel diffraction. Assume  $U(x_1, y_1)$  is zero outside the aperture, therefore the limits are infinite. Also assume the distance between the aperture and plane of observation is much larger than the size of the aperture. Therefore  $\cos(\vec{n}, \vec{r}_{01}) \cong 1$  and  $r_{01} \cong z$  in the denominator of equation 5.14. The superposition integral is as it was before,

$$U(x_0, y_0) = \int \int_{-\infty}^{\infty} h(x_0, y_0; x_1, y_1) U(x_1, y_1) dx_1 dy_1 \quad (5.15)$$

where the new weighting function with these assumptions is

$$h(x_0, y_0; x_1, y_1) = \frac{1}{i\lambda} \frac{\exp(ikr_{01})}{z}. \quad (5.16)$$

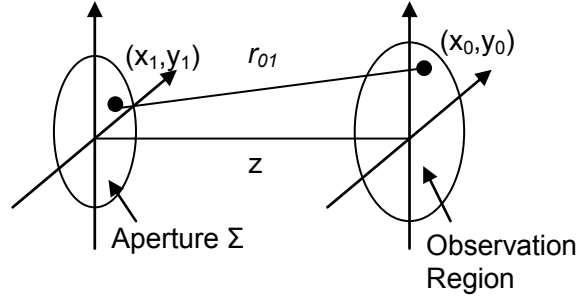


FIGURE 5.2: Diffraction Geometry for Fresnel Diffraction

From the diffraction geometry seen in figure 5.2, the distance  $r_{01}$  can be found exactly as

$$r_{01} = \sqrt{z^2 + (x_0 - x_1)^2 + (y_0 - y_1)^2} = z \sqrt{1 + \left(\frac{x_0 - x_1}{z}\right)^2 + \left(\frac{y_0 - y_1}{z}\right)^2}. \quad (5.17)$$

The binomial expansion of the square root is

$$\sqrt{1+a} = 1 + \frac{1}{2}a - \frac{1}{8}a^2 + \dots \quad |a| < 1. \quad (5.18)$$

Using the binomial expansion in the Fresnel region the distance  $r_{01}$  can be adequately approximated by using only the first two terms of the expansion resulting in

$$r_{01} \cong z \left[ 1 + \frac{1}{2} \left(\frac{x_0 - x_1}{z}\right)^2 + \frac{1}{2} \left(\frac{y_0 - y_1}{z}\right)^2 \right]. \quad (5.19)$$

From equation 5.16 the Fresnel diffraction weighting function can be written as

$$h(x_0, y_0; x_1, y_1) = \frac{\exp(ikz)}{i\lambda z} \exp\left\{ \frac{ik}{2z} [(x_0 - x_1)^2 + (y_0 - y_1)^2] \right\} \quad (5.20)$$

and the superposition integral and can be rewritten as

$$U(x_0, y_0) = \int \int_{-\infty}^{\infty} \frac{\exp(ikz)}{i\lambda z} \exp\left\{\frac{ik}{2z}[(x_0 - x_1)^2 + (y_0 - y_1)^2]\right\} U(x_1, y_1) dx_1 dy_1. \quad (5.21)$$

Expanding the quadratic term gives,

$$U(x_0, y_0) = \frac{\exp(ikz)}{i\lambda z} \exp\left[\frac{ik}{2z}(x_0^2 + y_0^2)\right] \int \int_{-\infty}^{\infty} U(x_1, y_1) \exp\left[\frac{ik}{2z}(x_1^2 + y_1^2)\right] \exp\left[-\frac{i2\pi}{\lambda z}(x_0 x_1 + y_0 y_1)\right] dx_1 dy_1 \quad (5.22)$$

This is the Fourier transform of  $U(x_1, y_1) \exp\left[\frac{ik}{2z}(x_1^2 + y_1^2)\right]$  such that  $f_x = \frac{x_0}{\lambda z}$

and  $f_y = \frac{y_0}{\lambda z}$ .

From the superposition integral, equation 5.21, it can be seen that the field amplitude  $U(x_0, y_0)$  is the convolution of  $U(x_1, y_1)$  with  $h(x_0, y_0; x_1, y_1)$ ,

$$U(x_0, y_0) = h(x_0, y_0; x_1, y_1) * U(x_1, y_1). \quad (5.23)$$

The Fresnel diffraction transfer function is the Fourier transform of the weighting function, equation 5.20, and is found to be

$$H(f_x, f_y) = \exp(ikz) \exp(-i\pi\lambda z(f_x^2 + f_y^2)). \quad (5.24)$$

Applying the convolution theorem gives

$$\mathcal{F}\{U(x_0, y_0)\} = H(f_x, f_y) \mathcal{F}\{U(x_1, y_1)\}. \quad (5.25)$$

## 5.2.2 Fraunhofer Diffraction

The Fraunhofer approximation is also referred to as the far-field approximation because not only do the Fresnel approximations still hold true, but there is the additional assumption that,

$$z \gg \frac{k(x_1^2 + y_1^2)_{\max}}{2}. \quad (5.26)$$

Using this approximation, the quadratic phase term in equation 5.22 goes to unity resulting in,

$$U(x_0, y_0) = \frac{\exp(ikz)}{i\lambda z} \exp\left[\frac{ik}{2z}(x_0^2 + y_0^2)\right] \int \int_{-\infty}^{\infty} U(x_l, y_l) \exp\left[-\frac{i2\pi}{\lambda z}(x_0 x_l + y_0 y_l)\right] dx_l dy_l \quad (5.27)$$

This is the Fourier transform of  $U(x_l, y_l)$ . Thus in the Fraunhofer diffraction region the field amplitude distribution is simply the Fourier transform of the aperture distribution.

### 5.3 Fourier Transforming Property of a Single Lens

As a wavefront passes through a lens the wavefront experiences a phase delay due to the thickness variation.

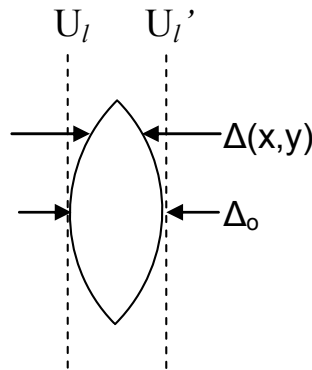


FIGURE 5.3: Thickness Function of a Lens



Looking at figure 5.3 the phase delay by the lens can be written as

$$\phi(x, y) = kn\Delta(x, y) + k[\Delta_o - \Delta(x, y)] \quad (5.28)$$

where  $\Delta_o$  is the maximum thickness,  $n$  is the index of refraction, and  $k$  is the wave number. The field just after the lens is found as

$$U_l'(x, y) = t_l(x, y) \cdot U_l(x, y) \quad (5.29)$$

where the transformation function of the lens is

$$t_l(x, y) = \exp[ik\Delta_o] \exp[ik(n-1)\Delta(x, y)]. \quad (5.30)$$

The thickness function of the lens is derived<sup>77</sup> to be

$$\Delta(x, y) = \Delta_o - \frac{x^2 + y^2}{2} \left( \frac{1}{R_1} - \frac{1}{R_2} \right) \quad (5.31)$$

where  $R$  is the radius of curvature for the front and back of the lens. Rewriting the transfer function gives

$$t_l(x, y) = \exp[ikn\Delta_o] \exp \left[ -ik(n-1) \left( \frac{x^2 + y^2}{2} \left( \frac{1}{R_1} - \frac{1}{R_2} \right) \right) \right]. \quad (5.32)$$

From geometric optics knowing

$$\frac{1}{f} = (n-1) \left( \frac{1}{R_1} - \frac{1}{R_2} \right) \quad (5.33)$$

and substituting into 5.31 gives

$$t_l(x, y) = \exp[ikn\Delta_o] \exp \left[ -\frac{ik}{2f} (x^2 + y^2) \right]. \quad (5.34)$$

Consider a coherent imaging system. A plane object with amplitude transmission  $t_o(x, y)$  is placed in the system at a distance  $s_o$  from the lens as seen in figure 5.4. Since

the lens is finite the aperture size can be accounted for with the pupil function  $P_l(x,y)$  where  $P_l(x,y) = 1$  inside the lens aperture and  $P_l(x,y) = 0$  otherwise.

The object is illuminated by a monochromatic plane wave of amplitude  $A$  such that the object field amplitude is

$$U_o(x,y) = A t_o(x,y). \quad (5.35)$$

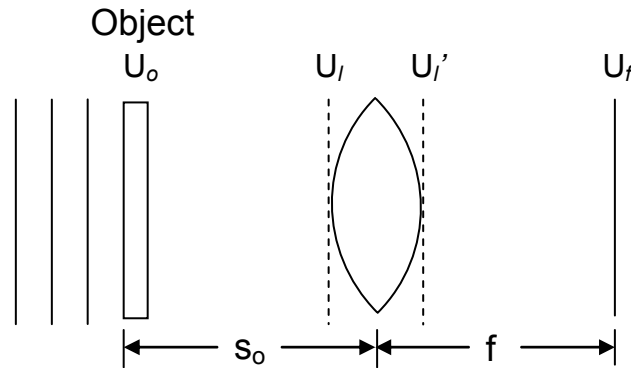


FIGURE 5.4: Configuration for the transforming property of a single lens.

Let  $F_o(f_x, f_y) = \mathcal{F}\{ U_o(x,y) \}$  and  $F_l(f_x, f_y) = \mathcal{F}\{ U_l(x,y) \}$ . Using the Fresnel transfer function, equation 5.25, propagation over distance  $s_o$  yields

$$F_l(f_x, f_y) = F_o(f_x, f_y) \exp(iks_o) \exp(-i\pi\lambda s_o(f_x^2 + f_y^2)). \quad (5.36)$$

Ignoring the constant phase factor  $\exp(iks_o)$ .

The field amplitude across the back focal plane,  $U_f$ , for an incoming field amplitude  $U_l$  is derived by Goodman<sup>77</sup> (page 85) to be

$$U_f(x_f, y_f) = \frac{1}{i\lambda f} \exp\left[\frac{ik}{2f}(x_f^2 + y_f^2)\right] \int_{-\infty}^{\infty} \int_{-\infty}^{\infty} U_l(x,y) \exp\left[-\frac{i2\pi}{\lambda f}(x_f x + y_f y)\right] dx dy. \quad (5.37)$$

Using the Fourier transform definition this can be rewritten as

$$U_f(x_f, y_f) = \frac{1}{i\lambda f} \exp\left[\frac{ik}{2f}(x_f^2 + y_f^2)\right] F_l\left(\frac{x_f}{\lambda f}, \frac{y_f}{\lambda f}\right). \quad (5.38)$$

Substituting in equation 5.36 yields

$$U_f(x_f, y_f) = \frac{1}{i\lambda f} \exp\left[\frac{ik}{2f}(x_f^2 + y_f^2)\right] F_o\left(\frac{x_f}{\lambda f}, \frac{y_f}{\lambda f}\right) \exp\left[-i\pi\lambda s_o\left(\frac{x_f^2}{\lambda^2 f^2} + \frac{y_f^2}{\lambda^2 f^2}\right)\right] \quad (5.39)$$

and can be rewritten as

$$U_f(x_f, y_f) = \frac{1}{i\lambda f} \exp\left[\frac{ik}{2f}(x_f^2 + y_f^2)\right] F_o\left(\frac{x_f}{\lambda f}, \frac{y_f}{\lambda f}\right) \exp\left[\frac{-iks_o}{2f^2}(x_f^2 + y_f^2)\right] \quad (5.40)$$

and rearranged to give

$$U_f(x_f, y_f) = \frac{1}{i\lambda f} \exp\left[\frac{ik}{2f}\left(1 - \frac{s_o}{f}\right)(x_f^2 + y_f^2)\right] F_o\left(\frac{x_f}{\lambda f}, \frac{y_f}{\lambda f}\right). \quad (5.41)$$

Replacing  $F_o$  and using equation 5.35 yields,

$$U_f(x_f, y_f) = \frac{A}{i\lambda f} \exp\left[\frac{ik}{2f}\left(1 - \frac{s_o}{f}\right)(x_f^2 + y_f^2)\right] \int_{-\infty}^{\infty} \int_{-\infty}^{\infty} t_o(x, y) \exp\left[-\frac{i2\pi}{\lambda f}(x_f x + y_f y)\right] dx dy. \quad (5.42)$$

If  $s_o = f$  then the phase curvature disappears and there is an exact Fourier relation of the object amplitude transmittance function. The intensity across the back focal plane,

$$I_f(x_f, y_f) = \frac{A^2}{\lambda^2 f^2} \left| \int_{-\infty}^{\infty} \int_{-\infty}^{\infty} t_o(x, y) \exp\left[-\frac{i2\pi}{\lambda f}(x_f x + y_f y)\right] dx dy \right|^2 \quad (5.43)$$

is the power spectrum of the object.

#### 5.4 Imaging using Linear Systems Theory

For any linear system the output is found to be the convolution of the input and the weighting, or impulse response, function  $h$ . This is known as the superposition integral.

$$g_2(x_2, y_2) = \int_{-\infty}^{\infty} \int_{-\infty}^{\infty} g_1(\xi, \eta) h(x_2 - \xi, y_2 - \eta) d\xi d\eta. \quad (5.44)$$

According to the convolution theorem if you take the Fourier transform of both sides the output spectra,  $G_2$  is found by

$$G_2(f_x, f_y) = H(f_x, f_y) G_1(f_x, f_y) \quad (5.45)$$

where  $H$ , known as the transfer function, is found by taking the Fourier transform of the impulse response function,

$$H(f_x, f_y) = \int_{-\infty}^{\infty} \int_{-\infty}^{\infty} h(x, y) \exp[-i2\pi(f_x x + f_y y)] dx dy. \quad (5.46)$$

An imaging system is a linear system and thus the definitions of linear systems can be applied to optics. The image field amplitude can be found by the superposition integral

$$U_i(x_i, y_i) = \int_{-\infty}^{\infty} \int_{-\infty}^{\infty} h(x_i, y_i; x_o, y_o) U_o(x_o, y_o) dx_o dy_o. \quad (5.47)$$

In optics the impulse response,  $h$ , is known as the point spread function where  $h$  is the image field amplitude in response to a point source object. The point spread function is also found to be the Fraunhofer diffraction pattern of a point source which is proportional to the Fourier transform of the exit pupil.

### 5.4.1 Coherent Imaging System

When the object is illuminated by a coherent source the impulse responses vary in unison and therefore there is a linear mapping of the complex field amplitudes from the object to the image. The point spread function is found to be the Fourier transform of the exit pupil.

$$h(x_i, y_i) = \int \int_{-\infty}^{\infty} P(\lambda dx, \lambda dy) \exp[-i2\pi(x_i x + y_i y)] dx dy \quad (5.48)$$

The superposition integral with complex field amplitudes is written as

$$U_i(x_i, y_i) = \int \int_{-\infty}^{\infty} h(x_i - x_o, y_i - y_o) U_o(x_o, y_o) dx_o dy_o \quad (5.49)$$

and the image intensity is written as.

$$I_i(x_i, y_i) = \left| \int \int_{-\infty}^{\infty} h(x_i - x_o, y_i - y_o) U_o(x_o, y_o) dx_o dy_o \right|^2 \quad (5.50)$$

Using the transfer function approach the coherent transfer function is

$$H(f_x, f_y) = \mathcal{F} \{ h(x_i, y_i) \} = \mathcal{F} \{ \mathcal{F} \{ P(\lambda dx, \lambda dy) \} \} = P(-\lambda dx, -\lambda dy). \quad (5.51)$$

Due to symmetry the coherent transfer function is equivalent to the exit pupil function.

Using the convolution theorem the image frequency spectra is

$$G_i(f_x, f_y) = H(f_x, f_y) G_o(f_x, f_y) \quad (5.52)$$

where the frequency spectra are found to be

$$G_i(f_x, f_y) = \int \int_{-\infty}^{\infty} U_i(x, y) \exp[-i2\pi(f_x x + f_y y)] dx dy \quad (5.53)$$

$$G_o(f_x, f_y) = \int \int_{-\infty}^{\infty} U_o(x, y) \exp[-i2\pi(f_x x + f_y y)] dx dy. \quad (5.54)$$

### 5.4.2 Incoherent Imaging System

When imaging with incoherent illumination the impulse responses vary independently and must be added, not by the complex amplitude, but by the intensity. Therefore, incoherent imaging systems are linear by intensity mapping so that the superposition integral is written as

$$I_i(x_i, y_i) = \kappa \int_{-\infty}^{\infty} \int_{-\infty}^{\infty} |h(x_i - x_o, y_i - y_o)|^2 I_o(x_o, y_o) dx_o dy_o \quad (5.55)$$

where  $\kappa$  is a real constant and the incoherent point spread function is the intensity of the coherent point spread function.

In incoherent imaging, the frequency spectra and transfer functions are normalized to the background dc component to better view the frequency contrast. The normalized frequency spectra are defined as

$$\mathcal{G}_i(f_x, f_y) = \frac{\int_{-\infty}^{\infty} \int_{-\infty}^{\infty} I_i(x, y) \exp[-i2\pi(f_x x + f_y y)] dx dy}{\int_{-\infty}^{\infty} \int_{-\infty}^{\infty} I_i(x, y) dx dy} \quad (5.56)$$

$$\mathcal{G}_o(f_x, f_y) = \frac{\int_{-\infty}^{\infty} \int_{-\infty}^{\infty} I_o(x, y) \exp[-i2\pi(f_x x + f_y y)] dx dy}{\int_{-\infty}^{\infty} \int_{-\infty}^{\infty} I_o(x, y) dx dy} \quad (5.57)$$

And the normalized transfer function, also known as the optical transfer function is

$$\mathcal{H}(f_x, f_y) = \frac{\int_{-\infty}^{\infty} \int_{-\infty}^{\infty} |h(x, y)|^2 \exp[-i2\pi(f_x x + f_y y)] dx dy}{\int_{-\infty}^{\infty} \int_{-\infty}^{\infty} |h(x, y)|^2 dx dy} \quad (5.58)$$

which can also be written as

$$\mathcal{H}(f_x, f_y) = \frac{\mathcal{F}\{|h(x, y)|^2\}}{\mathcal{F}\{|h(x, y)|^2\}_{f_x=0, f_y=0}} \quad (5.59)$$

Using the autocorrelation theorem, equation 5.8, and equation 5.48 the optical transfer function is found to be the autocorrelation of the exit pupil (area of overlap) divided by the total area

$$\mathcal{H}(f_x, f_y) = \frac{\int_{-\infty}^{\infty} \int_{-\infty}^{\infty} P\left(\xi + \frac{\lambda d_i f_x}{2}, \eta + \frac{\lambda d_i f_y}{2}\right) P\left(\xi - \frac{\lambda d_i f_x}{2}, \eta - \frac{\lambda d_i f_y}{2}\right) d\xi d\eta}{\int_{-\infty}^{\infty} \int_{-\infty}^{\infty} P(\xi, \eta) d\xi d\eta}. \quad (5.60)$$

According to the convolution theorem

$$\mathcal{G}_i(f_x, f_y) = \mathcal{H}(f_x, f_y) \mathcal{G}_o(f_x, f_y). \quad (5.61)$$

## 5.5 Spatial Filtering

The Fourier transforming property of a single convex lens is one of the most widely used since Abbe's microscopy application in the nineteenth century<sup>78</sup>. The ability to perform Fourier transforms simply with a single lens leads to the analysis of the frequency domain of an optical imaging system and how it relates to the image spatial domain. Abbe<sup>78</sup> and Porter<sup>79</sup> reported the first results showing how altering the frequency domain by placing filters in the Fourier plane affect the image spectrum and therefore the image itself. By filtering out spatial frequencies in the Fourier domain the frequency components of the object distribution are removed from the image plane. If a low-pass filter is placed in the Fourier plane the high frequencies, carrying the object detail and edges, are removed resulting in a smoother image of the object. If instead a high-pass filter were placed in the Fourier domain only the high frequencies would pass

enhancing the object edges and details in the image plane. A common way to perform spatial filtering is by the use of a 4-F system illustrated in figure 5.5. An object transparency or spatial light modulator is placed in the object plane and illuminated with a coherent monochromatic plane wave. The Fourier transform of the object is located at the back focal plane where the filter is placed to filter out the desired spatial frequencies and the resulting image is formed at the image plane.

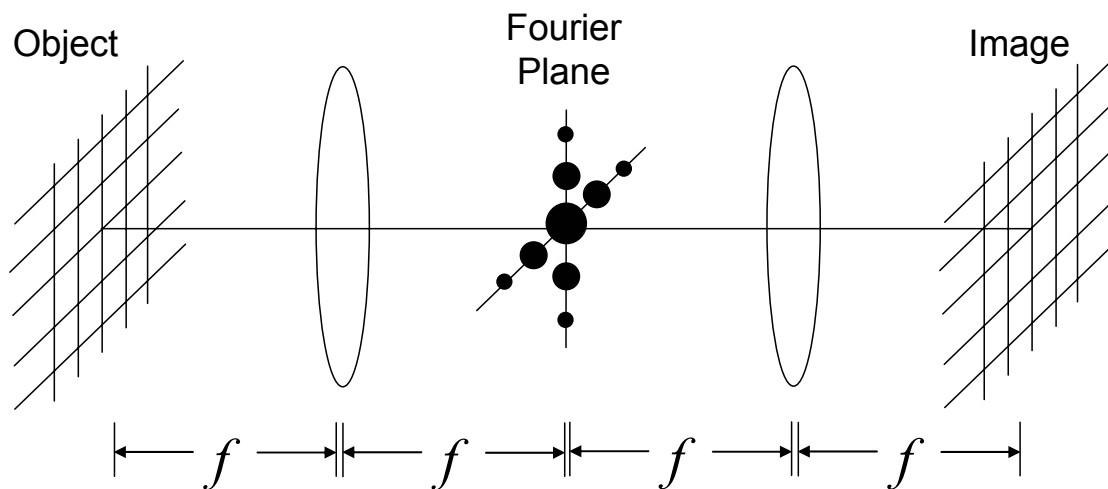


FIGURE 5.5: 4-F system; light incident on the object is a plane wave of coherent and monochromatic light

Figure 5.6 shows the results of spatial filtering with a 4-F system like that in figure 5.5 using two  $f = 150$  mm plano-convex lenses. The low-pass image, figure 5.6c, was obtained by placing an iris diaphragm in the Fourier plane allowing only the low spatial frequencies to pass to the image plane. It can be seen from the low-pass image that low frequencies contain information about the basic size and gross shape of the object. To obtain the high-pass image a small circular obstruction was centered in the



Fourier plane allowing the high spatial frequencies to pass resulting in figure 5.5d. High spatial frequencies carry information about the edges and fine detail of the object.

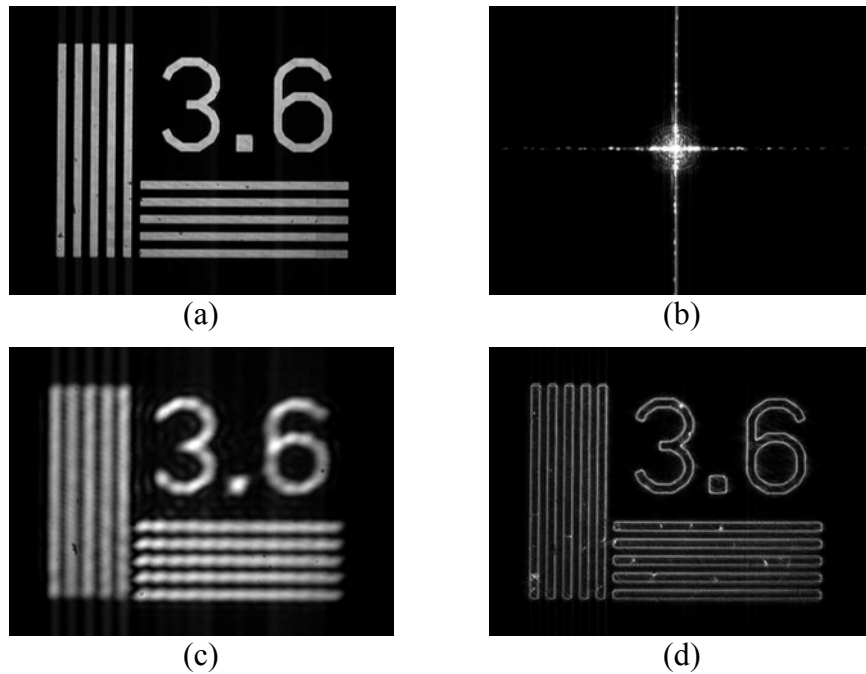


FIGURE 5.6: Spatial filtering using a 4-f system. (a) image plane, (b) Fourier plane, (c) image plane with a low-pass filter at the Fourier plane, and (d) image plane with a high-pass filter at the Fourier plane

## CHAPTER 6: FOURIER-BASED IMAGE SHARPNESS SENSOR

### 6.1 Introduction

Image sharpening is an indirect, image plane method for wavefront correction. The sharpness value is measured using the definition given by the sharpness metric. A Fourier-based image sharpness sensor uses a sharpness metric based on the Fourier transform of the image. In this chapter the components of such a sensor will be discussed, mainly the Fourier-based sharpness metric as it is the primary focus of this dissertation.

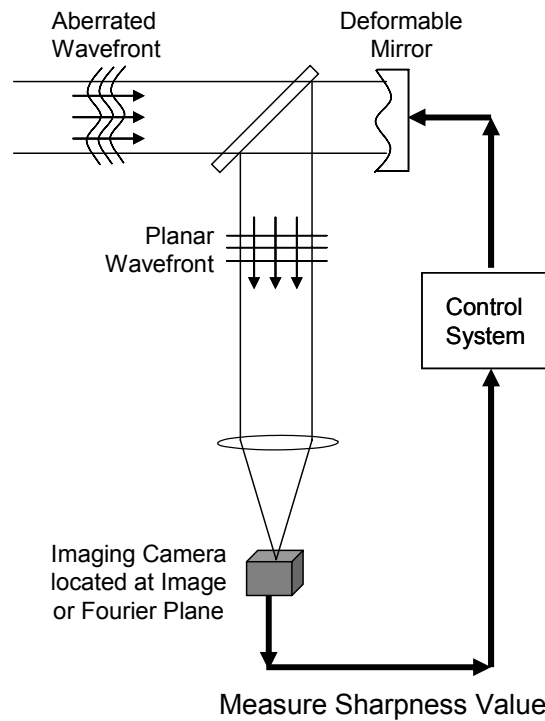


FIGURE 6.1: Image Sharpness Sensor Configuration.

## 6.2 Image Sharpness Sensor Configuration

The basic image sharpness sensor configuration is seen in figure 6.1. Location of the imaging camera is either at the image or Fourier plane depending on the sharpness metric used. After the image is captured the control system, consisting of the computer with calculating software and the hardware interfacing, calculates the sharpness value using a given sharpness metric. After the first sharpness calculation, the algorithm begins the process of maximizing the sharpness value by driving the deformable mirror (DM). One cycle consists of adjusting the DM actuator values, capturing a new image, and calculating the new sharpness value. If the sharpness value increases the mirror continues to move in that direction; if the sharpness value decreases the direction of motion for that DM actuator is reversed. This cycle continues until the sharpness value reaches a maximum. There are three main units of the image sharpness sensor: the sharpness metric, optical components (i.e. imaging camera and deformable mirror), and the search algorithm. Each of the units are discussed in the following sections.

## 6.3 Sharpness Metrics

The sharpness metric is the definition by which the sharpness values is calculated. Five sharpness metrics were used in this dissertation, four of which are new Fourier-based sharpness metrics. The five sharpness metrics are:

$$S_{i2} = \frac{\iint I_i^2(x, y) dx dy}{\left(\iint I_i(x, y) dx dy\right)^2} \quad (6.1)$$

$$S_1 = \frac{\iint |\mathcal{F}\{I_i(x, y)\}| df_x df_y}{\iint I_i(x, y) dx dy} \quad (6.2)$$

$$S_2 = \frac{\iint |\mathcal{F}\{I_i(x, y)\}_{masked}|^2 df_x df_y}{\iint |\mathcal{F}\{I_i(x, y)\}_{unmasked}|^2 df_x df_y} \quad (6.3)$$

$$S_3 = \frac{\iint |\mathcal{F}\{U_i(x, y)\}_{masked}|^2 df_x df_y}{\iint |\mathcal{F}\{U_i(x, y)\}_{unmasked}|^2 df_x df_y} \quad (6.4)$$

$$S_4 = \frac{\iint I(x, y)_{spatiallyfiltered} dx dy}{\iint I(x, y) dx dy} \quad (6.5)$$

This first metric,  $S_{i2}$ , is the intensity squared sharpness metric that is most common in image sharpening. This metric was first introduced and proved by Muller and Buffington and has been implemented in a closed-loop adaptive optics system.<sup>17,18,,80,81</sup> as discussed in chapter 4. By squaring the intensity at each pixel the difference in intensity values from pixel to pixel increases and thus the contrast is enhanced. When aberrations are added the image contrast decreases, and therefore so does the defined sharpness value. To account for overall changes in the image intensity, the metric is normalized by dividing by the square of the total intensity, or the total power squared. The units of this metric are  $1/m^2$ . Consider a point source object, increasing the aberrations causes the spatial spot size (measured in meters) to increase and the  $1/m^2$  to decrease and thus the sharpness value also decreases. In the similar sense, when imaging a bar chart test pattern, adding aberrations causes the distance between bars to increase which is an increase in spatial size (m) and a decrease in the spatial frequency (1/m).

Using Parseval's theorem

$$S_{i2} = \frac{\iint |I_i(x, y)|^2 dx dy}{\left(\iint I_i(x, y) dx dy\right)^2} = \frac{\iint |\mathcal{F}\{I_i(x, y)\}|^2 df_x df_y}{\left(\iint I_i(x, y) dx dy\right)^2} \quad (6.6)$$

where  $I_i$  is the image plane intensity, it can be seen that this metric can also be found from the Fourier domain. Though this is an interesting observation, the original sharpness metric is faster because often the image plane intensity is measured so there is no need to add extra calculations to find the Fourier transform. For the experiments in chapters 7 and 8 the  $S_{12}$  sharpness metric will be used for comparison.

As mentioned before when imaging a bar chart target, adding aberrations causes the spacing between bars to increase and the spatial frequency to decrease. For an incoherent imaging system the image spatial frequency spectra is found to be

$$\mathcal{G}_i(f_x, f_y) = \mathcal{H}(f_x, f_y) \mathcal{G}_o(f_x, f_y). \quad (6.7)$$

where  $\mathcal{H}(f_x, f_y)$  is the optical transfer function found to be the autocorrelation of the exit pupil, equation 5.60. The optical transfer function (OTF) shows how a system transfers the spatial frequencies of the object spectra to the image spectra. Aberrations of the system affect the OTF, not the object or image spectra. To see the affects of aberrations on different spatial frequencies, aberrations of various strengths and types were applied to the phase of the pupil function that was autocorrelated to find the OTF. Figure 6.2 shows the cross-sectional plots of the OTF modulus, the modulus transfer function (MTF), versus spatial frequency with zero spatial frequency in the center. Each subfigure contains plots of different aberration types with varying strengths. It can be seen for all aberration types, as the aberration strength increases the high spatial frequencies and the sum of all spatial frequencies decreases.

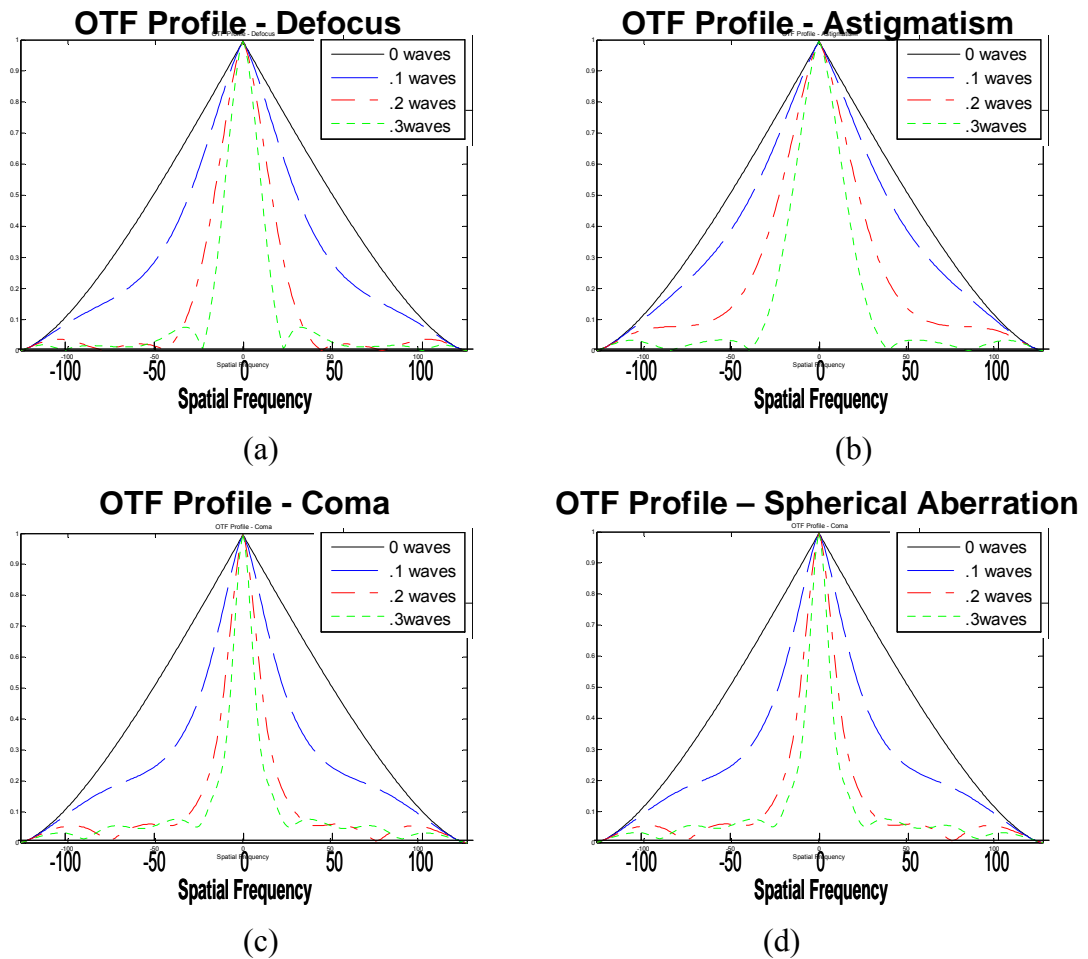


FIGURE 6.2: MTF cross-section plots with varying aberration strengths of (a) defocus, (b) astigmatism, (c) coma, and (d) spherical aberration.

From equation 6.6 it can be seen that squaring the magnitude of the spatial frequency at each pixel and taking the sum will produce a sharpness value that reaches a maximum when the wavefront error is zero. If the magnitudes of the spatial frequencies are summed without squaring each value then this is a new sharpness metric. For normalization, the sum is divided by the total power instead of power squared since there is no squaring in the numerator. This produces the sharpness metric  $S_1 =$

$$\frac{\iint |\mathcal{F}\{I_i(x, y)\}| df_x df_y}{\iint I_i(x, y) dx dy} \text{ with units of } 1/m^2. \text{ This metric can be used with an incoherent or}$$

coherent imaging system where the image intensity is captured with the image plane camera and the Fourier transform is found digitally.

From figure 6.2 it can be seen that as aberrations are added the higher spatial frequencies decrease. High spatial frequencies carry information about the edges and details of the image as seen in figure 5.6. Knowing this, if the low spatial frequencies are masked out and the remaining high spatial frequencies are summed and divided by the total unmasked spatial frequencies then this ratio is maximized when the wavefront error

is zero. This is represented as the sharpness metric  $S_2 = \frac{\iint |\mathcal{F}\{I_i(x, y)\}_{masked}| df_x df_y}{\iint |\mathcal{F}\{I_i(x, y)\}_{unmasked}| df_x df_y}$

where the Fourier transforming and masking are performed digitally on the image intensity captured with the image plane camera. This can be used in both incoherent and coherent imaging.

In a coherent imaging system a single lens produces the Fourier transform distribution of the object at the Fourier plane located before the image plane. If a camera is placed at the Fourier plane it captures  $|\mathcal{F}\{U_i(x, y)\}|^2$ . Again the sharpness value can be found by masking out the low spatial frequencies and dividing the sum of the remaining high spatial frequencies by the sum of the total unmasked spatial frequencies

to give the sharpness metric  $S_3 = \frac{\iint |\mathcal{F}\{U_i(x, y)\}_{masked}|^2 df_x df_y}{\iint |\mathcal{F}\{U_i(x, y)\}_{unmasked}|^2 df_x df_y}$ . The captured image of

the Fourier transform distribution is masked digitally and this works for coherent imaging only.

Finally the concept of spatially filtering discussed in section 5.5 can be applied to

create sharpness metric  $S_4 = \frac{\iint I(x, y)_{spatiallyfiltered} dx dy}{\iint I(x, y) dx dy}$ . This sharpness metric requires

that the optical path be divided into two paths with a camera at each image plane. In one path a physical, opaque, high-pass filter is placed at the Fourier plane and the camera is placed at the image plane. The spatially filtered image intensity will be greatest when aberrations are the smallest because there are more high spatial frequencies that pass by the mask. For normalization, the total power measured from the spatially filtered image plane camera is divided by the total power of the unfiltered image plane camera to give the sharpness value.

In this section, four novel Fourier-based sharpness metrics have been introduced. The performance of these metrics will be investigated in chapters 7 and 8 and compared to the  $S_{i2}$  metric.

#### 6.4 Optical Components

Two main optical components used in the Fourier-based image sharpness sensor, are the imaging camera and the deformable mirror. The imaging camera is a charged couple device (CCD) camera. Specifications of the CCD camera are listed in table 6.1.

Model	Pulnix TM-7CN
Imager/Pick-up Element	$\frac{1}{2}'' = 12.7 \text{ mm}$
No. of Pixels	768 x 494
Cell Size	$8.4 \mu\text{m} \times 9.8 \mu\text{m}$
Effective Area	$4.8 \text{ mm} \times 6.5 \text{ mm}$
TV Resolution	570 x 350

TABLE 6.1: CCD Camera Specifications



Two deformable mirrors were used and are referred to as the AgilOptics and the OKO deformable mirrors. Both deformable mirrors are micromachined membrane deformable mirrors with 37 electrostatic actuators. The profile of the AgilOptics deformable mirror is seen in figure 6.3 and the actuator array pattern of the AgilOptics mirror is seen in figure 6.4.

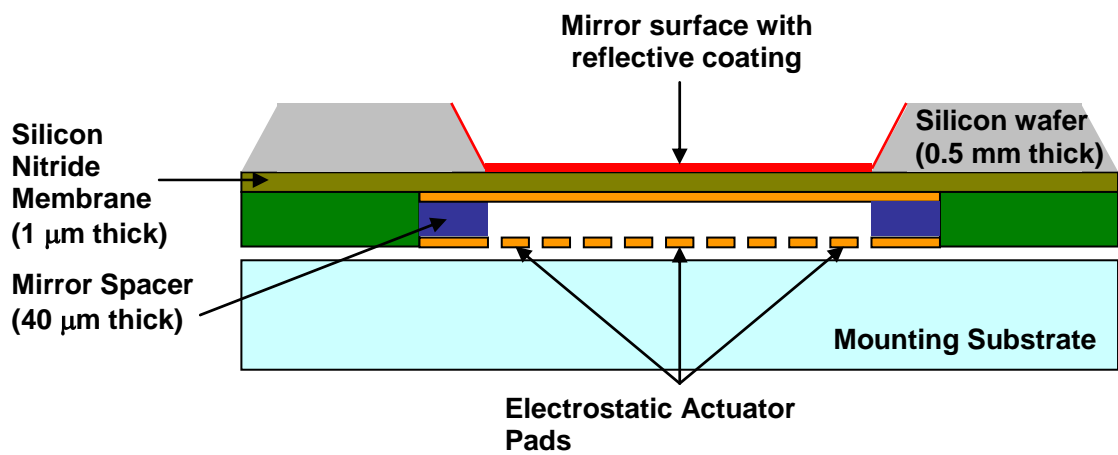


FIGURE 6.3: AgilOptics Deformable Mirror Profile

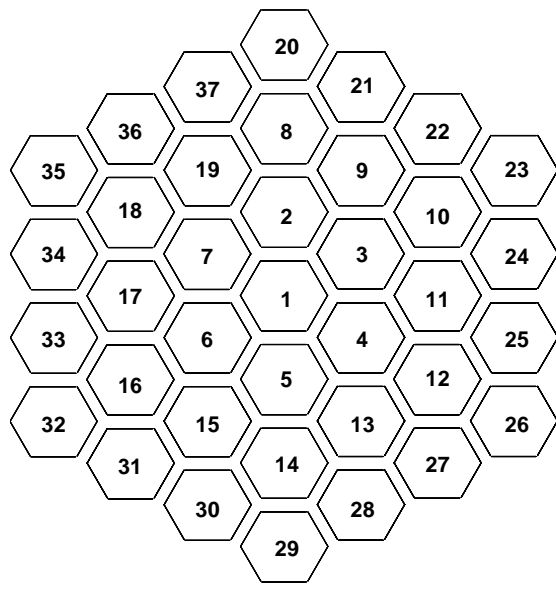


FIGURE 6.4: AgilOptics Actuator Array

Table 6.2 lists the specifications of the deformable mirrors. The active portion of each mirror is roughly 60% of the membrane diameter<sup>82</sup>.

Model	AgilOptics DM 16-37	OKO MMDM 15-37
Membrane Mirror Diameter	25 mm	15 mm
Useable Mirror Diameter	~15 mm	~9 mm
Number of Actuators	37	37
Maximum Drive Voltage	150 V	237 V
Maximum Deflection at Mirror Center	7 $\mu\text{m}$	9 $\mu\text{m}$

TABLE 6.2: Deformable Mirror Specifications

## 6.5 Search Algorithm

The accuracy and speed at which the maximum sharpness value is obtained depends highly on the search algorithm used. Due to the large number of degrees of freedom, a non-systematic algorithm is best to use. Unlike systematic algorithms that traverse the whole search space, a non-systematic algorithm creates a random guess and uses the information obtained to create the next guess and disregards the rest of the search space. Non-systematic search algorithms such as Simplex, simulated annealing, and stochastic gradient descent algorithms, have been studied in-depth in the dissertations of Doble<sup>80</sup> and Murray<sup>81</sup>. Further investigation of these search algorithms are not covered in this dissertation. Choice of the search algorithm depends on the application and must consider the factors of speed and how easily the algorithm finds an absolute maximum without stopping on a local maximum.

## CHAPTER 7: PERFORMANCE OF THE FOURIER-BASED IMAGE SHARPNESS SENSOR IN INCOHERENT IMAGING

### 7.1 Introduction

In this chapter the performance of the Fourier-based sharpness metrics used in an incoherent imaging system will be investigated. To investigate the capabilities of these sharpness metrics the sharpness values are calculated as aberrations are added. The sharpness metrics and system configurations for incoherent imaging will be discussed in sections 7.2 and 7.3. For simplicity defocus was the first aberration used to compare the three sharpness metrics. The sharpness versus defocus plots are present in section 7.4 to compare performance of the sharpness metrics for various objects. Higher order aberrations are later added in section 7.5 to see how the sharpness metric behaves as the aberration strength increases. Finally, in section 7.6 the sharpness metrics are implemented in a simple and manual closed-loop system.

### 7.2 Sharpness Metrics

Three sharpness metrics will be used throughout this chapter. The first is the intensity squared metric

$$S_{i2} = \frac{\iint I_i^2(x, y) dx dy}{\left(\iint I_i(x, y) dx dy\right)^2} = \frac{\sum I_i^2(x, y)}{\left(\sum I_i(x, y)\right)^2} \quad (7.1)$$

where the camera is located at the image plane to capture the image intensity. For  $S_{i2}$  each pixel value is squared and these squared values are summed up and divided by the

square of the summed pixel values.

The second sharpness metric is the first of the two Fourier-based metrics analyzed,

$$S_1 = \frac{\iint |\mathcal{F}\{I_i(x, y)\}| df_x df_y}{\iint I_i(x, y) dx dy} = \frac{\sum |\mathcal{F}\{I_i(x, y)\}|}{\sum I_i(x, y)}. \quad (7.2)$$

Again the camera is located at the image plane and the Fourier transform of the image intensity distribution is found digitally using the Fast Fourier Transform (FFT) algorithm. After the FFT has been performed, the  $S_1$  sharpness value is found to be the sum of the modulus of the Fourier transformed value at each pixel divided by the sum of the intensity pixel values.

The second Fourier-based sharpness metric is

$$S_2 = \frac{\iint |\mathcal{F}\{I_i(x, y)\}_{masked}| df_x df_y}{\iint |\mathcal{F}\{I_i(x, y)\}_{unmasked}| df_x df_y} = \frac{\sum |\mathcal{F}\{I_i(x, y)\}_{masked}|}{\sum |\mathcal{F}\{I_i(x, y)\}_{unmasked}|} \quad (7.3)$$

where the image intensity is captured by the image plane camera and the Fourier transform of the image intensity and the masking of the Fourier distribution are both found digitally. To calculate  $S_2$  the center pixels of the Fourier transform within a circle of a mask size radius are set to zero to mask out the low spatial frequencies. The absolute values of the remaining spatial frequency values are summed and divided by the sum of the absolute value of the original, unmasked, Fourier transform to give the  $S_2$  sharpness value.

### 7.3 System Configuration

For incoherent imaging information used for all sharpness value calculations is obtained from image plane camera. The Fourier transforming property of a single lens

can only be used with coherent light therefore for incoherent imaging the Fourier transform must be performed digitally. In the same sense any masking must be done digitally because there is no Fourier plane to physically mask.

Two incoherent imaging systems were used. First an imaging system was built on the optics table with the object illuminated by an incoherent Light Emitting Diode (LED) source. The second system was an 11 inch telescope with a camera mounted on it to capture several types of incoherent scenes of objects ranging in distance up to 5 km.

The optics table incoherent imaging system setup can be seen in figures 7.1 and 7.2. The object is illuminated by a StockerYale LED. Two deformable mirrors are placed in the system to both create and correct aberrations in the system. At the image plane a Pulnix CCD camera is placed to capture the image intensity distribution. Once the image is captured it is imported into MatLab and converted to a 640x640 array of intensity values for each pixel from which the sharpness value can be calculated using the metrics and methods described in section 7.2.

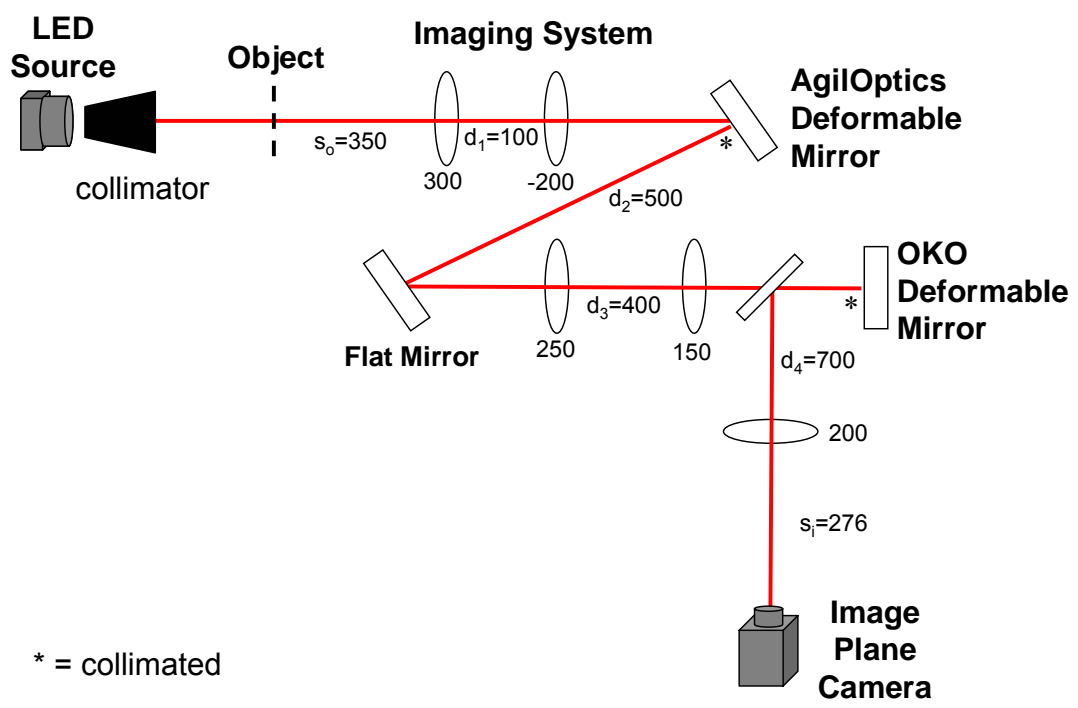


FIGURE 7.1: Experimental schematic with an incoherent source and the camera at the image plane. All numbers are in units of millimeters.

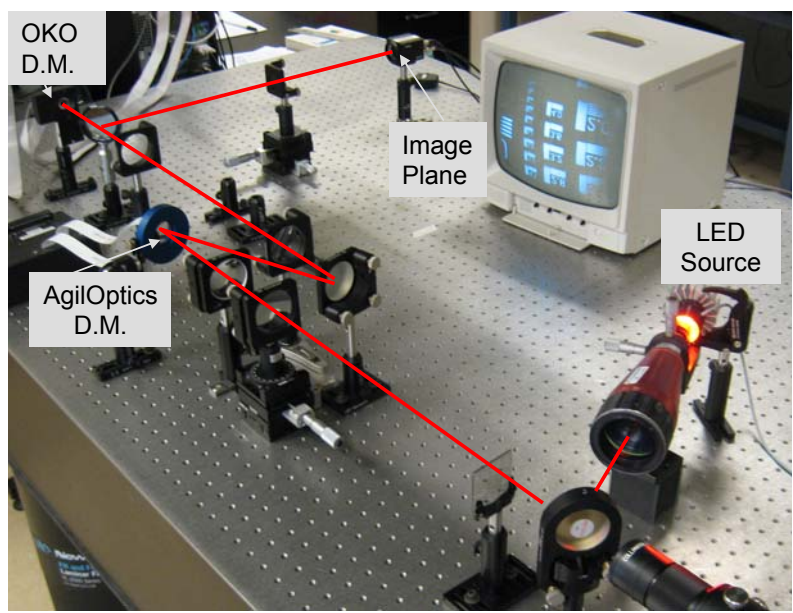


FIGURE 7.2: Optics table experimental setup. Incoherent LED source with the camera at the image plane.

The telescope system setup can be seen in figure 7.3. The telescope used was a Celestron NexStar telescope with an 11 inch aperture, a 70x magnification (with the standard 40mm eyepiece), and a resolution of 0.50 arc seconds based on the Rayleigh limit. Various daytime and nighttime objects were imaged by directing the telescope out of the laboratory window overlooking the UNC Charlotte campus as seen in figure 7.3. Defocus was added by turning to focus knob. The Pulnix CCD camera was mounted on the telescope at the image plane to capture the image intensity distribution. Again the captured image was imported into MatLab where sharpness values were calculated using the same methods as the optics table configuration.

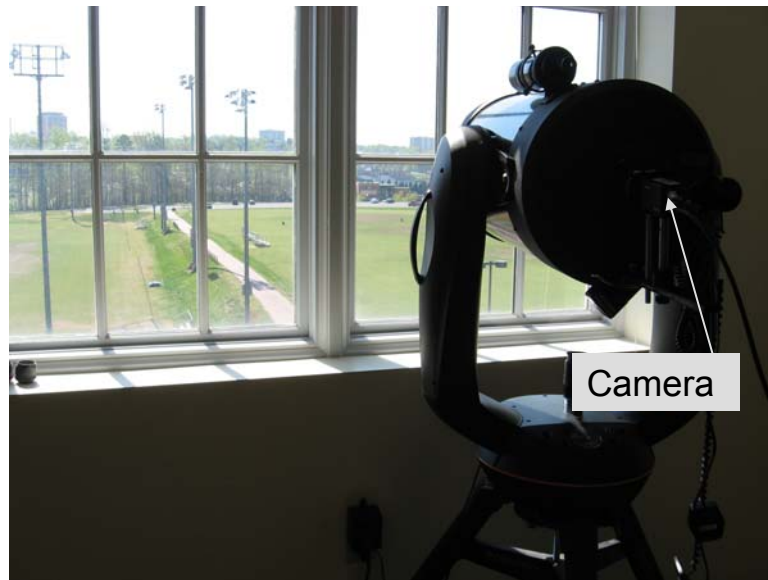


FIGURE 7.3: Telescope experimental setup with a Celestron NexStar 11 inch telescope and a CCD camera mounted at the image plane.

#### 7.4 Sharpness versus Defocus Experimental Results

In these experiments the sharpness value was measured using one of the three sharpness metrics and plotted versus aberration strength to see if the sharpness value does in fact reach a maximum when aberrations are reduced. For simplicity defocus was the first and only aberration implemented during the experiments in this section. Higher-order aberrations are applied and studied in section 7.5.

For a given object and object distance, the image plane camera was adjusted to display the image at focus. Initially all the actuators of the AgilOptics deformable mirror (DM) were set to a bias voltage of 50 V and all the OKO DM actuators values were set to zero. Once the system was aligned and at focus, all the actuators of the OKO DM were then set to -1 to create defocus and the image plane camera captured and saved the image. All the OKO DM actuators were then set to -0.95 and again the image was captured and saved. This process continued as all the OKO DM actuators were ranged from -1 to 1 in increments of 0.05 and the image was captured at each setting. Once this series of 41 images were saved, the sharpness value of each image was calculated in MatLab. Each image (in the form of .bmp, .tiff, or .jpg) was imported into MatLab and converted to a 640x640 array where each element represented the pixel intensity scaled to values between 0 and 255. The sharpness value for a single image was calculated based on the sharpness metric used and placed in a vector of sharpness values. The next image was then imported and again the sharpness value was calculated and placed in the sharpness vector. This continued until all the images were processed resulting in a 41 element vector of sharpness values.



This sharpness vector contains the sharpness values as the OKO DM cycled from out of focus (value of -1), through focus (value of 0), and continued to move out of focus (value of 1). The defocus Zernike coefficient, measured in waves, for each of the OKO DM actuator values was measured using a Shack Hartmann wavefront sensor (WFS). Figure 7.4 shows the addition of the WFS and the relay lenses to adjust the beam size. Once the defocus Zernike coefficients were measured they were placed in a 41 element vector. The sharpness vector versus the defocus vector was plotted to show how the sharpness value changes as the OKO DM went from defocus, through focus, and back to defocus. These sharpness versus defocus plots will be used to analyze the three sharpness metrics used in this chapter and the sharpness metrics used for coherent imaging in chapter 8.

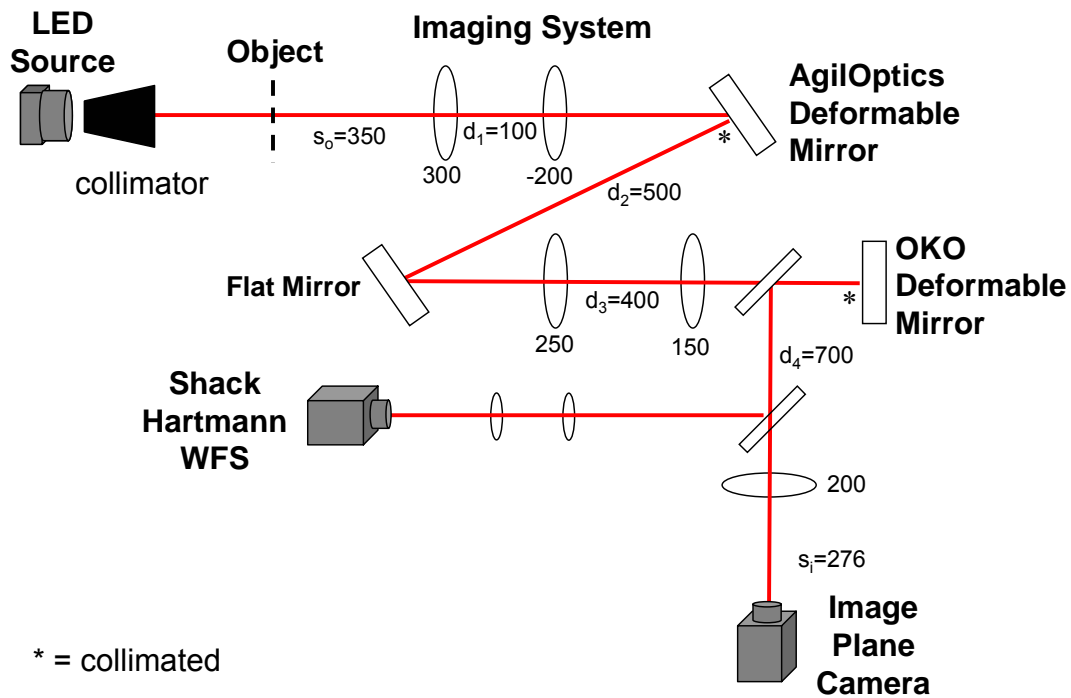


FIGURE 7.4: Experimental schematic with the added Shack Hartmann wavefront sensor.

Object	Image Intensity	Image Fourier Transform Distribution (linear scale)	Image Fourier Transform Distribution (logarithmic scale)
Bar Chart - High Frequency			
Bar Chart - Medium Frequency			
Bar Chart - Low Frequency			
Small Circle Object			
Circle Object			
Star Pattern			

TABLE 7.1: Image plane intensity distributions and digital Fourier transforms on linear and logarithmic scales for an incoherent source and optics table setup.

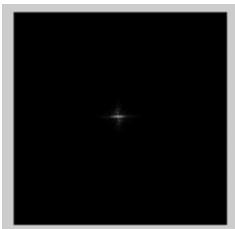
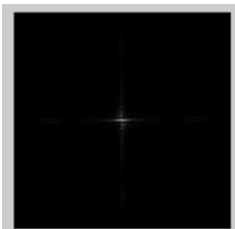
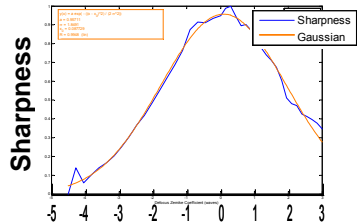
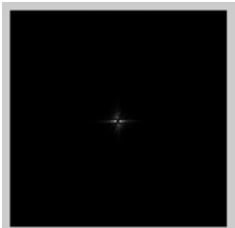
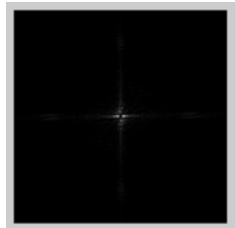
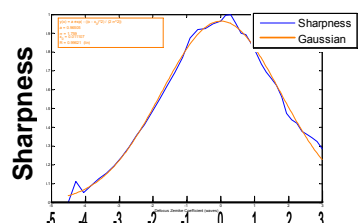

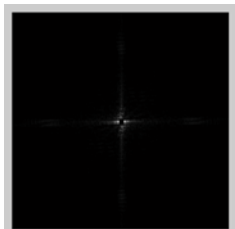
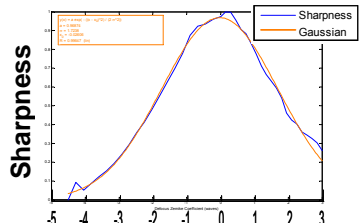

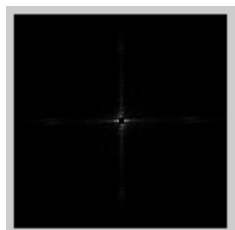
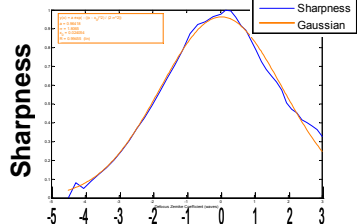
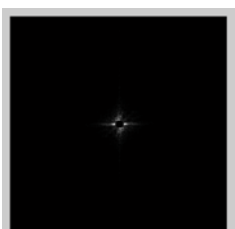
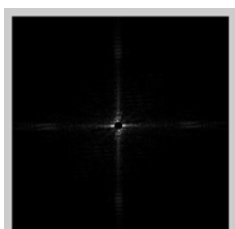
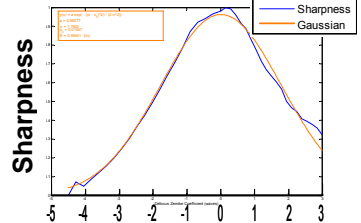
#### 7.4.1 Optics Table Experimental Results

For all optics table configurations in this chapter and in chapter 8, six different objects were used. The images of these six objects can be seen in table 7.1 along with the title with which they will be referred to throughout this dissertation. Also seen in table 7.1 is the Fourier transform, performed digitally with MatLab, of each image on linear and logarithmic scales. A National Bureau of Standards (NBS) 1963A resolution pattern was used to create the first three objects, referred to as “bar chart” objects. The bar chart was positioned such that certain spatial frequencies were in the illumination beam. High, medium, and low frequency titles refer to the relative spatial frequency number that was illuminated where the number identifies the lines per millimeter of the adjacent vertical and horizontal bars. Though one object is referred to as low frequency it is only the spatial frequency of the bars that is lower than the other objects, this object does in fact have high spatial frequencies as there are sharp, high contrast, edges throughout the pattern. The next two objects were created using an iris of two different sizes. “Small circle object” refers to the smallest size of the iris with a diameter of 2 mm and “circle object” refers to an iris with a diameter of 12 mm. Finally the “star pattern” refers to the portion of the star target pattern used that has wedge spacing and spatial frequencies ranging from 0.6 to 14 lines per millimeter.

To measure and compare the sharpness metrics, a series of image plane images was captured and saved as the OKO DM was cycled through the defocus values. Images were obtained for all six objects. Before comparing all three sharpness metrics, the affect of mask size on the sensitivity of  $S_2$ , equation 7.3, first needs to be investigated. To do so the image sharpness values versus defocus were obtained for all six objects using various

mask sizes and sharpness metric  $S_2$ . The mask size is the radius of the circle, measured in pixels, within which the central pixels of the image Fourier transform were set to zero. To compare the sharpness plots for each mask size and see the affect on the sensitivity, the plots were scaled and normalized to a sharpness range of 0 to 1. Once the plots were scaled and normalized they were fitted to a Gaussian from which the standard deviation was calculated. The sensitivity is determined from the standard deviation,  $\sigma$ , where the smaller value represents greater sensitivity. Table 7.2 shows the sharpness versus defocus plots of the medium frequency bar chart object with varying mask sizes. Also shown in table 7.2 are the image Fourier transforms at defocus and focus with the center masked out by the corresponding mask size. These Fourier transform images have been zoomed in to better see the detail at the high spatial frequencies. With the Fourier transform images it should be noted that MatLab automatically normalizes the pixel values to a range of 0 to 1 when performing a gray plot. As the mask size increases, more high spatial frequency detail can be seen as the low spatial frequencies are masked

Looking at the plots in table 7.2, in general as the mask size increases the standard deviation decreases and thus the sensitivity increases. Also it can be seen, especially with larger mask sizes, that the Fourier transforms at focus contain more high spatial frequencies than at defocus and therefore there is a greater sensitivity with the larger mask sizes. This mask size and sensitivity relationship was observed with all six objects and each object and mask size (up to 20) produced an absolute maximum at zero waves defocus. When selecting a mask size, typically the larger size is better, but one must also consider the objects being imaged and the resolution of the optical system. For the following sharpness metric comparisons the  $S_2$  metric uses a mask size of 20 pixels.

Mask Size (pixels)	Masked Fourier Transform at -2.7 waves of Defocus	Masked Fourier Transform at Focus	Sharpness vs. Defocus with Gaussian Fit
1			 <p><b>Sharpness vs. Defocus with Gaussian Fit</b>  <math>\sigma = 1.85</math> <math>R = 0.99</math></p>
2			 <p><b>Sharpness vs. Defocus with Gaussian Fit</b>  <math>\sigma = 1.76</math> <math>R = 0.99</math></p>
3			 <p><b>Sharpness vs. Defocus with Gaussian Fit</b>  <math>\sigma = 1.72</math> <math>R = 0.99</math></p>
4			 <p><b>Sharpness vs. Defocus with Gaussian Fit</b>  <math>\sigma = 1.81</math> <math>R = 0.99</math></p>
5			 <p><b>Sharpness vs. Defocus with Gaussian Fit</b>  <math>\sigma = 1.79</math> <math>R = 0.99</math></p>

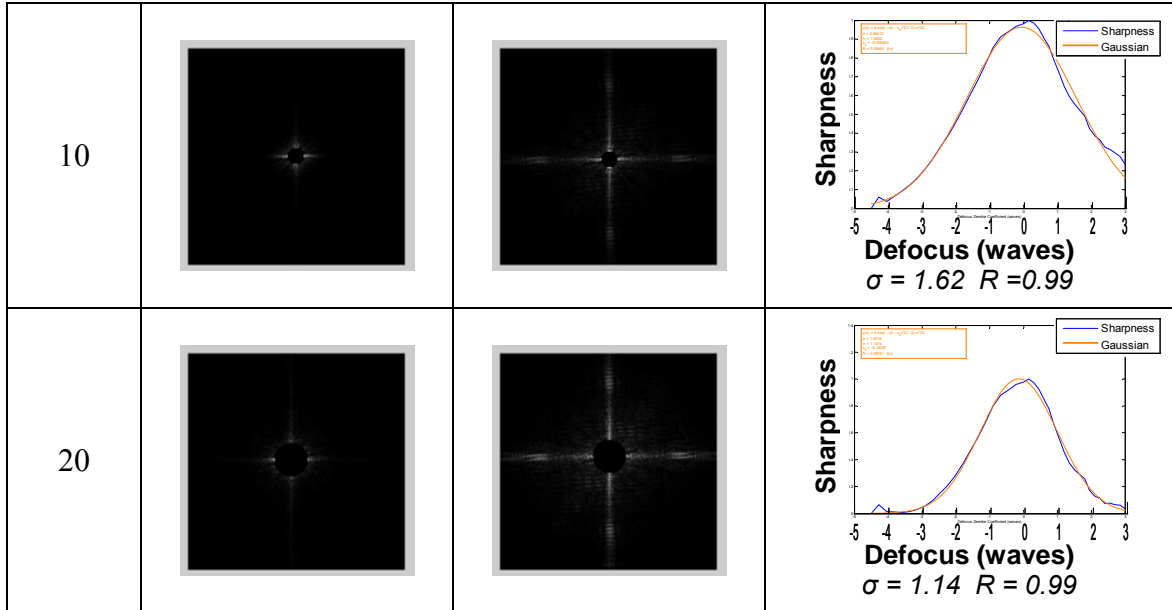


TABLE 7.2:  $S_2$  mask sensitivity for the medium frequency bar chart object illuminated with an incoherent source and optics table setup.

Using the same series of image plane captured images used to investigate the  $S_2$  mask size, the image sharpness values were calculated using the  $S_{i2}$ ,  $S_1$ , and  $S_2$  (mask size of 20 pixels) metrics and plotted versus defocus for all six objects and placed in table 7.3. For comparison all the plots were again scaled and normalized from 0 to 1 and fitted with a Gaussian to find the standard deviation. With the exception of the star pattern, it can be seen that the  $S_2$  metric is the most sensitive with the  $S_{i2}$  metric being the least sensitive. It can be noted for the circle object the  $S_{i2}$  failed to produce a maximum at focus where both the  $S_1$  and  $S_2$  metrics were successful.

Object	$S_{I2} = \frac{\iint I_i^2(x,y) dx dy}{(\iint I_i(x,y) dx dy)^2}$	$S_1 = \frac{\iint  \mathcal{F}\{I_i(x,y)\}  df_x df_y}{\iint I_i(x,y) dx dy}$	$S_2 = \frac{\iint \mathcal{F}\{I_i(x,y)\}_{masked}  df_x df_y }{\iint \mathcal{F}\{I_i(x,y)\}_{unmasked}  df_x df_y }$
Bar Chart – High Frequency	 <b>Sharpness</b> Defocus (waves) $\sigma = 1.85$ $R = 0.98$	 <b>Sharpness</b> Defocus (waves) $\sigma = 1.31$ $R = 0.97$	 <b>Sharpness</b> Defocus (waves) $\sigma = 1.23$ $R = 0.99$
Bar Chart – Medium Frequency	 <b>Sharpness</b> Defocus (waves) $\sigma = 1.47$ $R = 0.97$	 <b>Sharpness</b> Defocus (waves) $\sigma = 1.28$ $R = 0.99$	 <b>Sharpness</b> Defocus (waves) $\sigma = 1.14$ $R = 0.99$
Bar Chart – Low Frequency	 <b>Sharpness</b> Defocus (waves) $\sigma = 1.71$ $R = 0.15$	 <b>Sharpness</b> Defocus (waves) $\sigma = 1.42$ $R = 0.99$	 <b>Sharpness</b> Defocus (waves) $\sigma = 1.17$ $R = 0.99$
Small Circle Object	 <b>Sharpness</b> Defocus (waves) $\sigma = 1.93$ $R = 0.99$	 <b>Sharpness</b> Defocus (waves) $\sigma = 1.41$ $R = 0.97$	 <b>Sharpness</b> Defocus (waves) $\sigma = 1.38$ $R = 0.99$
Circle Object	 <b>Sharpness</b> Defocus (waves)	 <b>Sharpness</b> Defocus (waves) $\sigma = 1.51$ $R = 0.98$	 <b>Sharpness</b> Defocus (waves) $\sigma = 1.30$ $R = 0.99$
Star Pattern	 <b>Sharpness</b> Defocus (waves) $\sigma = 1.31$ $R = 0.95$	 <b>Sharpness</b> Defocus (waves) $\sigma = 1.03$ $R = 0.98$	 <b>Sharpness</b> Defocus (waves) $\sigma = 1.56$ $R = 0.99$

TABLE 7.3: Sharpness vs. defocus plots for an incoherent source and optics table setup. Comparison of the three image plane sharpness metrics.  $S_2$  uses a mask size of 20 pixels.

#### 7.4.2 Telescope Experimental Results

With the telescope experiments the objects are no longer test patterns and circle on the optics table, but extended object scenes as viewed from the laboratory window. Terrestrial objects imaged were at various distances ranging from 80 m up to 5 km. The moon was also imaged at near full phase. Similar to the optics table experiments several images were captured as the system went from defocus, through focus and continued to defocus again. For these experiments the defocus was added by turning the focus knob on the telescope. First the object of interest was brought into focus and then the knob was turned counter clockwise until the image was out of focus. The image was captured and saved before the focus knob was turned slightly in the clockwise direction where this next image was captured and saved. This continued as the focus knob turned through focus and continued on until the image was again out of focus.

The captured images were imported into MatLab where the sharpness value vector was calculated using one of the three sharpness metrics. When plotting the sharpness versus defocus it is difficult to quantize the defocus value since there is no measured scale on the focus knob and no capabilities with the current system to measure defocus using the Shack Hartmann WFS on the telescope. Defocus and focus images were labeled based on visual inspection, not wavefront measurement. An example of this terminology can be seen in figure 7.5 where the images of the UNC Charlotte logo at defocus and focus are shown. For all sharpness versus defocus plots with the telescope setup, the x-axis identifies the image number and has no significant physical meaning.





FIGURE 7.5: Telescope images of the UNC Charlotte logo with the telescope at (a) defocus and (b) focus

Before comparing the three sharpness metrics first the affect of the mask size in metric  $S_2$  must be investigated. Using the UNCC logo, seen in figure 7.5b, the  $S_2$  sharpness values were calculated with digital mask sizes of 1, 2, 3, 4, 5, and 10 pixels. For comparison the sharpness versus defocus plots were scaled, normalized, and fit to a Gaussian where the standard deviation was calculated.

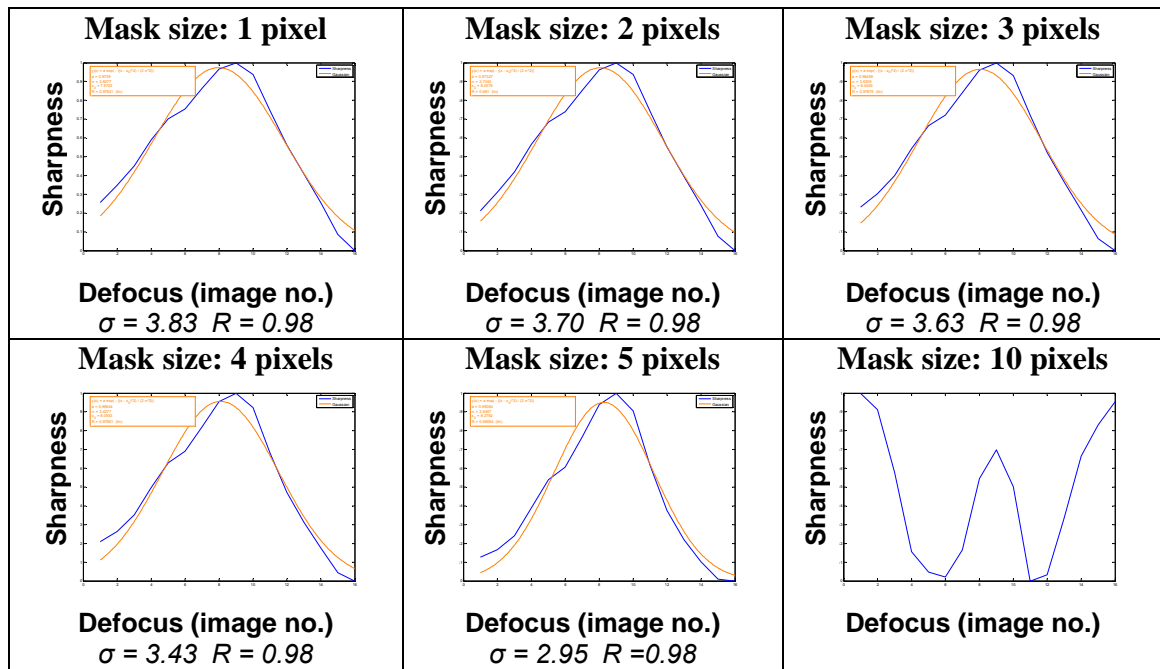

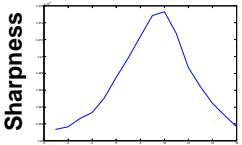
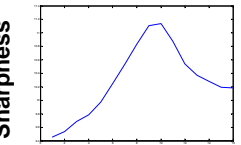
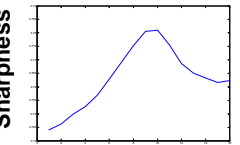
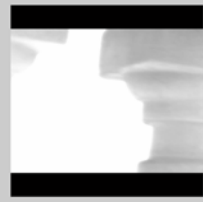
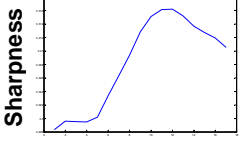
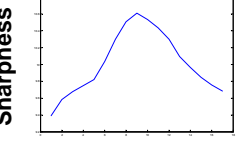
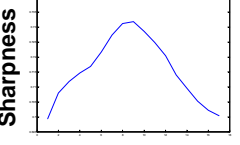

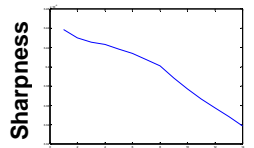
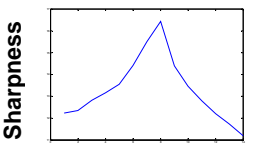
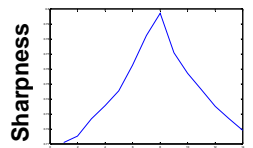

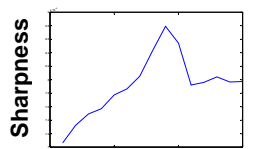
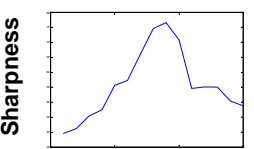
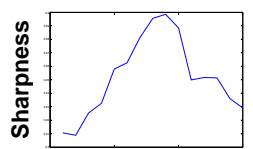
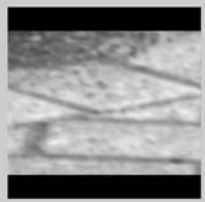
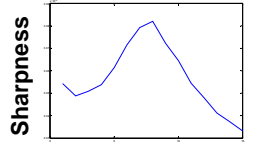
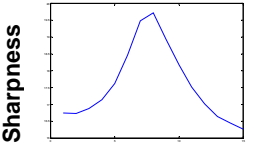
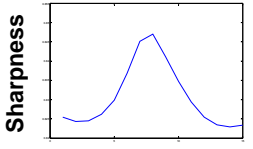

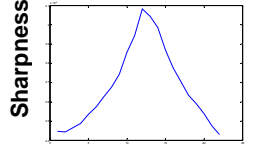
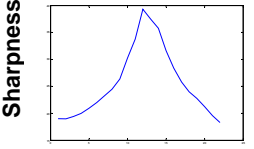
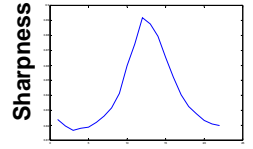
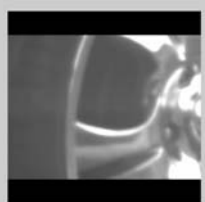
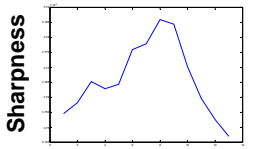
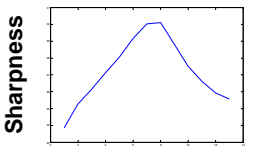
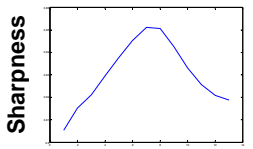



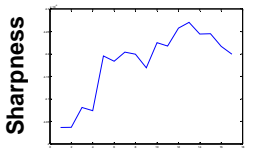
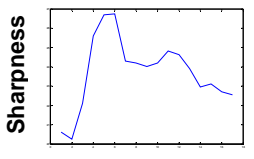
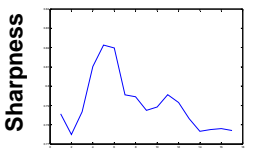
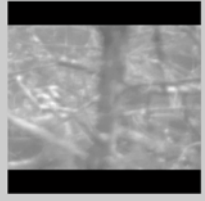
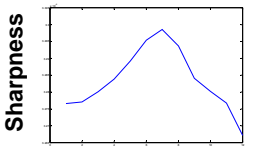
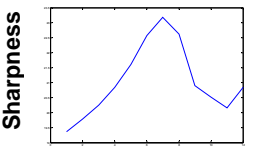
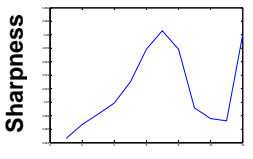

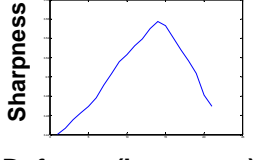
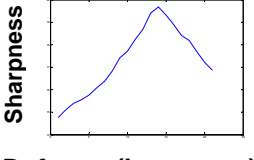
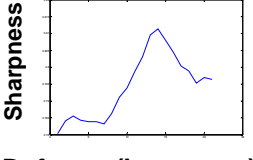

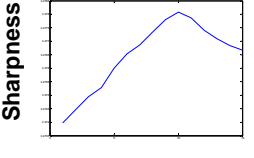
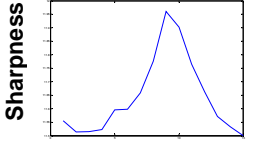
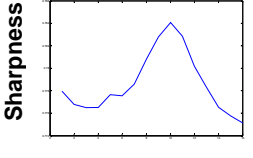

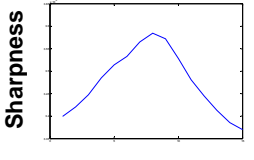
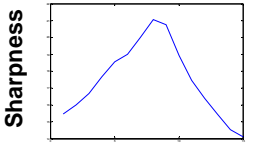
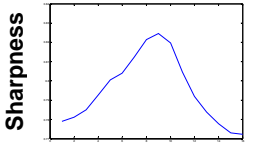
TABLE 7.4:  $S_2$  sharpness vs. defocus plots with various mask sizes for the UNC Charlotte logo object with the telescope setup.

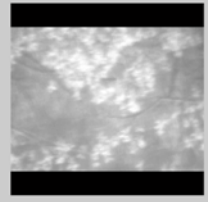
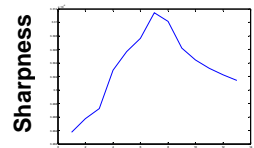
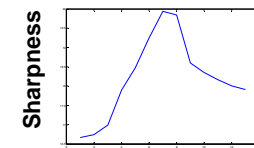
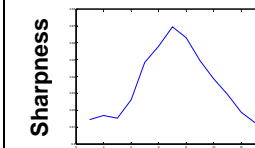
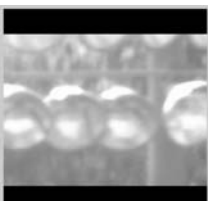
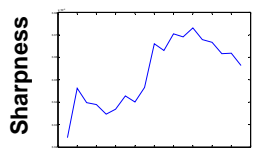
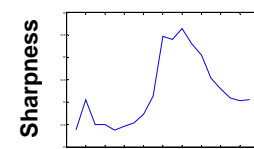
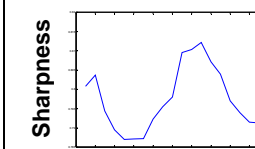
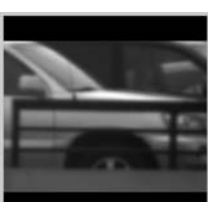
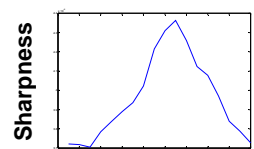
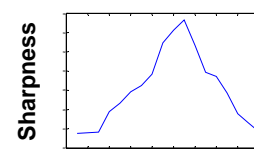
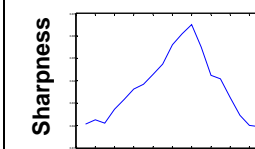

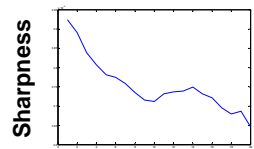
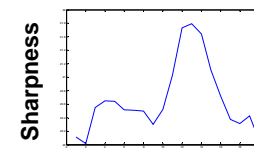
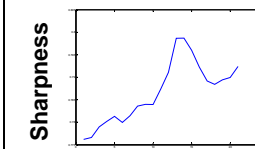

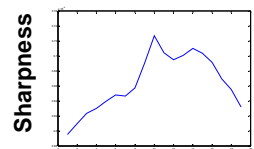
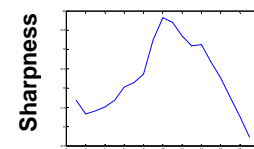
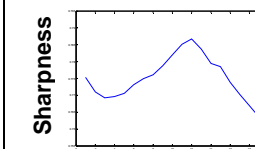
Table 7.4 shows the sharpness versus defocus plots with varying mask size. As the mask size increases the standard deviation decreases and thus the sensitivity increases up until the mask size of 10 pixels where there is no longer an absolute maximum. Unlike the optics table images, the telescope images are limited by the telescope resolution and object contrast causing the edges to be less defined and therefore showing fewer high spatial frequencies. When selecting the mask size, the larger mask size is better within the limitations introduced by the system resolution and object features. A mask size of 5 pixels is used for all the following  $S_2$  sharpness calculations.

The sharpness versus defocus plots using the three sharpness metrics were obtained for several extended objects and placed in table 7.5 for comparison.

Image at $S_1$ Maximum	$S_{i2} = \frac{\iint I_i^2(x, y) dx dy}{\left(\iint I_i(x, y) dx dy\right)^2}$	$S_1 = \frac{\iint  \mathcal{F}\{I_i(x, y)\}  df_x df_y}{\iint I_i(x, y) dx dy}$	$S_2 = \frac{\iint \mathcal{F}\{I_i(x, y)\}_{masked} df_x df_y}{\iint \mathcal{F}\{I_i(x, y)\}_{unmasked} df_x df_y}$
 Blinds Distance 80 m	 Sharpness Defocus (image no.) Maximum at image 10	 Sharpness Defocus (image no.) Maximum at image 10	 Sharpness Defocus (image no.) Maximum at image 10
 Column Distance 80 m	 Sharpness Defocus (image no.) Maximum at image 11	 Sharpness Defocus (image no.) Maximum at image 9	 Sharpness Defocus (image no.) Maximum at image 9

 <p>Lock Distance 80 m</p>	 <p>Sharpness</p> <p><b>Defocus (image no.)</b> <i>No Maximum</i></p>	 <p>Sharpness</p> <p><b>Defocus (image no.)</b> <i>Maximum at image 8</i></p>	 <p>Sharpness</p> <p><b>Defocus (image no.)</b> <i>Maximum at image 8</i></p>
 <p>Lamp Distance 80 m</p>	 <p>Sharpness</p> <p><b>Defocus (image no.)</b> <i>Maximum at image 9</i></p>	 <p>Sharpness</p> <p><b>Defocus (image no.)</b> <i>Maximum at image 9</i></p>	 <p>Sharpness</p> <p><b>Defocus (image no.)</b> <i>Maximum at image 9</i></p>
 <p>Brick Distance 90 m</p>	 <p>Sharpness</p> <p><b>Defocus (image no.)</b> <i>Maximum at image 8</i></p>	 <p>Sharpness</p> <p><b>Defocus (image no.)</b> <i>Maximum at image 8</i></p>	 <p>Sharpness</p> <p><b>Defocus (image no.)</b> <i>Maximum at image 8</i></p>
 <p>Sign Distance 110 m</p>	 <p>Sharpness</p> <p><b>Defocus (image no.)</b> <i>Maximum at image 11</i></p>	 <p>Sharpness</p> <p><b>Defocus (image no.)</b> <i>Maximum at image 11</i></p>	 <p>Sharpness</p> <p><b>Defocus (image no.)</b> <i>Maximum at image 11</i></p>
 <p>Tire Distance 120 m</p>	 <p>Sharpness</p> <p><b>Defocus (image no.)</b> <i>Maximum at image 8</i></p>	 <p>Sharpness</p> <p><b>Defocus (image no.)</b> <i>Maximum at image 8</i></p>	 <p>Sharpness</p> <p><b>Defocus (image no.)</b> <i>Maximum at image 7</i></p>

 <p>Trees &amp; Pole Distance 250 m &amp; 200 m</p>	 <p><b>Defocus (image no.)</b> <i>No Maximum</i></p>	 <p><b>Defocus (image no.)</b> <i>Maximum at image 6 for the trees Maximum at image 11 for the pole</i></p>	 <p><b>Defocus (image no.)</b> <i>Maximum at image 5 for the trees Maximum at image 11 for the pole</i></p>
 <p>Trees Distance 250 m</p>	 <p><b>Defocus (image no.)</b> <i>Maximum at image 7</i></p>	 <p><b>Defocus (image no.)</b> <i>Maximum at image 7</i></p>	 <p><b>Defocus (image no.)</b> <i>Maximum at image 7</i></p>
 <p>Field Light Box Distance 250 m</p>	 <p><b>Defocus (image no.)</b> <i>Maximum at image 14</i></p>	 <p><b>Defocus (image no.)</b> <i>Maximum at image 14</i></p>	 <p><b>Defocus (image no.)</b> <i>Maximum at image 14</i></p>
 <p>Sign lettering Distance 300 m</p>	 <p><b>Defocus (image no.)</b> <i>Maximum at image 11</i></p>	 <p><b>Defocus (image no.)</b> <i>Maximum at image 10</i></p>	 <p><b>Defocus (image no.)</b> <i>Maximum at image 10</i></p>
 <p>UNCC Logo Distance 300 m</p>	 <p><b>Defocus (image no.)</b> <i>Maximum at image 9</i></p>	 <p><b>Defocus (image no.)</b> <i>Maximum at image 9</i></p>	 <p><b>Defocus (image no.)</b> <i>Maximum at image 9</i></p>

 <p>Trees Distance 350 m</p>	 <p>Sharpness</p> <p>Defocus (image no.) Maximum at image 7</p>	 <p>Sharpness</p> <p>Defocus (image no.) Maximum at image 7</p>	 <p>Sharpness</p> <p>Defocus (image no.) Maximum at image 7</p>
 <p>Track Lights Distance 700 m</p>	 <p>Sharpness</p> <p>Defocus (image no.) Maximum at image 15</p>	 <p>Sharpness</p> <p>Defocus (image no.) Maximum at image 13</p>	 <p>Sharpness</p> <p>Defocus (image no.) Maximum at image 13</p>
 <p>Parking Deck Distance 740 m</p>	 <p>Sharpness</p> <p>Defocus (image no.) Maximum at image 12</p>	 <p>Sharpness</p> <p>Defocus (image no.) Maximum at image 12</p>	 <p>Sharpness</p> <p>Defocus (image no.) Maximum at image 12</p>
 <p>Dome Distance 1 km</p>	 <p>Sharpness</p> <p>Defocus (image no.) Local max. at image 15</p>	 <p>Sharpness</p> <p>Defocus (image no.) Maximum at image 14</p>	 <p>Sharpness</p> <p>Defocus (image no.) Maximum at image 14</p>
 <p>Library Distance 1.0 km</p>	 <p>Sharpness</p> <p>Defocus (image no.) Maximum at image 11</p>	 <p>Sharpness</p> <p>Defocus (image no.) Maximum at image 11</p>	 <p>Sharpness</p> <p>Defocus (image no.) Maximum at image 12</p>

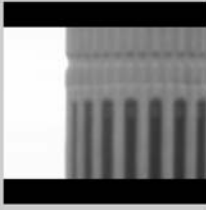
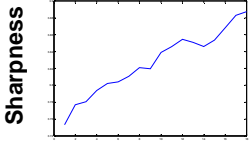
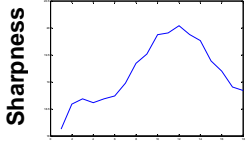
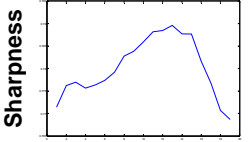

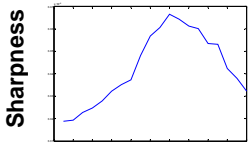
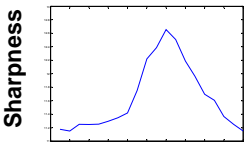
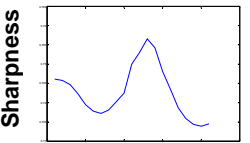
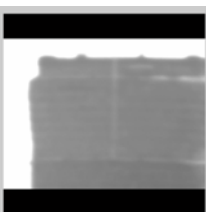
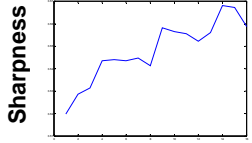
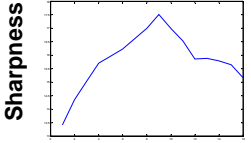
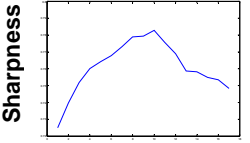

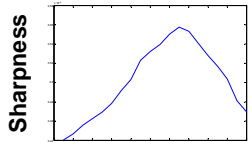
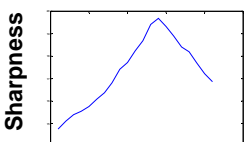
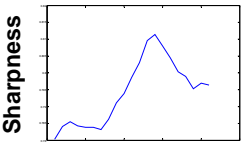

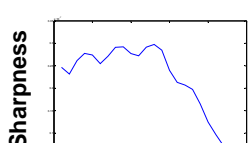
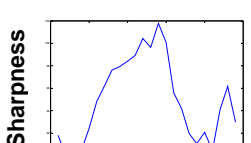
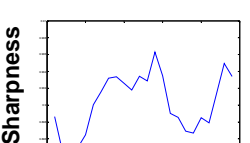
 Belk Tower Distance 1.1 km	 <b>Sharpness</b> <b>Defocus (image no.)</b> <i>Local max. at image</i> 13	 <b>Sharpness</b> <b>Defocus (image no.)</b> <i>Maximum at image</i> 13	 <b>Sharpness</b> <b>Defocus (image no.)</b> <i>Maximum at image</i> 13
 Windows Distance 1.2 km	 <b>Sharpness</b> <b>Defocus (image no.)</b> <i>Maximum at image</i> 13	 <b>Sharpness</b> <b>Defocus (image no.)</b> <i>Maximum at image</i> 13	 <b>Sharpness</b> <b>Defocus (image no.)</b> <i>Maximum at image</i> 13
 Smokestack Distance 1.5 km	 <b>Sharpness</b> <b>Defocus (image no.)</b> <i>Local max. at image</i> 10	 <b>Sharpness</b> <b>Defocus (image no.)</b> <i>Maximum at image</i> 10	 <b>Sharpness</b> <b>Defocus (image no.)</b> <i>Maximum at image</i> 10
 Cell Phone Tower Distance 4.8 km	 <b>Sharpness</b> <b>Defocus (image no.)</b> <i>Maximum at image</i> 14	 <b>Sharpness</b> <b>Defocus (image no.)</b> <i>Maximum at image</i> 14	 <b>Sharpness</b> <b>Defocus (image no.)</b> <i>Maximum at image</i> 14
 Moon Distance: 384400 km	 <b>Sharpness</b> <b>Defocus (image no.)</b> <i>Local max. at image</i> 14	 <b>Sharpness</b> <b>Defocus (image no.)</b> <i>Maximum at image</i> 14	 <b>Sharpness</b> <b>Defocus (image no.)</b> <i>Maximum at image</i> 14

TABLE 7.5.: Sharpness vs. defocus plots for 22 extended objects. Comparison of the three sharpness metrics.  $S_2$  uses a mask size of 5 pixels.

Before comparing and discussing the sharpness versus defocus plots in table 7.5 it should be noted that these plots are not normalized like previous optics table plots and the x-axis has no physical meaning but rather lists the image number. It can be seen for several objects (i.e. lock, trees & pole, dome, belk tower, and smokestack) that the  $S_{i2}$  sharpness metric failed either by having no maximum at focus or only a local maximum. For all objects the  $S_1$  and  $S_2$  Fourier-based metrics successfully produced an absolute maximum at focus. There were some low contrast objects (i.e. column, sign lettering, and track lights) where the  $S_{i2}$  maximum was at different image than the  $S_1$  and  $S_2$  metrics. After visual inspection of the images at the two maximum values, the images at the  $S_1$  and  $S_2$  metric maxima are sharper than the  $S_{i2}$  maximum images. For the trees and pole object there are two local maxima because there are two objects at different object distances within the field of view, the trees and the pole, causing two different “in-focus” positions depending on the object in focus. Each of the two local maxima corresponds to the focus positions of the trees and the pole respectively. In general the Fourier-based sharpness metrics were more robust than the  $S_{i2}$  sharpness metric.

When imaging with the telescope extended objects and scenes were plenty but it was more difficult to locate incoherent point sources. Due to campus light pollution and the limited field of view from the laboratory window it was difficult to image the few visible stars, therefore alternative point sources were needed. The first point source was created by placing a fiber optics white light source in the window of an adjacent building and directing it toward the laboratory window. The second point source was a lamp located on a parking deck that was distant enough that the light structure could not be resolved and thus worked as a point source. Finally the two lights on a distant cell phone

tower worked well for the third point source object. Images of these point source objects at focus can be seen in table 7.6 with their corresponding distances.


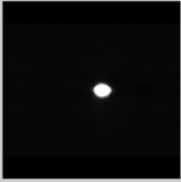

Fiber Optics Lamp Point Source Distance = 90 m	Parking Deck Light Distance = 570 m	Cell Tower Dual Lights Distance = 5.0 km
		

TABLE 7.6: Telescope images of the incoherent point sources at focus.

Sharpness versus defocus plots for the three point sources and the three sharpness metrics (mask size of 5 pixels used for  $S_2$ ) are presented in table 7.7. These plots have been normalized and fitted with a Gaussian to compare the sensitivities of the metrics. Again the Fourier-based sharpness metrics performed better than the  $S_{i2}$  metric. Comparison between the  $S_1$  and  $S_2$  metrics show  $S_2$  has a smaller standard deviation and greater sensitivity than the  $S_1$  metric.



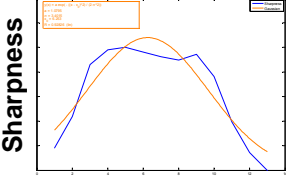
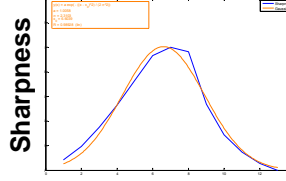
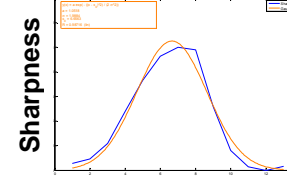
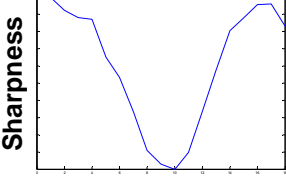
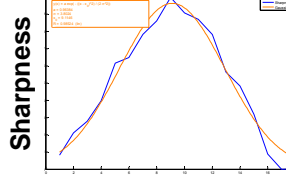
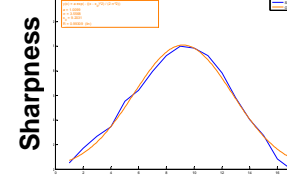
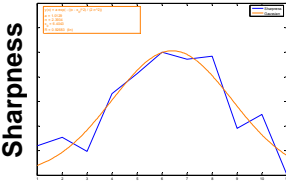
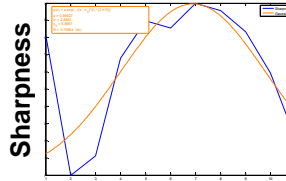
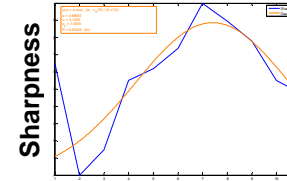
Object	$S_{i2} = \frac{\iint I_i^2(x, y) dx dy}{\left(\iint I_i(x, y) dx dy\right)^2}$	$S_1 = \frac{\iint  \mathcal{F}\{I_i(x, y)\}  df_x df_y}{\iint I_i(x, y) dx dy}$	$S_2 = \frac{\iint \mathcal{F}\{I_i(x, y)\}_{masked}  df_x df_y }{\iint \mathcal{F}\{I_i(x, y)\}_{unmasked}  df_x df_y }$
Fiber Optics Lamp Point Source	 <p>Defocus (image no.) <math>\sigma = 3.40</math> <math>R = 0.93</math></p>	 <p>Defocus (image no.) <math>\sigma = 2.31</math> <math>R = 0.99</math></p>	 <p>Defocus (image no.) <math>\sigma = 1.99</math> <math>R = 0.99</math></p>
Parking Deck Light	 <p>Defocus (image no.)</p>	 <p>Defocus (image no.) <math>\sigma = 3.80</math> <math>R = 0.99</math></p>	 <p>Defocus (image no.) <math>\sigma = 3.56</math> <math>R = 0.99</math></p>
Cell Tower Dual Lights	 <p>Defocus (image no.) <math>\sigma = 2.39</math> <math>R = 0.93</math></p>	 <p>Defocus (image no.) <math>\sigma = 2.89</math> <math>R = 0.76</math></p>	 <p>Defocus (image no.) <math>\sigma = 3.13</math> <math>R = 0.80</math></p>

TABLE 7.7: Sharpness vs. defocus plots for the incoherent point source with the telescope setup. Comparison of the three image plane sharpness metrics.  $S_2$  uses a mask size of 5 pixels.

### 7.4.3 Summary

In this section the sharpness versus defocus plots were created for the optics table and telescope configurations for various incoherently illuminated objects and scenes. In several cases where the  $S_{i2}$  failed to produce an absolute maximum at focus the Fourier-based sharpness metrics were successful. For many objects where all three metrics were successful, the comparison of standard deviations of the Gaussian-fitted plots found  $S_2$  to be the most sensitive whereas  $S_{i2}$  was the least sensitive. To further compare the three metrics the time it took to calculate the sharpness value of a single captured image was

measured and listed in table 7.8. Though the  $S_2$  metric is the most sensitive it requires the longest computing time because of the Fourier transforming and digital masking. When selecting a metric there is a trade off between sensitivity and computing time.

	$S_{i2} = \frac{\iint I_i^2(x, y) dx dy}{\left(\iint I_i(x, y) dx dy\right)^2}$	$S_1 = \frac{\iint  \mathcal{F}\{I_i(x, y)\}  df_x df_y}{\iint I_i(x, y) dx dy}$	$S_2 = \frac{\iint \mathcal{F}\{I_i(x, y)\}_{\text{masked}}   df_x df_y}{\iint \mathcal{F}\{I_i(x, y)\}_{\text{unmasked}}   df_x df_y}$
Computing Time	4.04 s	4.40 s	4.56 s

TABLE 7.8: Computing times of the three image plane sharpness metrics.

Another factor to consider is the mask size used for the  $S_2$  metric. In general, the sensitivity increases as the mask size increases up to the limit created by the system resolution and object contrast. A mask size of 20 pixels was used for the optics table where a mask size of only 5 pixels was used for the telescope experiments. This difference in mask size is attributed to the fact that the optics table objects had higher contrast and thus more high spatial frequencies and a larger mask size limit than the telescope system that was limited by the telescope resolution and scene contrast.

### 7.5 Sharpness versus higher order aberrations

In this section the sharpness values were calculated as higher order aberrations of increasing strength were added. Only the optics table configuration was used since higher order aberrations can not be applied to the telescope in a controlled manner. Higher order aberrations consisted of astigmatism, coma, and spherical aberration and were created with the OKO DM. Using the Shack-Hartmann WFS in the setup in figure 7.4 the mirror was driven to produce the target wavefront of an aberration with a set strength compared to a reference wavefront that included the aberrations of the optical system. For each

aberration the strength ranged from 0 to 2.01 waves with increments of 0.16 waves. This aberration strength range is seen on the x-axis of the following sharpness versus aberration plots. It should be noted that none of the sharpness plots in this section are normalized because there was not a Gaussian shape to fit to. Unlike with defocus where the maximum is toward the center at zero waves defocus, with these plots the maximum should be located at the left side of the plot as the aberration strength ranges from 0 to 2.01 waves.

Sharpness versus aberration strength plots for all three sharpness metrics and all objects can be seen in table 7.9, 7.10, and 7.11 for astigmatism, coma, and spherical aberration respectively. A mask size of 20 pixels was used for sharpness metric  $S_2$ .

Looking at the astigmatism plots for the small circle object, the  $S_2$  metric produced an absolute maximum at 0 waves of astigmatism where both  $S_{i2}$  and  $S_1$  failed. The intensity squared metric,  $S_{i2}$ , failed with the high frequency bar chart and circle object where both the Fourier-based metrics were successful. For coma again the  $S_2$  metric was successful for all objects where  $S_{i2}$  and  $S_1$  both failed to produce an absolute maximum at zero waves of coma for the low frequency bar chart object and the two circle objects. Looking at the plots in table 7.11 with spherical aberration, none of the metrics worked for the small circle object. As with the other aberrations the  $S_2$  metric performs the best at producing an absolute maximum at zero waves of aberration. It can be seen that these metrics were successful with higher order aberrations though they do not work as well as they did with defocus because local maxima were more frequent. Sharpness measurements with higher aberrations are limited by the capability of the deformable

mirror to apply the desired aberration on the wavefront where defocus is easier to create by setting all actuator voltages to the same value.

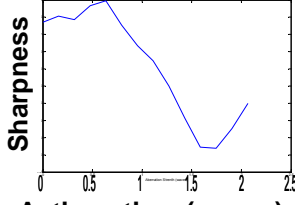
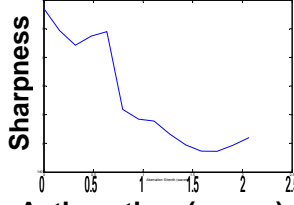
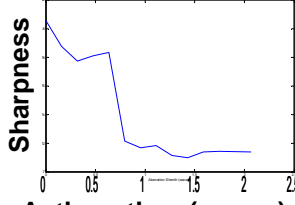
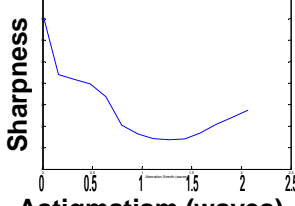
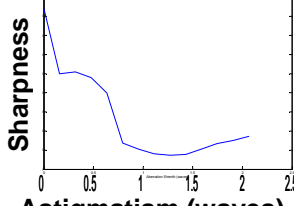
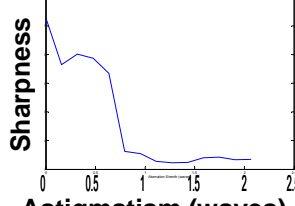
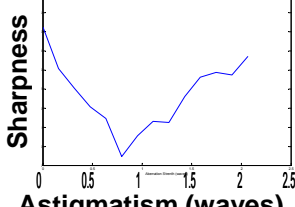
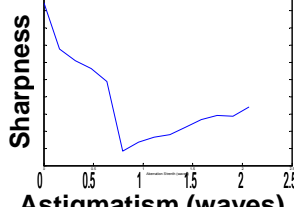
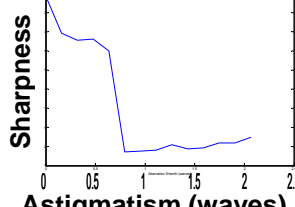
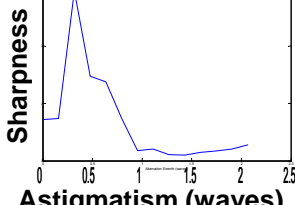
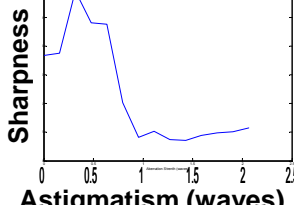
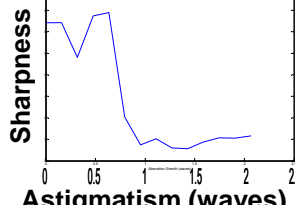
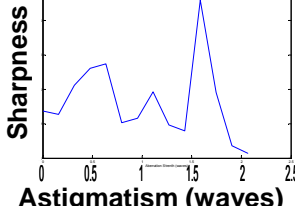
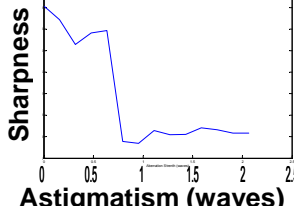
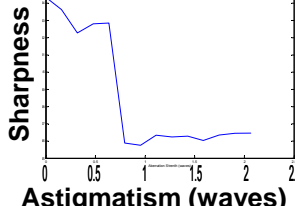
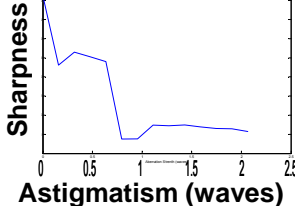
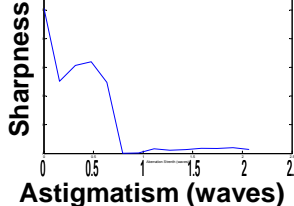
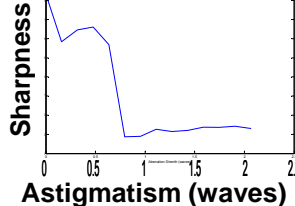
Object	$S_{i2} = \frac{\iint I_i^2(x,y) dx dy}{(\iint I_i(x,y) dx dy)^2}$	$S_1 = \frac{\iint  \mathcal{F}\{I_i(x,y)\}  df_x df_y}{\iint I_i(x,y) dx dy}$	$S_2 = \frac{\iint \mathcal{F}\{I_i(x,y)\}_{masked} df_x df_y}{\iint \mathcal{F}\{I_i(x,y)\}_{unmasked} df_x df_y}$
Bar Chart - High Frequency			
Bar Chart - Medium Frequency			
Bar Chart - Low Frequency			
Small Circle Object			
Circle Object			
Star Pattern			

TABLE 7.9: Sharpness vs. astigmatism plots for an incoherent source and optics table setup. Comparison of the three image plane sharpness metrics.  $S_2$  uses a mask size of 80 pixels.

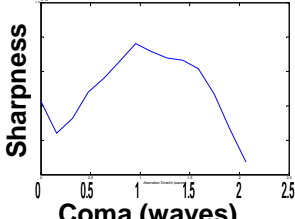
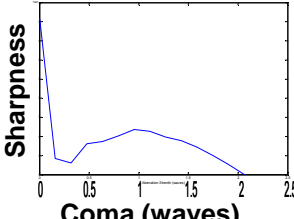
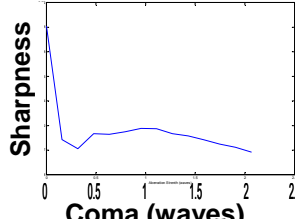
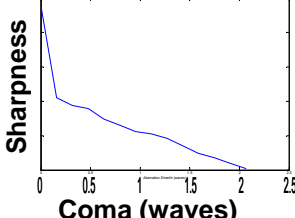
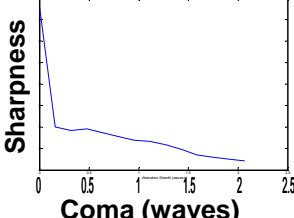
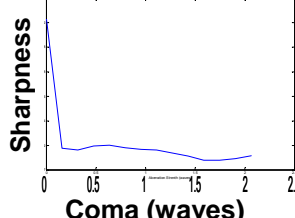
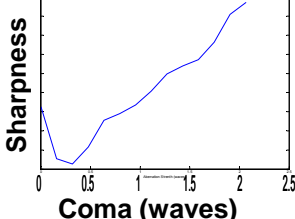
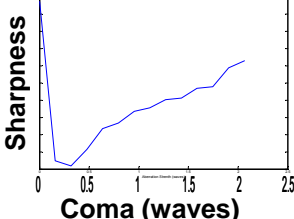
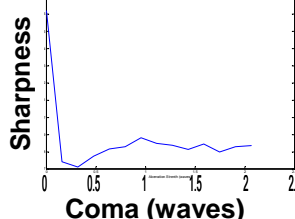
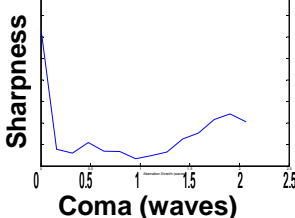
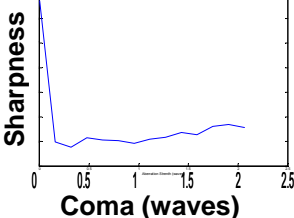
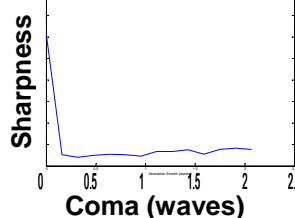
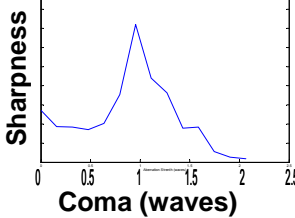
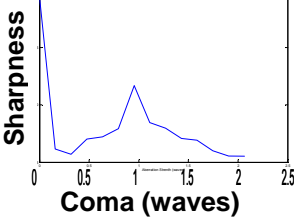
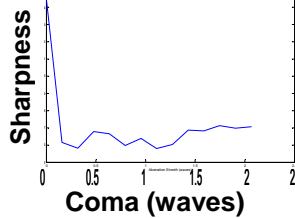
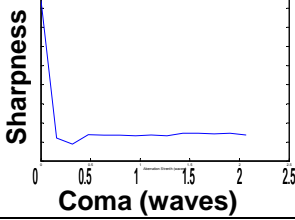
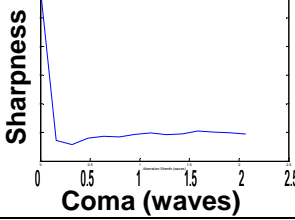
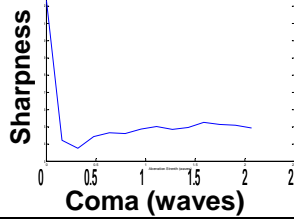
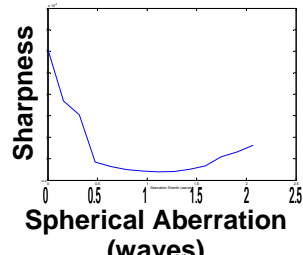
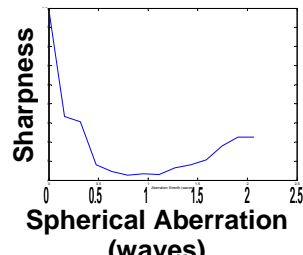
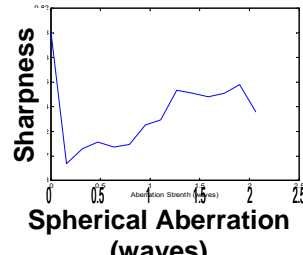
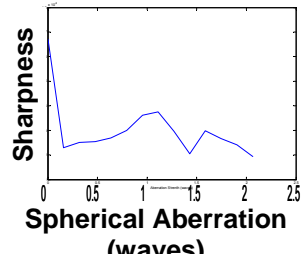
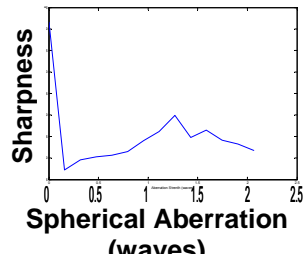
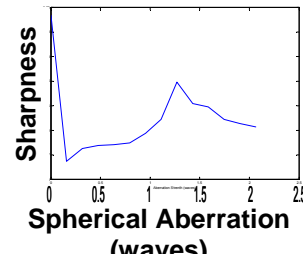
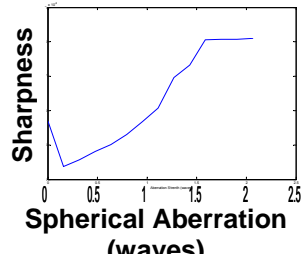
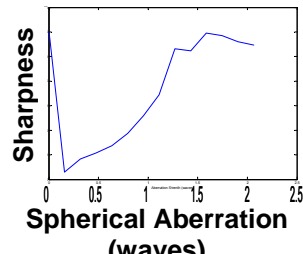
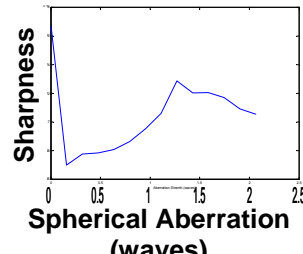
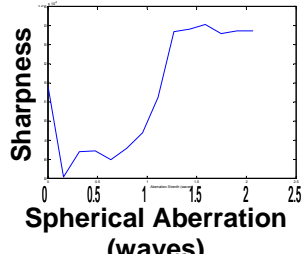
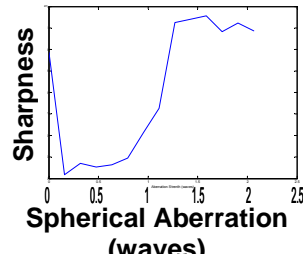
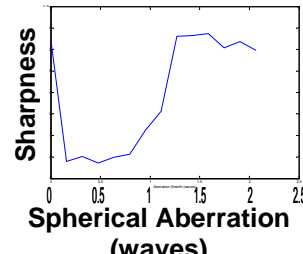
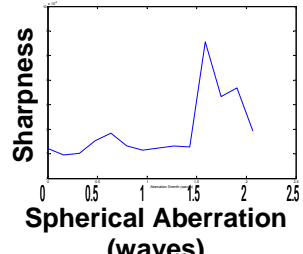
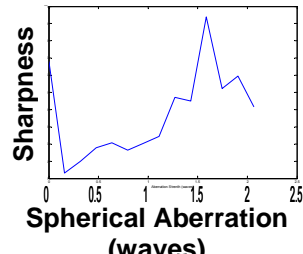
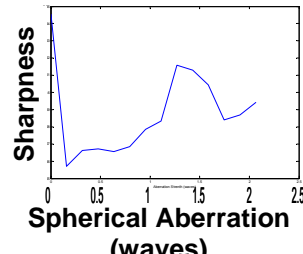
Object	$S_{i2} = \frac{\iint I_i^2(x, y) dx dy}{\left(\iint I_i(x, y) dx dy\right)^2}$	$S_1 = \frac{\iint  \mathcal{F}\{I_i(x, y)\}  df_x df_y}{\iint I_i(x, y) dx dy}$	$S_2 = \frac{\iint  \mathcal{F}\{I_i(x, y)\}_{masked}  df_x df_y}{\iint  \mathcal{F}\{I_i(x, y)\}_{unmasked}  df_x df_y}$
Bar Chart - High Frequency			
Bar Chart - Medium Frequency			
Bar Chart - Low Frequency			
Small Circle Object			
Circle Object			
Star Pattern			

TABLE 7.10: Sharpness vs. coma plots for an incoherent source and optics table setup. Comparison of the three image plane sharpness metrics.  $S_2$  uses a mask size of 20 pixels.

Object	$S_{I_2} = \frac{\iint I_i^2(x, y) dx dy}{\left(\iint I_i(x, y) dx dy\right)^2}$	$S_1 = \frac{\iint  \mathcal{F}\{I_i(x, y)\}  df_x df_y}{\iint I_i(x, y) dx dy}$	$S_2 = \frac{\iint \mathcal{F}\{I_i(x, y)\}_{\text{masked}}  df_x df_y }{\iint \mathcal{F}\{I_i(x, y)\}_{\text{unmasked}}  df_x df_y }$
Bar Chart - High Frequency	 <p>Sharpness</p> <p>Spherical Aberration (waves)</p>	 <p>Sharpness</p> <p>Spherical Aberration (waves)</p>	 <p>Sharpness</p> <p>Spherical Aberration (waves)</p>
Bar Chart - Medium Frequency	 <p>Sharpness</p> <p>Spherical Aberration (waves)</p>	 <p>Sharpness</p> <p>Spherical Aberration (waves)</p>	 <p>Sharpness</p> <p>Spherical Aberration (waves)</p>
Bar Chart - Low Frequency	 <p>Sharpness</p> <p>Spherical Aberration (waves)</p>	 <p>Sharpness</p> <p>Spherical Aberration (waves)</p>	 <p>Sharpness</p> <p>Spherical Aberration (waves)</p>
Small Circle Object	 <p>Sharpness</p> <p>Spherical Aberration (waves)</p>	 <p>Sharpness</p> <p>Spherical Aberration (waves)</p>	 <p>Sharpness</p> <p>Spherical Aberration (waves)</p>
Circle Object	 <p>Sharpness</p> <p>Spherical Aberration (waves)</p>	 <p>Sharpness</p> <p>Spherical Aberration (waves)</p>	 <p>Sharpness</p> <p>Spherical Aberration (waves)</p>

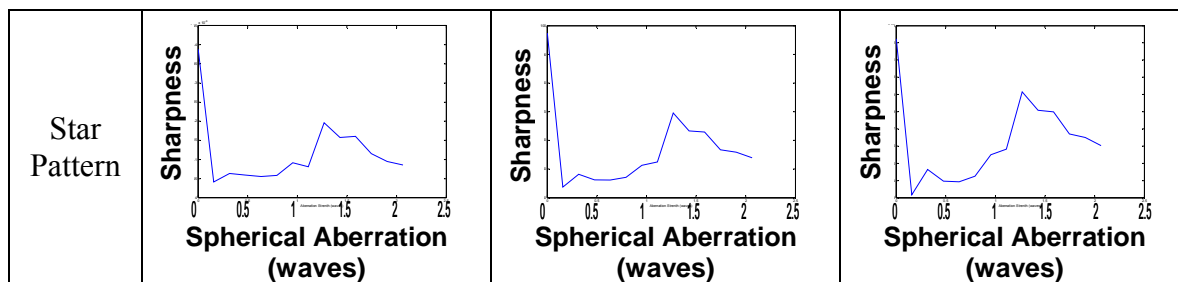


TABLE 7.11: Sharpness vs. spherical aberration plots for an incoherent source and optics table setup. Comparison of the three image plane sharpness metrics.  $S_2$  uses a mask size of 20 pixels.

















## 7.6 Performance in a closed-loop system

To see the potential of these three image sharpness metrics in a closed-loop system, they were used in a manual closed-loop system. With the optics table setup the image plane camera was moved to an arbitrary location out of focus but close enough to focus to allow correction with the OKO deformable mirror (DM). Initially all the OKO DM actuator values were set to zero and the sharpness value was calculated from the captured image using all three metrics and noted. All the OKO DM actuator values were decreased by an increment of 0.05 and the image was recorded and sharpness values were calculated. If the sharpness value increased then the OKO DM actuator values continued to decrease by an increment of 0.05; if the sharpness value decreased then the actuator values were increased. This continued until there the sharpness value reached a maximum.

The first closed-loop experiment used the high frequency bar chart object with the optics table setup. In table 7.12 each captured image is listed with its corresponding sharpness values and OKO DM actuator setting. Local maxima of the sharpness values are indicated with *italics* and absolute maxima are indicated with **bold text**. For this run the actuator increments were initially 0.05. Once a maximum was passed, the increments



were shortened to 0.01 to find a more accurate actuator setting. Visibly it is difficult to see much change in images within an actuator value of 0.1 of the maximum. It should be noted that both  $S_1$  and  $S_2$  are in agreement of the absolute value of 0.41 where  $S_{i2}$  found and absolute value of 0.38.

 <p> <math>S_{i2} = 5.282 \times 10^{-6}</math>  <math>S_1 = 63.05</math>  <math>S_2 = 0.661</math>            OKO Actuator = 0         </p>	 <p> <math>S_{i2} = 5.22 \times 10^{-6}</math>  <math>S_1 = 59.44</math>  <math>S_2 = 0.646</math>            OKO Actuator = -.05         </p>	 <p> <math>S_{i2} = 5.352 \times 10^{-6}</math>  <math>S_1 = 66.83</math>  <math>S_2 = 0.676</math>            OKO Actuator = .05         </p>	 <p> <math>S_{i2} = 5.421 \times 10^{-6}</math>  <math>S_1 = 74.22</math>  <math>S_2 = 0.707</math>            OKO Actuator = .1         </p>
 <p> <math>S_{i2} = 5.473 \times 10^{-6}</math>  <math>S_1 = 79.55</math>  <math>S_2 = 0.726</math>            OKO Actuator = .15         </p>	 <p> <math>S_{i2} = 5.527 \times 10^{-6}</math>  <math>S_1 = 87.38</math>  <math>S_2 = 0.751</math>            OKO Actuator = .2         </p>	 <p> <math>S_{i2} = 5.586 \times 10^{-6}</math>  <math>S_1 = 95.72</math>  <math>S_2 = 0.772</math>            OKO Actuator = .25         </p>	 <p> <math>S_{i2} = 5.636 \times 10^{-6}</math>  <math>S_1 = 103.55</math>  <math>S_2 = 0.789</math>            OKO Actuator = .3         </p>
 <p> <math>S_{i2} = 5.658 \times 10^{-6}</math>  <math>S_1 = 109.08</math>  <math>S_2 = 0.801</math>            OKO Actuator = .35         </p>	 <p> <math>S_{i2} = 5.637 \times 10^{-6}</math>  <math>S_1 = 111.89</math>  <math>S_2 = \mathbf{0.807}</math>            OKO Actuator = .4         </p>	 <p> <math>S_{i2} = 5.612 \times 10^{-6}</math>  <math>S_1 = 107.01</math>  <math>S_2 = 0.798</math>            OKO Actuator = .45         </p>	 <p> <math>S_{i2} = 5.623 \times 10^{-6}</math>  <math>S_1 = 108.72</math>  <math>S_2 = 0.801</math>            OKO Actuator = .44         </p>
 <p> <math>S_{i2} = 5.631 \times 10^{-6}</math>  <math>S_1 = 108.73</math>  <math>S_2 = 0.801</math>            OKO Actuator = .43         </p>	 <p> <math>S_{i2} = 5.617 \times 10^{-6}</math>  <math>S_1 = 110.08</math>  <math>S_2 = 0.804</math>            OKO Actuator = .42         </p>	 <p> <math>S_{i2} = 5.635 \times 10^{-6}</math>  <math>S_1 = \mathbf{112.18}</math>  <math>S_2 = \mathbf{0.807}</math>            OKO Actuator = .41         </p>	 <p> <math>S_{i2} = 5.655 \times 10^{-6}</math>  <math>S_1 = 110.40</math>  <math>S_2 = 0.804</math>            OKO Actuator = .40         </p>

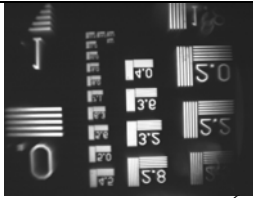
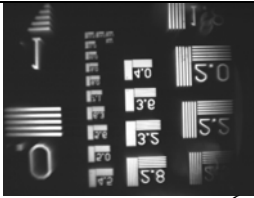
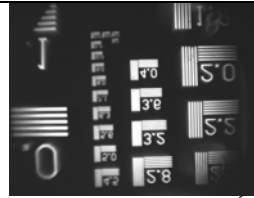
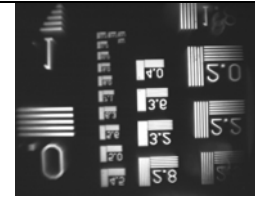
			
$S_{i2} = 5.662 \times 10^{-6}$ $S_1 = 110.78$ $S_2 = 0.804$ OKO Actuator = .39	$S_{i2} = \mathbf{5.672 \times 10^{-6}}$ $S_1 = 111.31$ $S_2 = 0.805$ OKO Actuator = .38	$S_{i2} = 5.671 \times 10^{-6}$ $S_1 = 111.12$ $S_2 = 0.802$ OKO Actuator = .37	$S_{i2} = 5.666$ $S_1 = 109.99$ $S_2 = 0.802$ OKO Actuator = .36

TABLE 7.12: Closed-loop images for the high frequency bar chart object on the optics table with an incoherent source. Mask size of 20 pixels used for  $S_2$ .

For the telescope setup the telescope was directed at an unknown object out of focus. Similar to the previous closed-loop, the sharpness value was calculated and recorded. Then the focus knob was turned slightly one direction and a new image was captured and the sharpness value was measured. If the sharpness increased the knob continued to turn in that direction, otherwise the direction was reversed. Since there is no scale on the focus knob there is no quantized defocus value. The closed-loop on the telescope was performed on three objects and can be seen in tables 7.13, 7.14, and 7.15. The direction listed was the direction the focus knob was turned after the sharpness values were calculated for the corresponding image. Local maxima are identified with italics and absolute maximum with bold. There was agreement between the Fourier-based sharpness metrics,  $S_1$  and  $S_2$ , and the maximum sharpness but some disagreement with the  $S_{i2}$  maximum sharpness value. It should be noted that the tree images are different due to the motion of the trees yet the sharpness metrics were still successful. According to the shift theorem, equation 5.5, a translation in the image spatial plane causes as phase shift in the image Fourier plane. The phase shift information is lost when

the modulus is taken to calculate the sharpness value. Therefore image motion has no impact on the sharpness values as long as the object stays in the field of view.






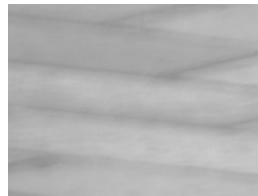






 $S_{i2} = 3.2659 \times 10^{-6}$ $S_1 = 12.11$ $S_2 = 0.7962$ Image Number 1 Counterclockwise	 $S_{i2} = 3.2653 \times 10^{-6}$ $S_1 = 11.69$ $S_2 = 0.7894$ Image Number 2 Clockwise	 $S_{i2} = 3.2660 \times 10^{-6}$ $S_1 = 11.84$ $S_2 = 0.7911$ Image Number 3 Clockwise	 $S_{i2} = 3.2702 \times 10^{-6}$ $S_1 = 13.09$ $S_2 = 0.8097$ Image Number 4 Clockwise
 $S_{i2} = 3.2718 \times 10^{-6}$ $S_1 = 13.29$ $S_2 = 0.8120$ Image Number 5 Clockwise	 $S_{i2} = 3.2687 \times 10^{-6}$ $S_1 = 12.16$ $S_2 = 0.7945$ Image Number 6 Counterclockwise	 $S_{i2} = 3.2685 \times 10^{-6}$ $S_1 = 12.24$ $S_2 = 0.7964$ Image Number 7 Counterclockwise	 $S_{i2} = 3.2702 \times 10^{-6}$ $S_1 = 12.63$ $S_2 = 0.8030$ Image Number 8 Counterclockwise
 $S_{i2} = 3.2715 \times 10^{-6}$ $S_1 = 13.17$ $S_2 = 0.8113$ Image Number 9 Counterclockwise	 $S_{i2} = \mathbf{3.2721 \times 10^{-6}}$ $S_1 = 13.85$ $S_2 = 0.8208$ Image Number 10 Counterclockwise	 $S_{i2} = 3.2713 \times 10^{-6}$ $S_1 = \mathbf{13.96}$ $S_2 = \mathbf{0.8224}$ Image Number 11 Counterclockwise	 $S_{i2} = 3.2702 \times 10^{-6}$ $S_1 = 13.43$ $S_2 = 0.8154$ Image Number 12 Counterclockwise

TABLE 7.13: Closed-loop images of brick located at a distance of about 60 m taken with the telescope. Image plane sharpness metrics used. Mask size of 5 pixels used for  $S_2$ .








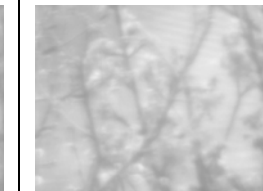
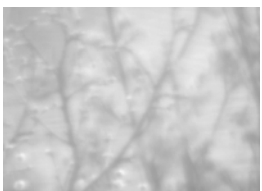
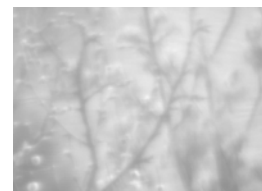


 $S_{i2} = 3.2644 \times 10^{-6}$ $S_1 = 9.99$ $S_2 = 0.7539$ Image Number 1 Counterclockwise	 $S_{i2} = 3.2611 \times 10^{-6}$ $S_1 = 9.76$ $S_2 = 0.7537$ Image Number 2 Clockwise	 $S_{i2} = 3.2607 \times 10^{-6}$ $S_1 = 9.86$ $S_2 = 0.7562$ Image Number 3 Clockwise	 $S_{i2} = 3.2623 \times 10^{-6}$ $S_1 = 10.20$ $S_2 = 0.7585$ Image Number 4 Clockwise
 $S_{i2} = 3.2659 \times 10^{-6}$ $S_1 = 10.68$ $S_2 = 0.7629$ Image Number 5 Clockwise	 $S_{i2} = 3.2820 \times 10^{-6}$ $S_1 = 12.22$ $S_2 = 0.7876$ Image Number 6 Clockwise	 $S_{i2} = 3.2736 \times 10^{-6}$ $S_1 = 11.90$ $S_2 = 0.7807$ Image Number 7 Counterclockwise	 $S_{i2} = 3.2805 \times 10^{-6}$ $S_1 = 12.95$ $S_2 = 0.7917$ Image Number 8 Counterclockwise
 $S_{i2} = 3.2764 \times 10^{-6}$ $S_1 = 12.67$ $S_2 = 0.7915$ Image Number 9 Counterclockwise	 $S_{i2} = \mathbf{3.2802 \times 10^{-6}}$ $S_1 = 12.91$ $S_2 = 0.7974$ Image Number 10 Clockwise	 $S_{i2} = 3.2749 \times 10^{-6}$ $S_1 = \mathbf{13.23}$ $S_2 = \mathbf{0.8033}$ Image Number 11 Clockwise	 $S_{i2} = 3.2751 \times 10^{-6}$ $S_1 = 12.72$ $S_2 = 0.7967$ Image Number 12 Clockwise

TABLE 7.14: Closed-loop images of trees located at a distance of about 300 m taken with the telescope. Image plane sharpness metrics used. Mask size of 5 pixels used for  $S_2$ .

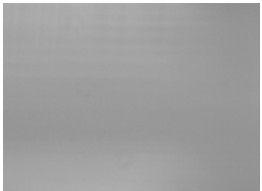



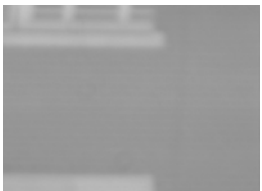
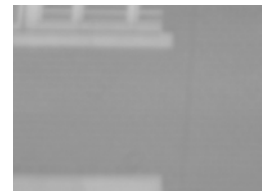
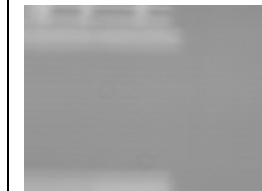
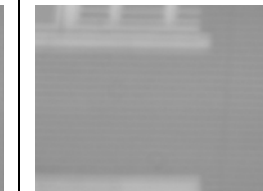
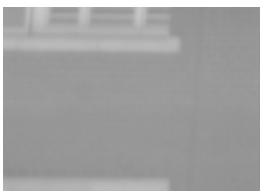
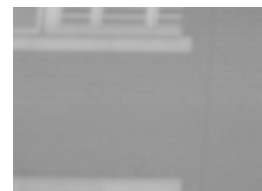
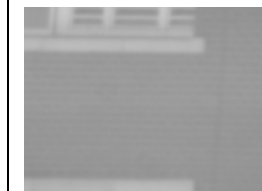
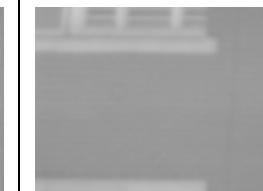
 <p> <math>S_{i2} = 3.2617 \times 10^{-6}</math>  <math>S_1 = 10.74</math>  <math>S_2 = 0.7750</math>            Image Number 1            Counterclockwise         </p>	 <p> <math>S_{i2} = 3.2632 \times 10^{-6}</math>  <math>S_1 = 11.01</math>  <math>S_2 = 0.7776</math>            Image Number 2            Counterclockwise         </p>	 <p> <math>S_{i2} = 3.2647 \times 10^{-6}</math>  <math>S_1 = 11.19</math>  <math>S_2 = 0.7778</math>            Image Number 3            Counterclockwise         </p>	 <p> <math>S_{i2} = 3.2685 \times 10^{-6}</math>  <math>S_1 = 11.54</math>  <math>S_2 = 0.7807</math>            Image Number 4            Counterclockwise         </p>
 <p> <math>S_{i2} = 3.2698 \times 10^{-6}</math>  <math>S_1 = 11.82</math>  <math>S_2 = 0.7854</math>            Image Number 5            Counterclockwise         </p>	 <p> <math>S_{i2} = 3.2700 \times 10^{-6}</math>  <math>S_1 = 11.96</math>  <math>S_2 = 0.7879</math>            Image Number 6            Counterclockwise         </p>	 <p> <math>S_{i2} = 3.2683 \times 10^{-6}</math>  <math>S_1 = 11.64</math>  <math>S_2 = 0.7827</math>            Image Number 7            Clockwise         </p>	 <p> <math>S_{i2} = 3.2699 \times 10^{-6}</math>  <math>S_1 = 11.83</math>  <math>S_2 = 0.7865</math>            Image Number 8            Clockwise         </p>
 <p> <math>S_{i2} = 3.2710 \times 10^{-6}</math>  <math>S_1 = 12.01</math>  <math>S_2 = 0.7900</math>            Image Number 9            Clockwise         </p>	 <p> <math>S_{i2} = 3.2713 \times 10^{-6}</math>  <math>S_1 = 12.07</math>  <math>S_2 = 0.7912</math>            Image Number 10            Clockwise         </p>	 <p> <math>S_{i2} = \mathbf{3.2716 \times 10^{-6}}</math>  <math>S_1 = \mathbf{12.08}</math>  <math>S_2 = \mathbf{0.7917}</math>            Image Number 11            Clockwise         </p>	 <p> <math>S_{i2} = 3.2710 \times 10^{-6}</math>  <math>S_1 = 11.93</math>  <math>S_2 = 0.7891</math>            Image Number 12            Clockwise         </p>

TABLE 7.15 Closed-loop images of a window located at a distance of about 1 km taken with the telescope. Image plane sharpness metrics used. Mask size of 5 pixels used for  $S_2$ .

These preliminary results in this slow and manual closed-loop system show promise for the sharpness metrics to perform successfully in a automatic, closed-loop adaptive optics system.

## 7.7 Conclusions

In this chapter the performance of three sharpness metrics  $S_{i2}$ ,  $S_1$ , and  $S_2$  in an incoherent imaging system were investigated and compared. Two incoherent configurations were used, the optics table and telescope setups. First, the three metrics were compared by only applying defocus to the system by using the OKO DM in the optical table setup and the defocus knob in the telescope setup. As mask size used for  $S_2$  increases so does the sensitivity of the metric up to an upper limit determined by the scene contrast and optical system resolution. Comparison of the three metrics found the Fourier-based metrics  $S_1$  and  $S_2$  to perform with greater robustness and sensitivity than the intensity squared  $S_{i2}$  metric. Between the two Fourier-based metrics the  $S_2$  metric often had greater sensitivity than  $S_1$ . The drawback of the Fourier-based metrics is that the calculation time is longer because the Fourier transform is found digitally.

Higher order aberrations were then applied to compare the metric performances. It was found that though the sharpness metrics did not perform as well as with defocus only, the sharpness metrics often had a maximum sharpness value at zero waves of a given aberration.

Finally the metrics were implemented in a preliminary, manual, closed-loop system. Though this system was manual, slow, and did not use a search algorithm, the preliminary results show promise of the sharpness metrics succeeding in a closed-loop adaptive optics system.

## CHAPTER 8: PERFORMANCE OF THE FOURIER-BASED IMAGE SHARPNESS SENSOR IN COHERENT IMAGING

### 8.1 Introduction

This chapter will investigate the performance of the Fourier-based sharpness metrics in a coherent imaging system. Like in the previous chapter, the sharpness values will be measured as aberrations are added to the system based on the sharpness metrics being investigated. All five sharpness metrics are used in coherent imaging and discussed in sections 8.2. Section 8.3 describes the coherent optical configurations depending on the sharpness metric used. To study the effect of adding aberration, defocus was first added and the sharpness value is measured versus defocus and presented in section 8.4 where the performance of all metrics are shown and compared. Higher order aberrations are later added in section 8.5 to see how the sharpness metric behaves as the aberration strength increases. The sharpness metrics are then implemented in a simple and manual closed-loop system in section 8.6.

### 8.2 Sharpness Metrics

The first three sharpness metrics,

$$S_{i2} = \frac{\iint I_i^2(x, y) dx dy}{\left(\iint I_i(x, y) dx dy\right)^2} = \frac{\sum I_i^2(x, y)}{\left(\sum I_i(x, y)\right)^2} \quad (8.1)$$

$$S_1 = \frac{\iint |\mathcal{F}\{I_i(x, y)\}| df_x df_y}{\iint I_i(x, y) dx dy} = \frac{\sum |\mathcal{F}\{I_i(x, y)\}|}{\sum I_i(x, y)} \quad (8.2)$$

$$S_2 = \frac{\iint |\mathcal{F}\{I_i(x, y)\}_{masked}| df_x df_y}{\iint |\mathcal{F}\{I_i(x, y)\}_{unmasked}| df_x df_y} = \frac{\sum |\mathcal{F}\{I_i(x, y)\}_{masked}|}{\sum |\mathcal{F}\{I_i(x, y)\}_{unmasked}|} \quad (8.3)$$

are the same three used in the incoherent imaging system as discussed in section 7.2. All three of these sharpness metrics use information obtained from the image captured by the image plane camera.

When imaging with a coherent system the Fourier transforming property of a single lens produces a Fourier plane located before the image plane. The Fourier transform of the object field is performed optically and captured by a camera located at the Fourier plane. From this captured image the sharpness value is calculated using.

$$S_3 = \frac{\iint |\mathcal{F}\{U_i(x, y)\}_{masked}|^2 df_x df_y}{\iint |\mathcal{F}\{U_i(x, y)\}_{unmasked}|^2 df_x df_y} = \frac{\sum |\mathcal{F}\{U_i(x, y)\}_{masked}|^2}{\sum |\mathcal{F}\{U_i(x, y)\}_{unmasked}|^2} \quad (8.4)$$

where the power spectrum is masked digitally, summed, and divided by the sum of the unmasked power spectrum. Since the Fourier transform has been performed optically there is no need to use the fast Fourier transform. To mask the Fourier transform intensity array the center must be located based on the camera position. Once the center pixel is found this location remains constant as long as the camera is stationary since translation of the object introduces a phase change at the Fourier plane, not a translation. This is a result of the shift theorem, equation 5.5. The central pixels about the center within a circle of a radius equal to the mask size are set to zero and saved as a new array. To calculate the sharpness value using  $S_3$  the sum of the masked array is divided by the sum of the unmasked array.

The final sharpness metric also uses the Fourier transforming property of a single lens in a coherent imaging system. The optical path is divided into two paths with a



camera located at each of the two image planes. In one path a physical, opaque mask is centered in the Fourier plane to block out the low spatial frequencies and let the high spatial frequencies pass through to the image plane. The image plane cameras capture both the spatially filtered image and unfiltered image intensity. Then the captured image intensity is summed and the ratio of these two power values produces the sharpness value as represented by the sharpness metric

$$S_4 = \frac{\iint I(x, y)_{\text{spatially filtered}} dx dy}{\iint I(x, y) dx dy} = \frac{\sum I(x, y)_{\text{spatially filtered}}}{\sum I(x, y)}. \quad (8.5)$$

Both the spatially filtered and unfiltered images are captured by the camera and imported into MatLab where they were converted into two arrays of pixel intensities. The sharpness value using metric  $S_4$  is then found by summing the spatially filtered image intensity and dividing it by the sum of the unfiltered intensity.

### 8.3 Optical System Configurations

Since the sharpness metrics have different optical system requirements, the required system configurations will be discussed in this section. Experimental results will be organized based on the optical configuration

The first configuration is referred to as “camera at the image plane.” There are two configurations, the optics table and telescope setup. In the optics table setup the CCD camera is located at the image plane as seen in figures 8.1 and 8.2. This system is similar to the incoherent imaging system, figure 7.1, with the exception that in this system the object is illuminated by a HeNe laser.

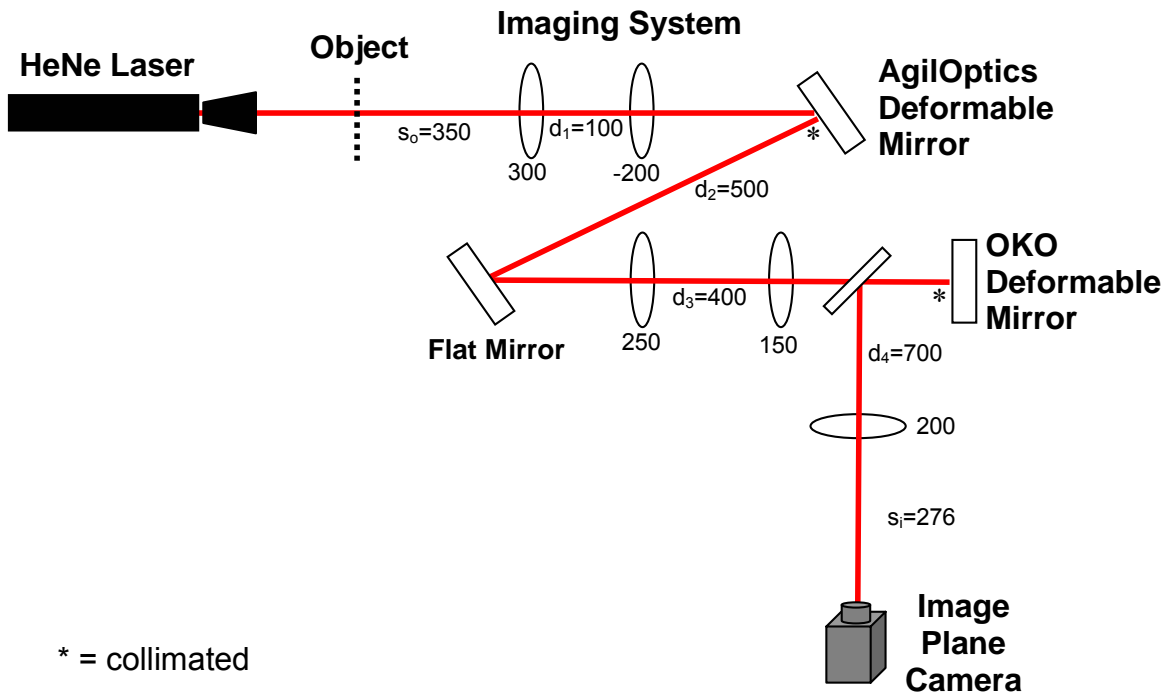


FIGURE 8.1: Experimental schematic with a coherent source and the camera at the image plane. All numbers are in units of millimeters.

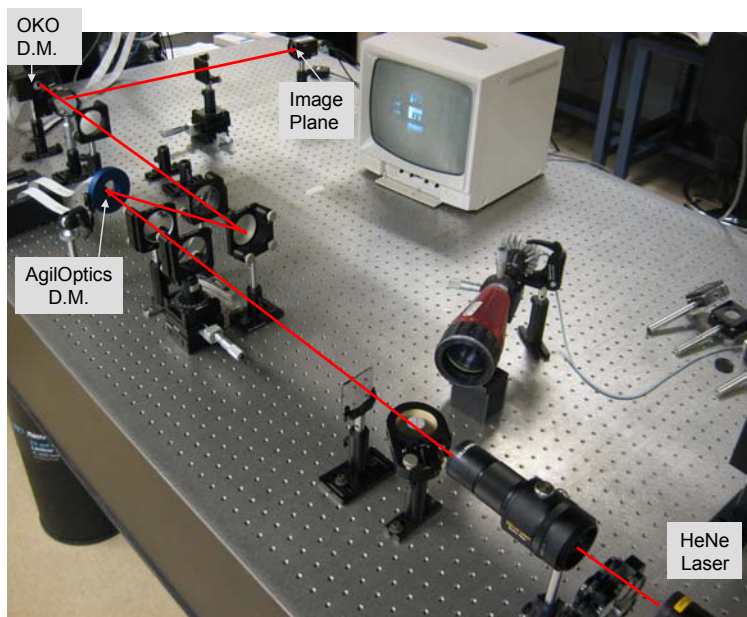


FIGURE 8.2: Optics table experimental setup. Coherent HeNe laser source with the camera located at the image plane.

Like the incoherent system the Fourier transform is performed digitally using MatLab and masking for  $S_2$  is also done digitally by zeroing the central pixel values that fall within a circle with a radius equal to the mask size. Sharpness values  $S_{12}$ ,  $S_1$ , and  $S_2$  are calculated the same way as the incoherent system as described in section 7.2.

The telescope setup seen in figure 7.3 is again used to image coherent point sources. Images captured at the telescope image plane are used with the first three sharpness metrics to calculate the sharpness values using the same methodology as the optics table image plane configuration.

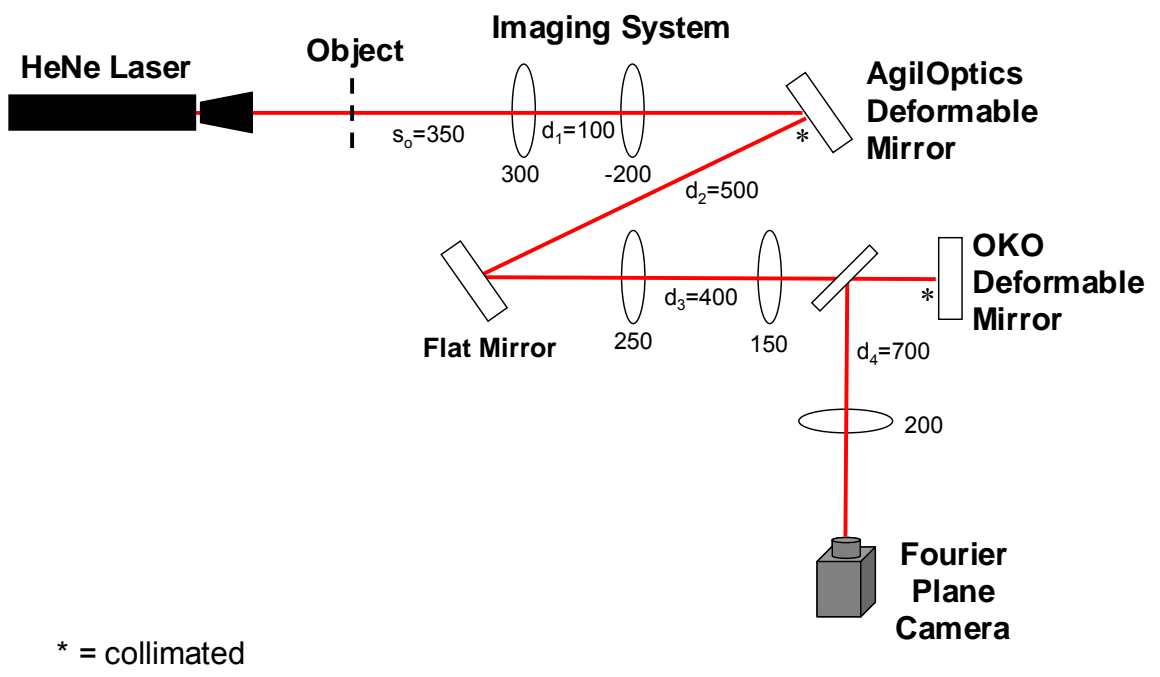


FIGURE 8.3: Experimental schematic with a coherent source and the camera at the Fourier plane. All numbers are in units of millimeters.

For the second configuration, referred to as “camera at the Fourier plane”, the camera is located at the Fourier plane as seen in figures 8.3 and 8.4. The intensity at the Fourier plane is captured by the camera, saved, and imported into MatLab where it is converted to a 640x640 array of Fourier plane intensity values. The sharpness value is then calculated as described in section 8.2.

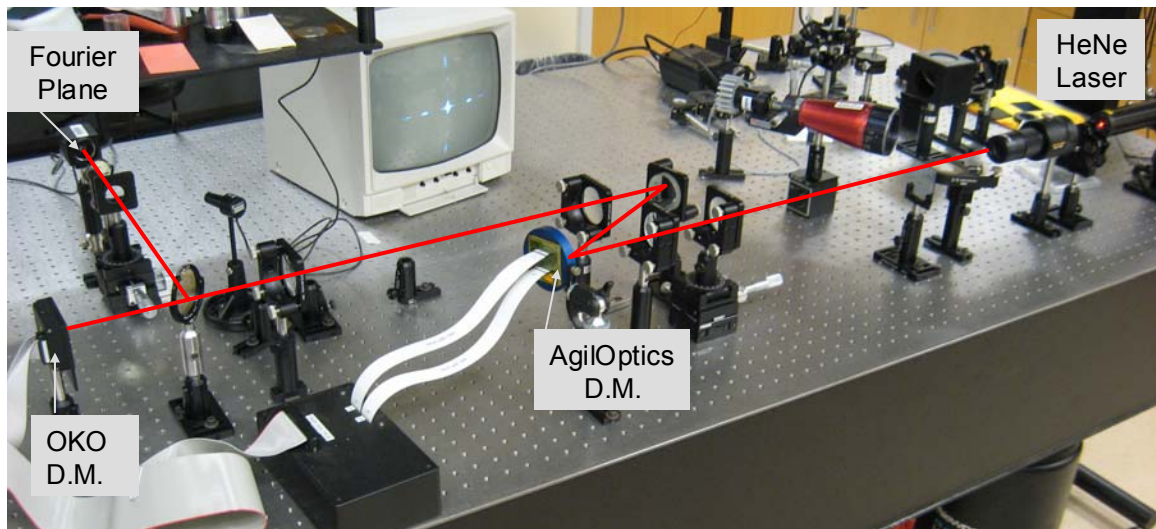


FIGURE 8.4: Optics table experimental setup. Coherent HeNe laser source with the camera located at the Fourier plane.

The third and final configuration called “physical mask at the Fourier plane” again uses the Fourier transforming property of a single lens to do perform spatial filtering. Figure 8.5 shows the optical system requiring the beam to be divided with a beam splitter and a camera placed at each of the two image planes, also seen in figure 8.6. In one optical path a high-pass filter is placed and centered in the Fourier plane blocking the low spatial frequencies and allowing the high spatial frequencies to pass and form an image at the image plane.

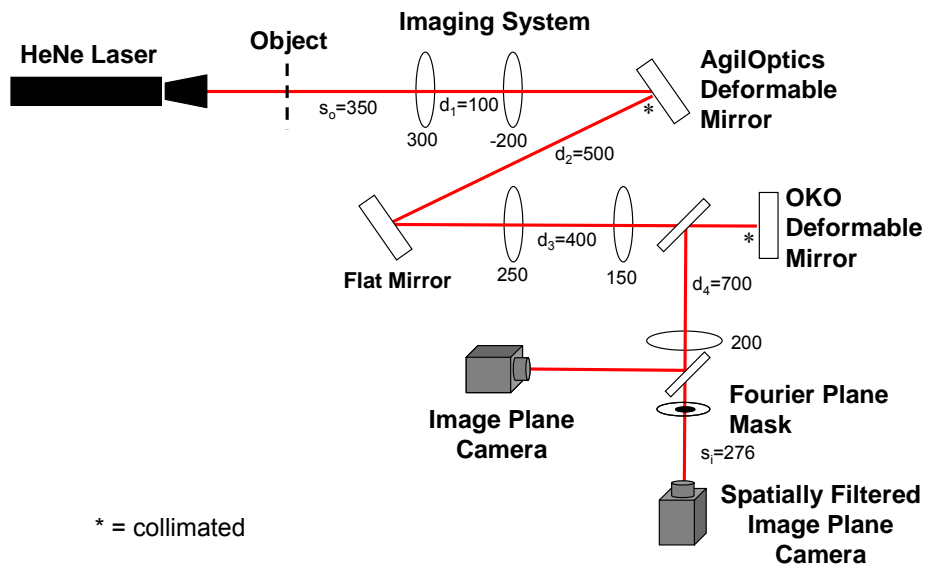


FIGURE 8.5: Experimental schematic with a coherent source and high-pass mask at the Fourier plane. Cameras are located at the image planes to capture the spatially filtered image and the normal image. All numbers are in units of millimeters.

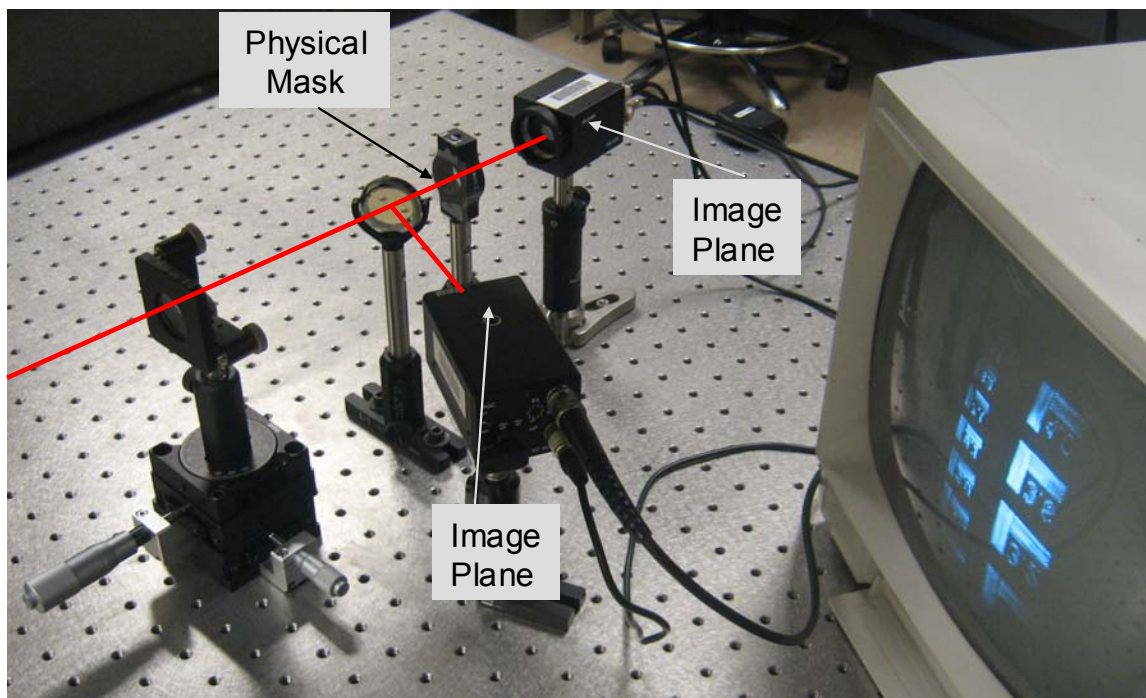


FIGURE 8.6: Optics table setup of the spatially filtering configuration.

The mask consists of a simple overhead transparency with a circle printed on it. For the circle objects where the Fourier transform distribution is spatially smaller, a mask of size 0.13 mm was used and for extended objects with high spatial frequencies a mask of size 1.27 mm was used. Due to the imperfections in the transparencies and the fact that the ink dot was not completely opaque, some low spatial frequencies passed through and some high spatial frequencies were lost

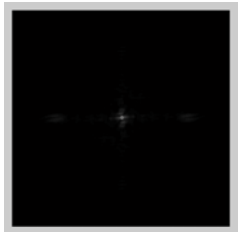
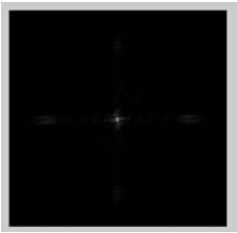
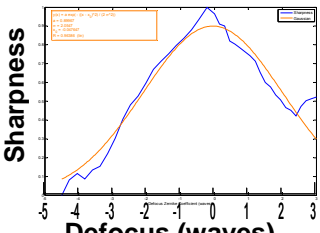
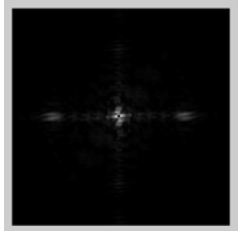
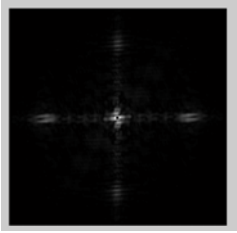
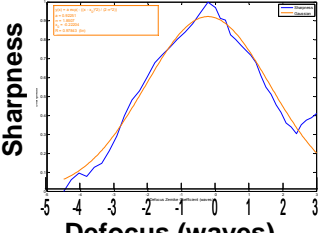
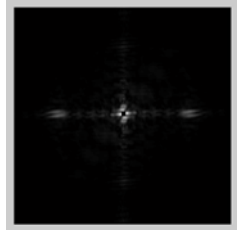
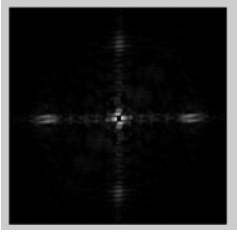
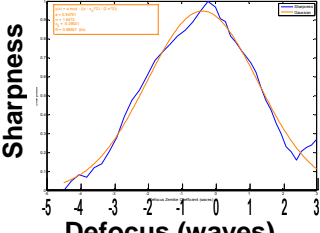
#### 8.4 Sharpness versus Defocus Experimental Results

To investigate the performance of these sharpness metrics the sharpness values were calculated as defocus was added to the system. When plotting the sharpness values as the systems cycles from defocus, through focus, and back out of focus there should be a steep absolute maximum at focus. Sharpness versus defocus plots are obtained in the same way as described in section 7.4. In this section only defocus is considered and higher order aberrations are investigated in the section 8.5. The sharpness versus defocus plots are arranged in subsections based on the optical system configuration used.

##### 8.4.1 Camera at the Image Plane

Using the image plane configuration seen in figures 8.1 and 8.2, the sharpness metrics  $S_{i2}$ ,  $S_1$ , and  $S_2$  were studied first using objects on the optics table illuminated with a HeNe laser. The objects illuminated by the laser were there same objects described in section 7.4.1. Before comparing the three sharpness metrics, the optimal mask size for the  $S_2$  metric needs to be found. Sharpness versus defocus plots for the medium frequency bar chart object were found with varying mask sizes and listed in table 8.1. For these plots the sharpness values were normalized to a range of 0 to 1 and fit to a Gaussian curve to determine the sensitivity by calculating the standard deviation,  $\sigma$ , of

the fitted Gaussian. The Fourier transform of the captured image was performed digitally using fast Fourier transform in MatLab and masked digitally. Masked Fourier transforms at defocus and focus with various mask sizes can be seen in table 8.1 where the plots have been zoomed in to better see the details. For the Fourier transform images it should also be noted that MatLab automatically scales the intensity values when performing a gray plot.

Mask Size (pixels)	Masked Fourier Transform at -2.7 waves of Defocus	Masked Fourier Transform at Focus	Sharpness vs. Defocus with Gaussian Fit
1			 <p>Sharpness vs. Defocus with Gaussian Fit  <math>\sigma = 2.05</math> <math>R = 0.96</math></p>
2			 <p>Sharpness vs. Defocus with Gaussian Fit  <math>\sigma = 1.85</math> <math>R = 0.98</math></p>
3			 <p>Sharpness vs. Defocus with Gaussian Fit  <math>\sigma = 1.65</math> <math>R = 0.99</math></p>

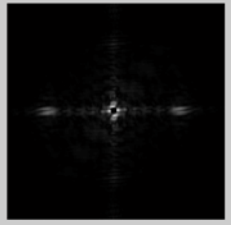
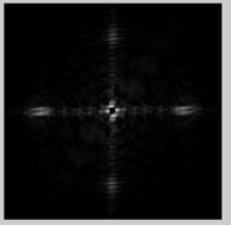
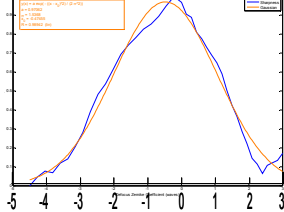
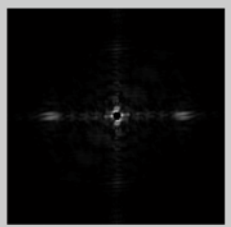
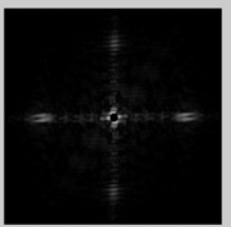
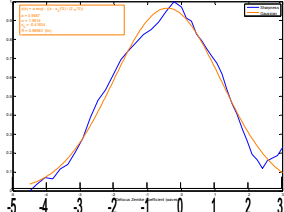
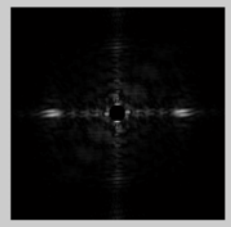
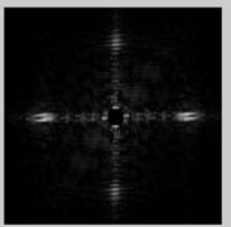
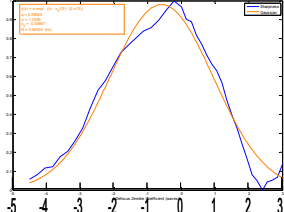
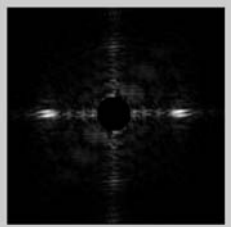
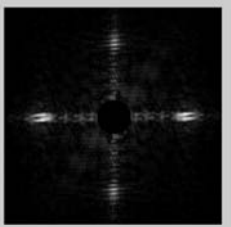
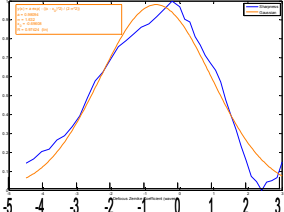
4			 <p>Sharpness</p> <p>Defocus (waves)</p> <p><math>\sigma = 1.54</math> <math>R = 0.99</math></p>
5			 <p>Sharpness</p> <p>Defocus (waves)</p> <p><math>\sigma = 1.59</math> <math>R = 0.99</math></p>
10			 <p>Sharpness</p> <p>Defocus (waves)</p> <p><math>\sigma = 1.54</math> <math>R = 0.98</math></p>
20			 <p>Sharpness</p> <p>Defocus (waves)</p> <p><math>\sigma = 1.63</math> <math>R = 0.97</math></p>

TABLE 8.1:  $S_2$  mask sensitivity for the medium frequency bar chart object illuminated by a coherent source.

It can be seen, especially with mask size 20, that at focus there are more higher spatial frequencies than at defocus and thus there is a maximum  $S_2$  sharpness value at focus. Like the incoherent source, table 7.2, as the mask size increases the standard deviation decreases and thus the sensitivity increases. For all objects it was observed that beyond a mask size of 5 pixels this trend discontinues as the standard deviation slightly



increases. This breakdown in the trend can be attributed to greater noise caused by the speckle effect when using the coherent laser source. Since there is no benefit of increased sensitivity for masks larger than 5 pixels a mask size of 5 pixels was used for all the following  $S_2$  sharpness calculations.

The three sharpness metrics are then compared by finding the sharpness versus defocus plots for all six objects as seen in table 8.2. For comparison the sharpness values have been normalized and fit with a Gaussian to determine the sensitivity. It can be seen that the Fourier-based metrics performed better than  $S_{i2}$  by producing an absolute maximum for all objects where the  $S_{i2}$  failed with the low frequency bar chart and circle object. In general the  $S_2$  metric performed with greater sensitivity than the  $S_1$  metric. For the high frequency bar chart object there are several local maxima due to the increased noise caused by speckle.

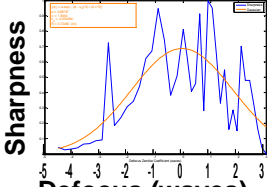
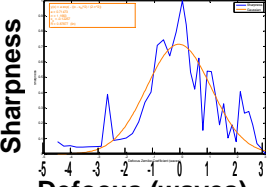
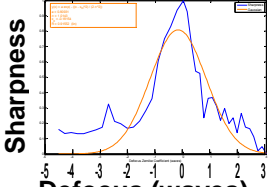
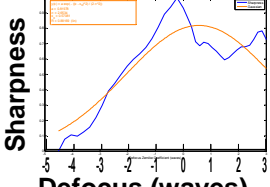
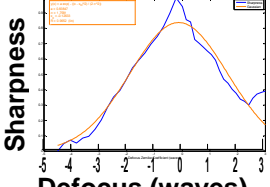
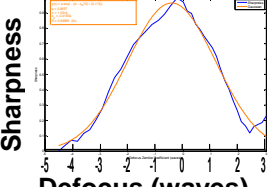
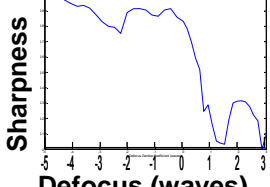
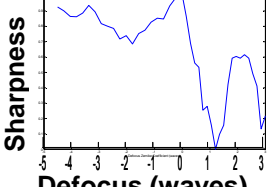
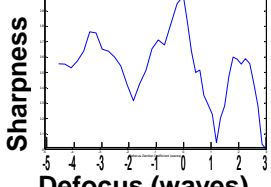
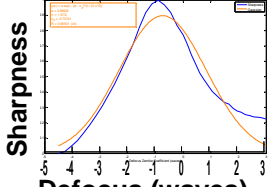
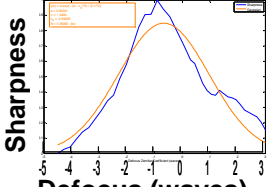
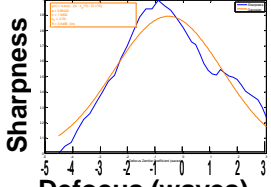
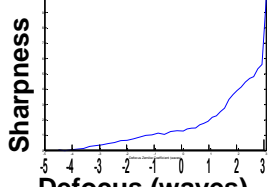
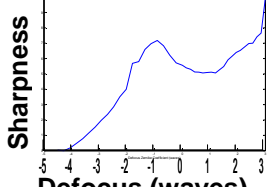
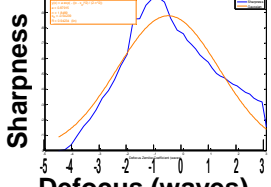
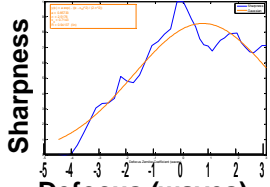
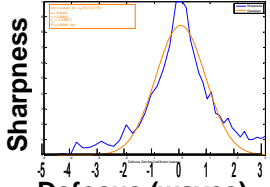
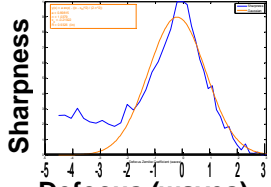
Object	$S_{i2} = \frac{\iint I_i^2(x, y) dx dy}{\left(\iint I_i(x, y) dx dy\right)^2}$	$S_1 = \frac{\iint  \mathcal{F}\{I_i(x, y)\}  df_x df_y}{\iint I_i(x, y) dx dy}$	$S_2 = \frac{\iint \mathcal{F}\{I_i(x, y)\}_{\text{masked}}  df_x df_y}{\iint \mathcal{F}\{I_i(x, y)\}_{\text{unmasked}}  df_x df_y}$
Bar Chart – High Frequency	 <p data-bbox="505 499 716 558"><b>Sharpness</b> <b>Defocus (waves)</b> <math>\sigma = 1.83</math> <math>R = 0.72</math></p>	 <p data-bbox="833 499 1044 558"><b>Sharpness</b> <b>Defocus (waves)</b> <math>\sigma = 1.17</math> <math>R = 0.88</math></p>	 <p data-bbox="1159 499 1370 558"><b>Sharpness</b> <b>Defocus (waves)</b> <math>\sigma = 1.01</math> <math>R = 0.92</math></p>
Bar Chart – Medium Frequency	 <p data-bbox="505 751 716 810"><b>Sharpness</b> <b>Defocus (waves)</b> <math>\sigma = 2.65</math> <math>R = 0.88</math></p>	 <p data-bbox="833 751 1044 810"><b>Sharpness</b> <b>Defocus (waves)</b> <math>\sigma = 1.76</math> <math>R = 0.97</math></p>	 <p data-bbox="1159 751 1370 810"><b>Sharpness</b> <b>Defocus (waves)</b> <math>\sigma = 1.59</math> <math>R = 0.99</math></p>
Bar Chart – Low Frequency	 <p data-bbox="505 1003 716 1062"><b>Sharpness</b> <b>Defocus (waves)</b></p>	 <p data-bbox="833 1003 1044 1062"><b>Sharpness</b> <b>Defocus (waves)</b></p>	 <p data-bbox="1159 1003 1370 1062"><b>Sharpness</b> <b>Defocus (waves)</b></p>
Small Circle Object	 <p data-bbox="505 1255 716 1314"><b>Sharpness</b> <b>Defocus (waves)</b> <math>\sigma = 1.57</math> <math>R = 0.97</math></p>	 <p data-bbox="833 1255 1044 1314"><b>Sharpness</b> <b>Defocus (waves)</b> <math>\sigma = 1.64</math> <math>R = 0.95</math></p>	 <p data-bbox="1159 1255 1370 1314"><b>Sharpness</b> <b>Defocus (waves)</b> <math>\sigma = 1.96</math> <math>R = 0.95</math></p>
Circle Object	 <p data-bbox="505 1507 716 1566"><b>Sharpness</b> <b>Defocus (waves)</b></p>	 <p data-bbox="833 1507 1044 1566"><b>Sharpness</b> <b>Defocus (waves)</b></p>	 <p data-bbox="1159 1507 1370 1566"><b>Sharpness</b> <b>Defocus (waves)</b> <math>\sigma = 1.85</math> <math>R = 0.94</math></p>
Star Pattern	 <p data-bbox="505 1759 716 1812"><b>Sharpness</b> <b>Defocus (waves)</b> <math>\sigma = 2.51</math> <math>R = 0.94</math></p>	 <p data-bbox="833 1759 1044 1812"><b>Sharpness</b> <b>Defocus (waves)</b> <math>\sigma = 0.90</math> <math>R = 0.96</math></p>	 <p data-bbox="1159 1759 1370 1812"><b>Sharpness</b> <b>Defocus (waves)</b> <math>\sigma = 1.04</math> <math>R = 0.93</math></p>

TABLE 8.2: Sharpness vs. defocus plots for a coherent source and optics table setup. Comparison of the three image plane sharpness metrics.  $S_2$  uses a mask size of 5 pixels.

For the telescope setup coherent point sources were created by directing a laser out of the window of an adjacent building toward the laboratory window over a distance of 90 m. Images of the coherent point sources captured by the telescope are seen in table 8.3. Sharpness versus defocus plots for the two point sources using all three metrics were found and placed in table 8.4. Metric  $S_2$  produced an absolute maximum at focus for both point sources where metrics  $S_{i2}$  and  $S_1$  failed.

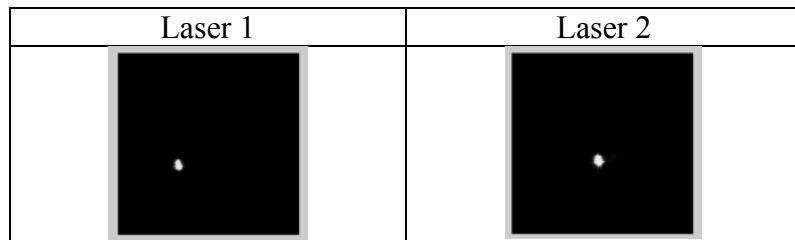


TABLE 8.3: Images of the coherent point sources at a distance of 90 taken with the telescope.

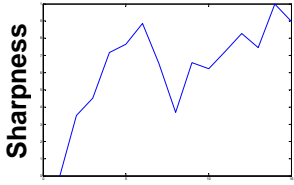
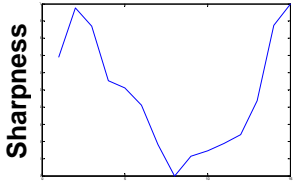
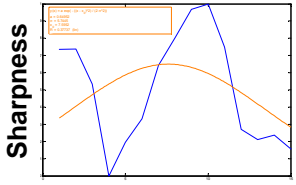
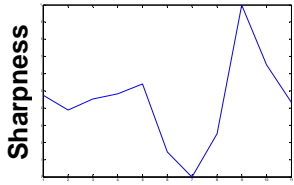
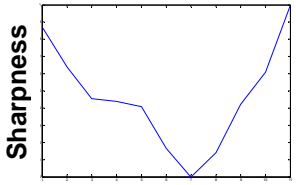
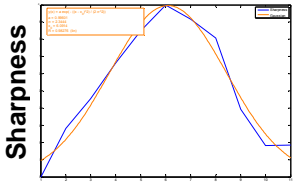
Object	$S_{i2} = \frac{\iint I_i^2(x, y) dx dy}{\left(\iint I_i(x, y) dx dy\right)^2}$	$S_1 = \frac{\iint  \mathcal{F}\{I_i(x, y)\}  df_x df_y}{\iint I_i(x, y) dx dy}$	$S_2 = \frac{\iint \mathcal{F}\{I_i(x, y)\}_{masked}  df_x df_y}{\iint \mathcal{F}\{I_i(x, y)\}_{unmasked}  df_x df_y}$
Laser 1	 Sharpness vs Defocus (image no.)	 Sharpness vs Defocus (image no.)	 Sharpness vs Defocus (image no.) $\sigma = 7.60 \quad R = 0.38$
Laser 2	 Sharpness vs Defocus (image no.)	 Sharpness vs Defocus (image no.)	 Sharpness vs Defocus (image no.) $\sigma = 2.43 \quad R = 0.98$

TABLE 8.4: Sharpness vs. defocus plots for coherent point sources with the telescope setup. Comparison of the three image plane sharpness metrics.  $S_2$  uses a mask size of 5 pixels.

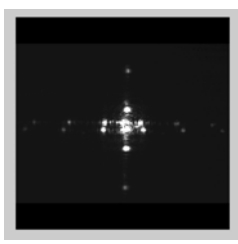
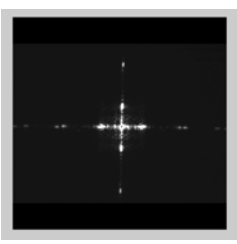
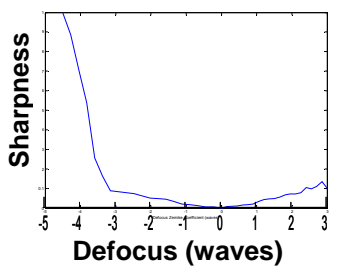
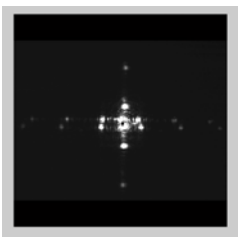
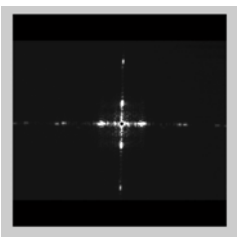
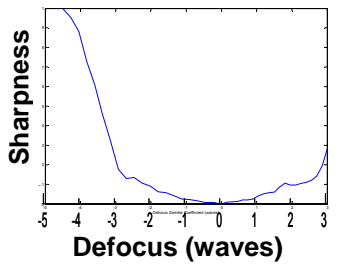
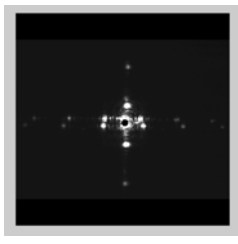
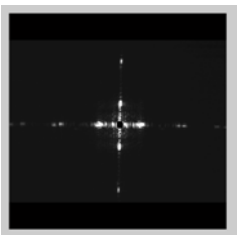
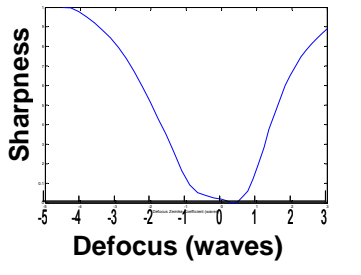
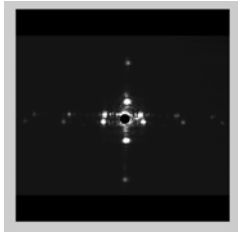
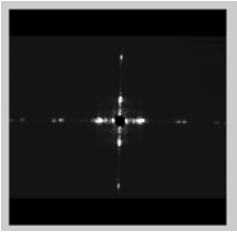
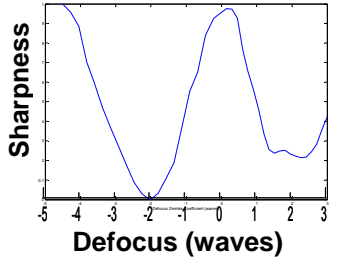
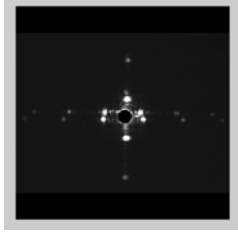
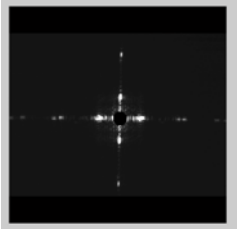
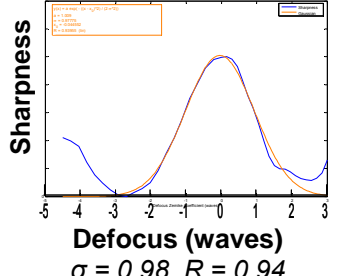
### 8.4.2 Camera at the Fourier Plane

For coherent imaging systems the Fourier transform can be created optically using the transforming property of a single lens. A camera is placed at the Fourier plane the captures  $|\mathcal{F}\{U_i(x, y)\}|^2$ . In this section the captured image refers to the Fourier plane intensity, not the image plane intensity. Thus the sharpness metric,

$$S_3 = \frac{\iint |\mathcal{F}\{U_i(x, y)\}|_{masked}^2 df_x df_y}{\iint |\mathcal{F}\{U_i(x, y)\}|_{unmasked}^2 df_x df_y} = \frac{\sum |\mathcal{F}\{U_i(x, y)\}|_{masked}^2}{\sum |\mathcal{F}\{U_i(x, y)\}|_{unmasked}^2} \quad (8.6)$$

is found by digitally masking the captured image, summing the remaining intensity, and dividing by the sum of the original, unmasked image as described in section 8.2

To find the appropriate digital mask size the sharpness versus defocus plots for the high frequency bar chart object with varying mask sizes were found and placed in table 8.5. The plots were normalized and fitted with a Gaussian to compare sensitivity. Table 8.5 also shows the captured Fourier plane distributions at defocus and focus with the corresponding mask size.

Mask Size (pixels)	Masked Fourier Transform at -2.7 waves of Defocus	Masked Fourier Transform at Focus	Sharpness vs. Defocus with Gaussian Fit
2			 Sharpness vs. Defocus (waves)
5			 Sharpness vs. Defocus (waves)
10			 Sharpness vs. Defocus (waves)
15			 Sharpness vs. Defocus (waves)
20			 Sharpness vs. Defocus (waves) $\sigma = 0.98$ $R = 0.94$

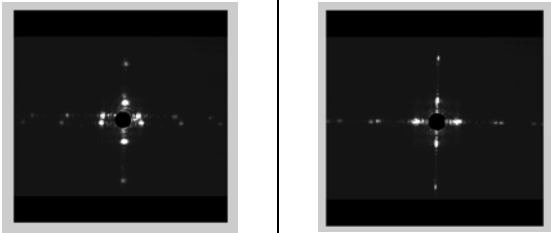
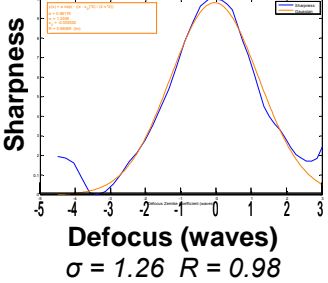

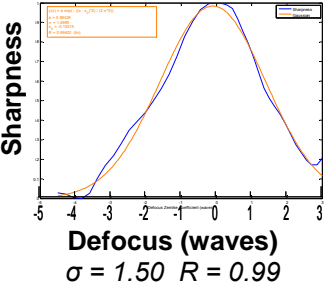
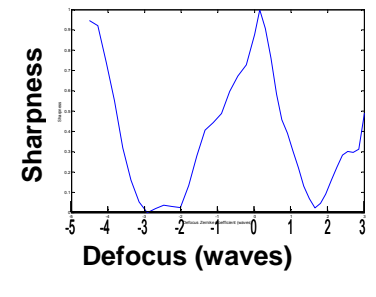
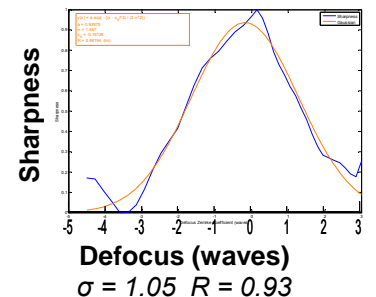
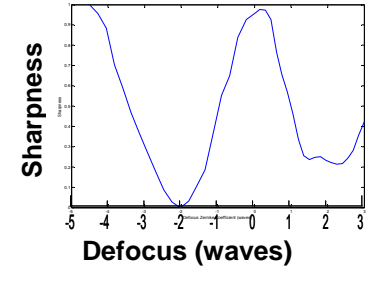
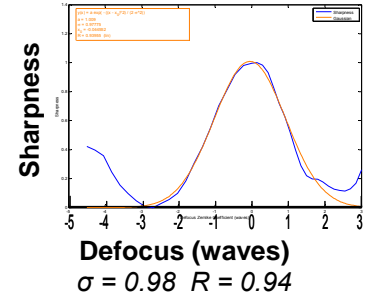
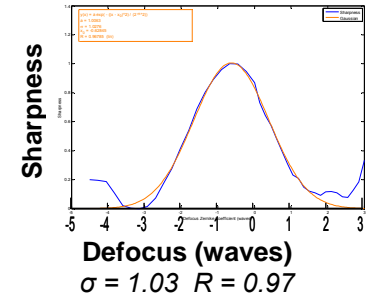
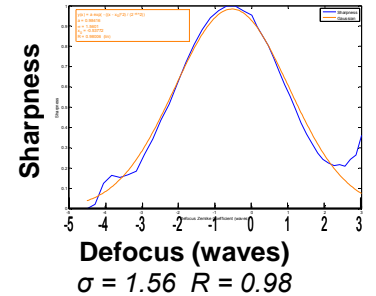
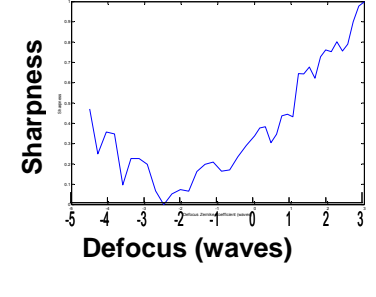
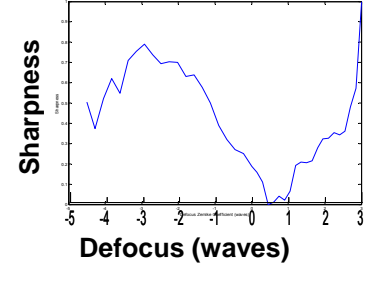
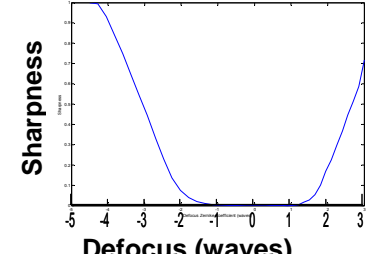
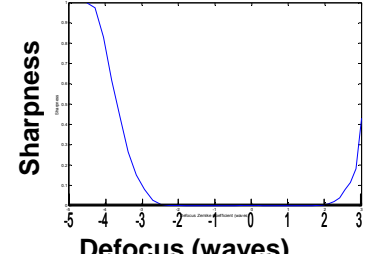
25		
30		

TABLE 8:5:  $S_3$  mask sensitivity for the medium frequency bar chart object illuminated by a coherent source.

It can be seen that an absolute maximum does not appear until the mask size reaches 20 pixels because the central dc term needs to be masked out in order to see the relative increase of high spatial frequencies at focus. Once the mask size is large enough to achieve an absolute maximum, as the mask size increases the standard deviation increases and the sensitivity decreases.

To continue the study the affect of mask size on sensitivity, the sharpness versus defocus plots for all six objects on the optics table were found using mask sizes of 15 and 20 pixels. These plots are found in table 8.6 where the plots have been normalized and fitted with a Gaussian where there is an absolute maximum.

Object	$S_3 = \frac{\iint  \mathcal{F}\{U_i(x,y)\} _{masked}^2 df_x df_y}{\iint  \mathcal{F}\{U_i(x,y)\} _{unmasked}^2 df_x df_y}$ Mask Size = 15 pixels	$S_3 = \frac{\iint  \mathcal{F}\{U_i(x,y)\} _{masked}^2 df_x df_y}{\iint  \mathcal{F}\{U_i(x,y)\} _{unmasked}^2 df_x df_y}$ Mask Size = 20 pixels
Bar Chart - High Frequency		
Bar Chart - Medium Frequency		
Bar Chart - Low Frequency		
Small Circle Object		
Circle Object		

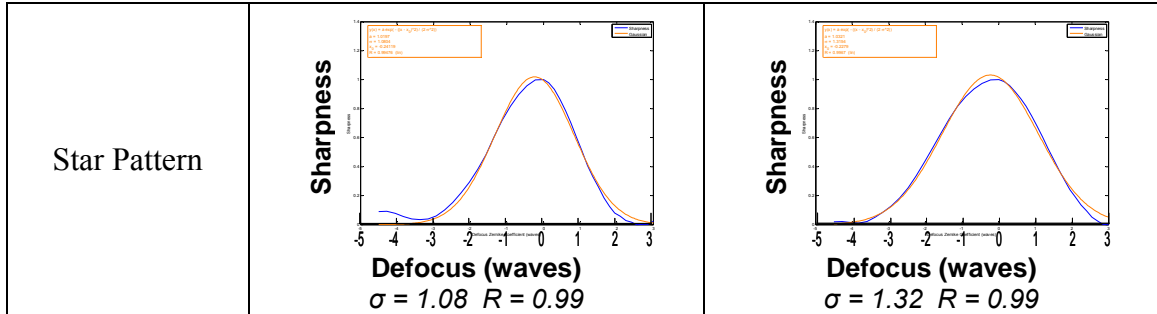


TABLE 8.6: Sharpness vs. defocus plots for a coherent source and optics table setup. Use of the  $S_3$  sharpness metric with mask sizes of 15 and 20 pixels.

The sharpness metric  $S_3$  performs well for the extended bar chart and star pattern objects but fails with the circle objects. Even with smaller mask sizes no maximum was ever observed for the circle objects. For the circle objects the Fourier transform plane distribution is an airy pattern with few high spatial frequencies. At focus the Fourier transform distribution of the circle is the smallest spatially and therefore there is a minimum because more intensity is masked out for the smaller distribution. For extended objects when the dc term is masked out, only the increase of the high spatial frequencies is observed causing a maximum at focus.

It should be noted that the focus location of these plots locates when the camera is at the true Fourier plane. In order for this location to correspond to focus of the image plane camera the system must be calibrated such that the Fourier plane camera at its focus corresponds with the image plane camera at focus. This calibration can be done by using one of the image plane metrics in section 8.4.1 to find the proper image plane camera location and then metric  $S_3$  can be used to find the true Fourier plane to place the Fourier plane camera. Once this is calibrated then the sharpness measured at the Fourier plane with  $S_3$  will correspond to the sharpness value of the image plane.



### 8.4.3 Physical mask at the Fourier plane

Digitally performing the Fourier transform and masking takes additional computing time. To reduce the computation time the Fourier transform can be performed optically with a coherent imaging system and the masking can be done physically. To perform spatial filtering a physical mask was placed at the Fourier plane of one of the optical paths with a camera capturing the spatially filtered image and another camera, located at the image plane of the other divided optical path, captured the unfiltered image. Taking the ratio of the spatially filtered image power to the unfiltered image power produces the sharpness value,  $S_4$ . An example of the spatially filtered images taken at focus and defocus can be seen in figure 8.7.

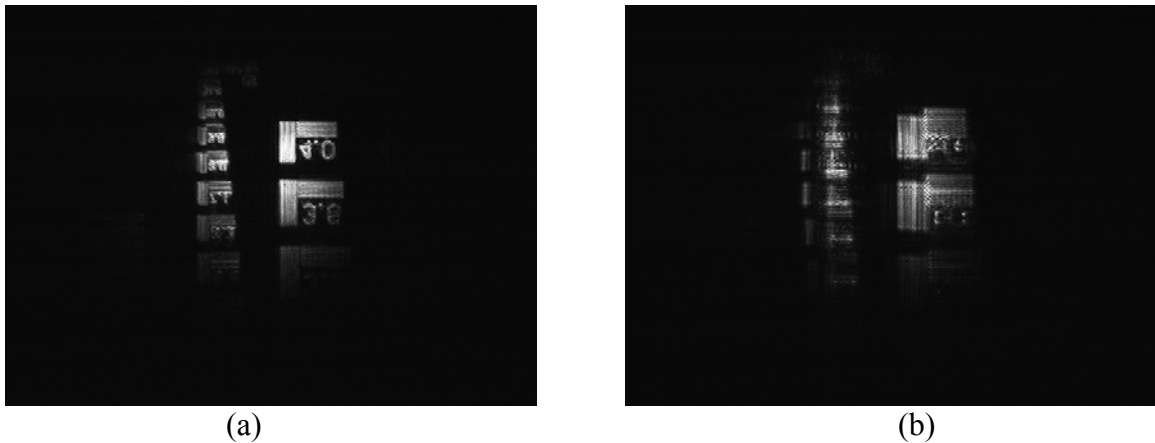
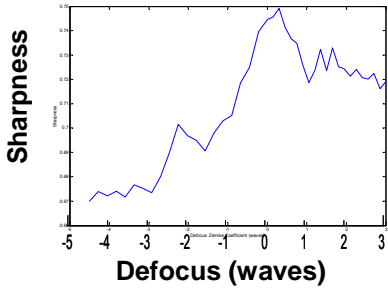
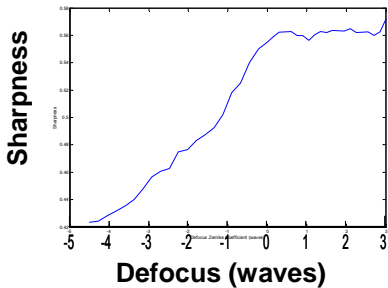


FIGURE 8.7: Image plane captured images of the spatially filtered high frequency bar chart object at (a) focus and (b) defocus.

The sharpness versus defocus plots were created for all six optics table objects and placed in table 8.7. It can be seen that an absolute maximum was reached for the high frequency bar chart and the star pattern, a local maximum was achieved for the medium and low frequency bar charts, and no maximum for the circle objects. For the

circle objects the Fourier plane distribution is an airy pattern with very little high spatial frequencies so when the DC term is masked out there is little intensity in the high spatial frequencies for comparison. As the OKO DM mirror applies defocus curvature is applied to the wavefront causing the location of the Fourier plane to move. As the Fourier transform location moves the distribution at the mask increased in spatial size causing the relative size of the mask to the Fourier plane decrease and the light passing by the mask for the circle objects to increase. This is most noticeable in the linear behavior of the small circle object. This method was successful for objects with high spatial frequencies where the DC term is masked and the remaining high spatial frequencies pass by the mask for comparison as defocus is added.

Object	$S_4 = \frac{\iint I(x, y)_{\text{spatially filtered}} dx dy}{\iint I(x, y) dx dy}$
Bar Chart - High Frequency	 <p>Sharpness</p> <p>Defocus (waves)</p>
Bar Chart - Medium Frequency	 <p>Sharpness</p> <p>Defocus (waves)</p>

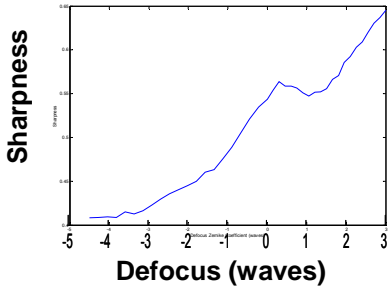
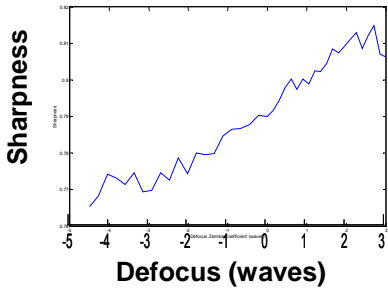
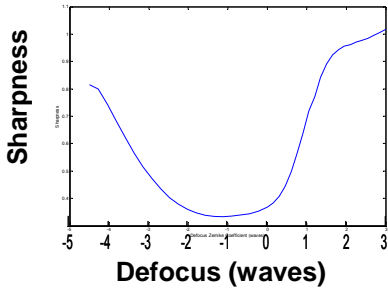
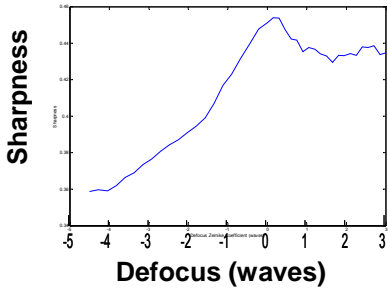
Bar Chart - Low Frequency	
Small Circle Object	
Circle Object	
Star Pattern	

TABLE 8.7: Sharpness vs. defocus plots for a coherent source and optics table setup using the  $S_4$  sharpness metric.

#### 8.4.4 Summary

The image plane sharpness metrics,  $S_{i2}$ ,  $S_1$ , and  $S_2$ , were successful for most objects. In the case of the circle object, the Fourier-based metrics  $S_1$  and  $S_2$  produced a

local maximum at focus where the  $S_{i2}$  failed to produce a maximum. Compared to the incoherent source, the sharpness versus defocus plots with the coherent source contained more noise due to the speckle effect of the laser. As the mask size of  $S_2$  increased so did the sensitivity up to a point where this trend broke down.

The  $S_3$  metric with the camera at the Fourier plane was successful for the extended bar chart and star pattern objects but not for the circular objects. Mask size for the  $S_3$  metric had to be large enough to mask out the DC term and beyond this the sensitivity decreased as the mask size increased. Proper use of this metric requires calibration such that the camera at the true Fourier plane corresponds to the imaging camera at the true image plane.

The final metric,  $S_4$ , involved spatial filtering by placing a physical mask at the Fourier plane of one of the divided optical paths. This metric failed for the circular objects but was successful for extended objects working better for objects with higher spatial frequencies. When defocus is added the Fourier plane location moves and thus the mask size relative to the Fourier transform changes causing the failure with circular objects.

Computing times varied with the sharpness depending on whether the Fourier transform was performed digitally or optically and if masking was done digitally or physically. The computing times to calculate the sharpness of a single captured image for all sharpness metrics are listed in table 8.8.  $S_4$  was the fastest since the Fourier transform was done optically and the masking done physically where  $S_2$  was the slowest as both were done digitally.

	$S_{i2}$	$S_1$	$S_2$	$S_3$	$S_4$
Computing Time	4.04 s	4.40 s	4.56 s	4.12 s	1.0 s

TABLE 8.8: Computing time of the sharpness metrics.

## 8.5 Sharpness versus higher order aberrations

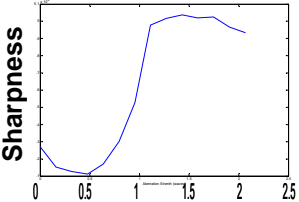
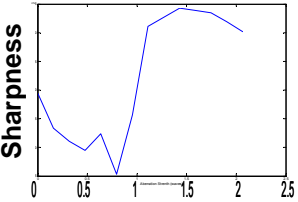
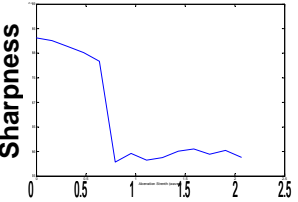
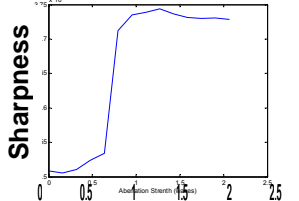
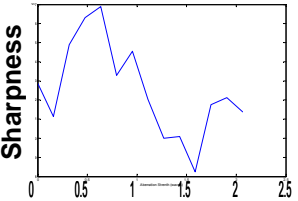
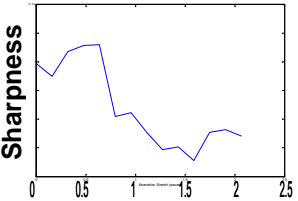
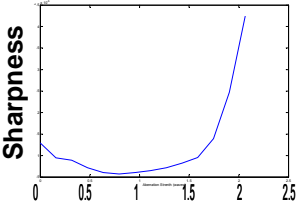
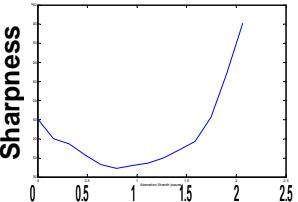
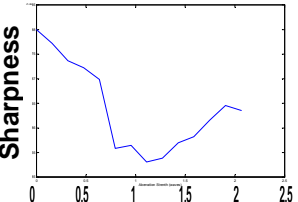
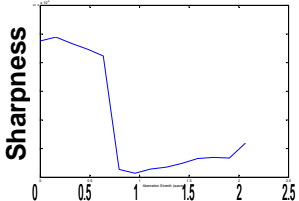
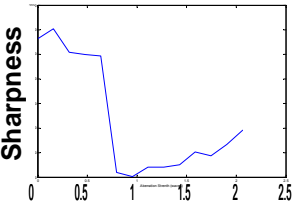
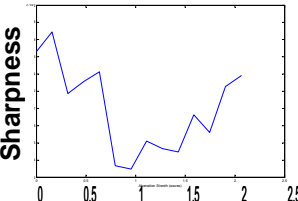
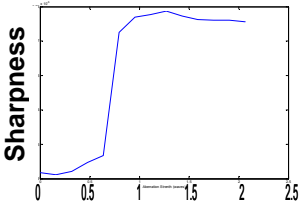
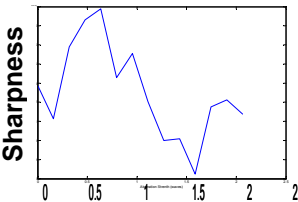
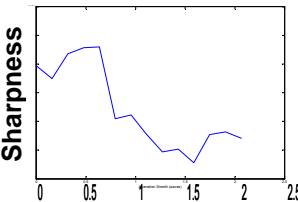
After studying the performance of the sharpness metrics with defocus, higher order aberrations were applied and the sharpness values were measured. Astigmatism, coma, and spherical aberrations were the higher aberrations applied with the OKO deformable mirror using the same method as for the incoherent imaging system described in section 7.5. All five sharpness metrics were used to measure and plot the sharpness value versus aberration strength. Defocus was applied over a range from negative to positive defocus causing the sharpness maximum to appear toward the center of the plot at zero waves of defocus. For the higher order aberrations the aberration strength increased from zero, therefore the sharpness maximum should be located on the left side of the plot where the aberration strength is zero. Results in this section are divided based on the optical system configuration used as in section 8.4.

### 8.5.1 Camera at the Image Plane

The three image plane sharpness metrics,  $S_{i2}$ ,  $S_1$ , and  $S_2$ , were used to calculate the sharpness value versus aberration strength of astigmatism, coma, and spherical aberration. For the  $S_2$  metric, a mask size of 20 pixels was used in the following plots.

Sharpness versus aberration strength plots for astigmatism, coma, and spherical aberration can be seen in figures 8.9, 8.10, and 8.11 respectively. For astigmatism the  $S_2$  outperformed the other two metrics by producing an absolute maximum at zero waves for all objects where the other two metrics failed for most objects. Again the  $S_2$  metric was

successful for all objects when coma was applied except for the low frequency bar chart object where there was a local maximum. Finally for spherical aberration both Fourier-based metrics,  $S_1$  and  $S_2$ , failed for the medium and low frequency bar object but were more successful and sensitive than the  $S_{i2}$  metric for all other objects.

Object	$S_{i2} = \frac{\iint I_i^2(x, y) dx dy}{\left(\iint I_i(x, y) dx dy\right)^2}$	$S_1 = \frac{\iint  \mathcal{F}\{I_i(x, y)\}  df_x df_y}{\iint I_i(x, y) dx dy}$	$S_2 = \frac{\iint \mathcal{F}\{I_i(x, y)\}_{masked}   df_x df_y}{\iint \mathcal{F}\{I_i(x, y)\}_{unmasked}   df_x df_y}$
Bar Chart - High Frequency	 <p>Astigmatism (waves)</p>	 <p>Astigmatism (waves)</p>	 <p>Astigmatism (waves)</p>
Bar Chart - Medium Frequency	 <p>Astigmatism (waves)</p>	 <p>Astigmatism (waves)</p>	 <p>Astigmatism (waves)</p>
Bar Chart - Low Frequency	 <p>Astigmatism (waves)</p>	 <p>Astigmatism (waves)</p>	 <p>Astigmatism (waves)</p>
Small Circle Object	 <p>Astigmatism (waves)</p>	 <p>Astigmatism (waves)</p>	 <p>Astigmatism (waves)</p>
Circle Object	 <p>Astigmatism (waves)</p>	 <p>Astigmatism (waves)</p>	 <p>Astigmatism (waves)</p>

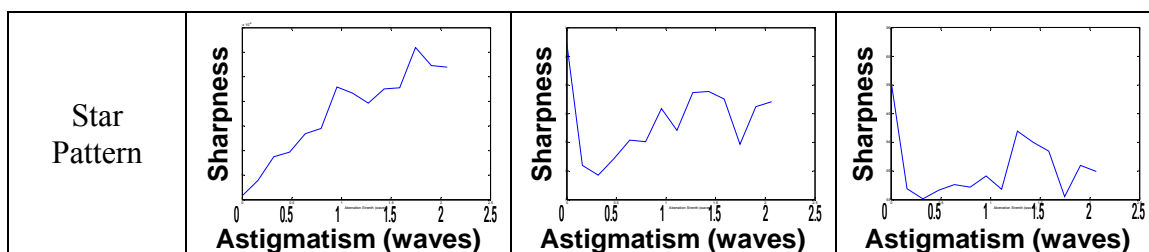
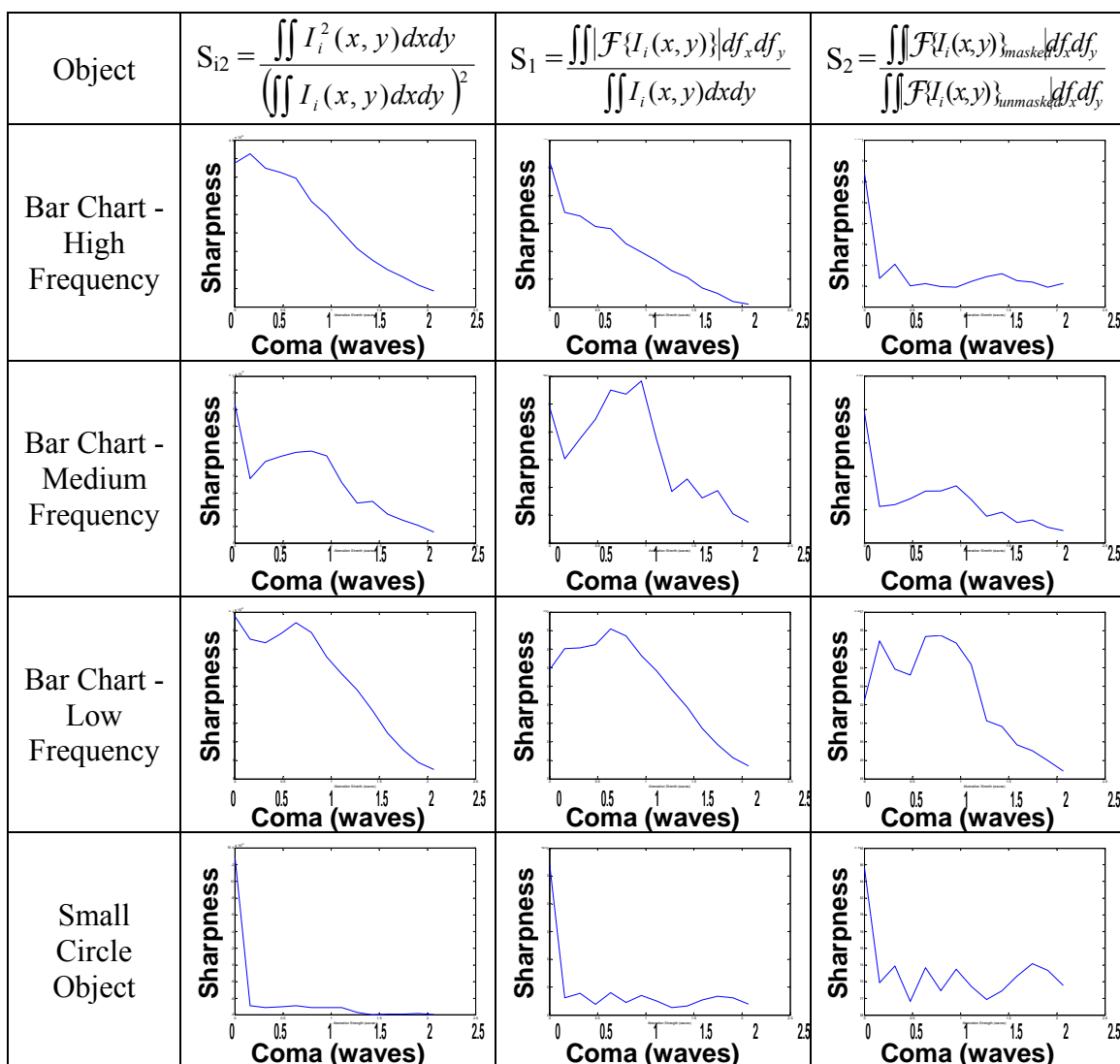


TABLE 8.9: Sharpness vs. astigmatism plots for a coherent source and optics table setup. Comparison of the three image plane sharpness metrics.  $S_2$  uses a mask size of 20 pixels.



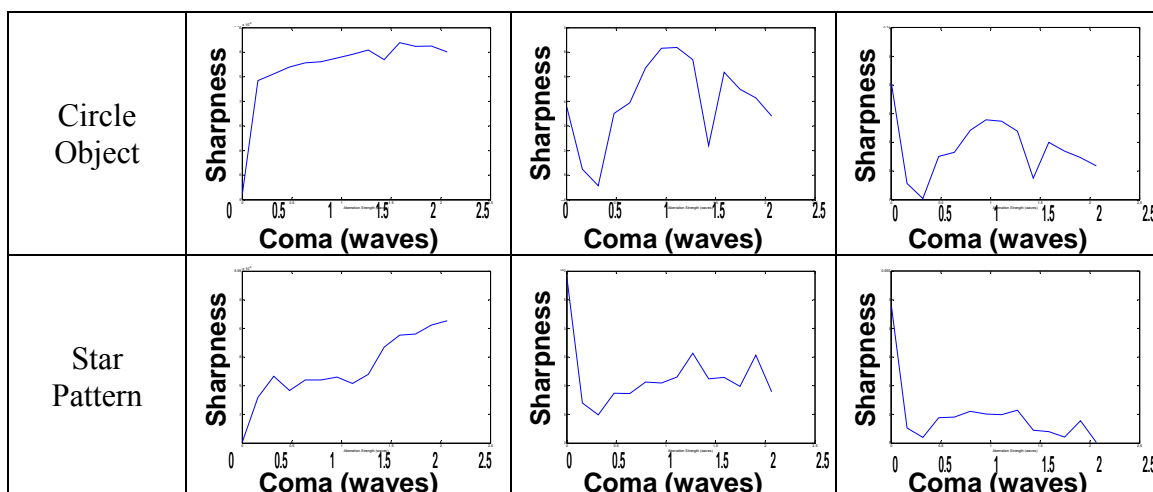
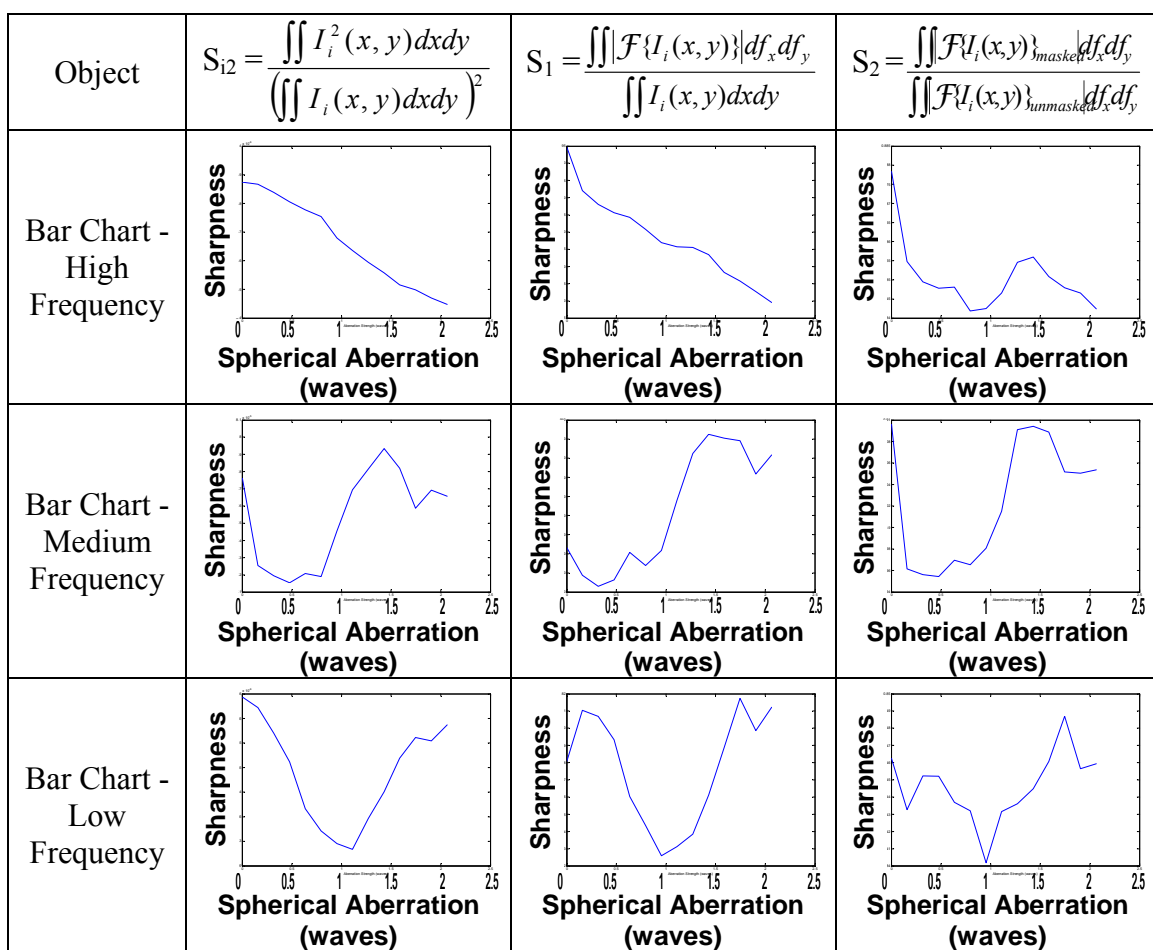


TABLE 8.10: Sharpness vs. coma plots for a coherent source and optics table setup. Comparison of the three image plane sharpness metrics.  $S_2$  uses a mask size of 20 pixels.





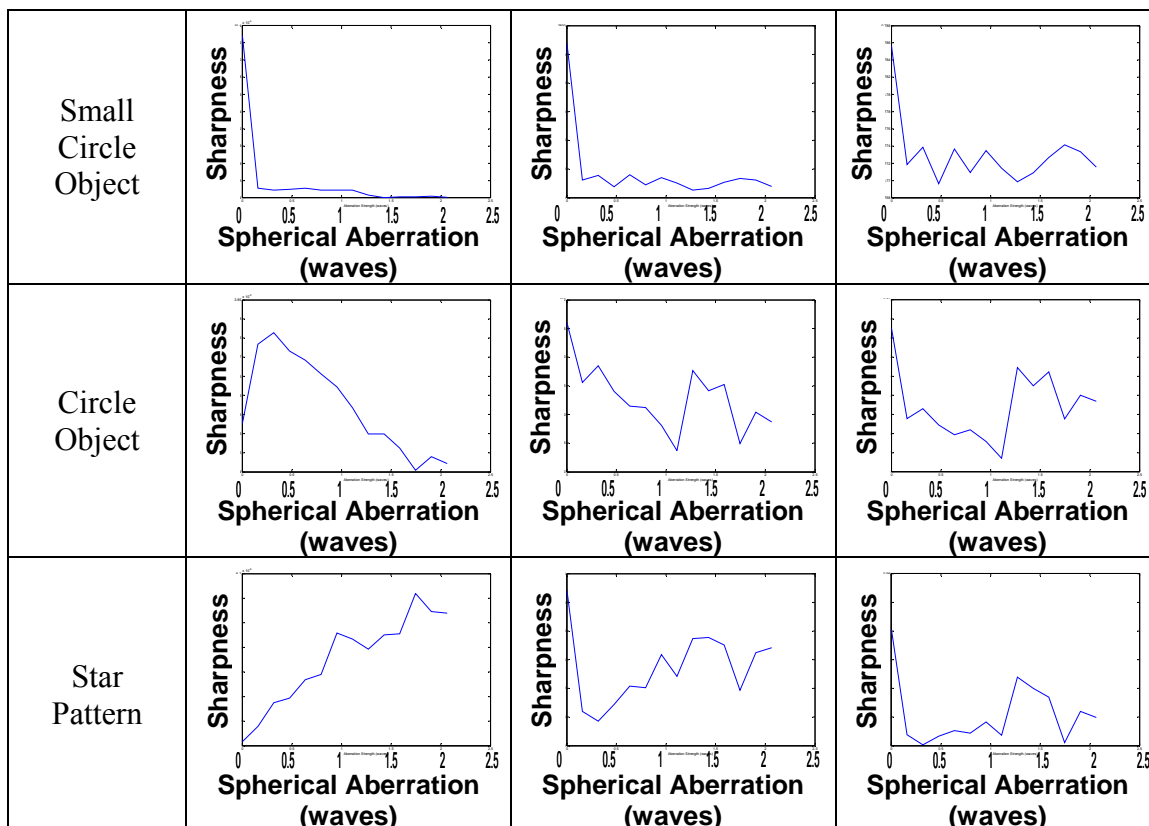


TABLE 8.11: Sharpness vs. spherical aberration plots for a coherent source and optics table setup. Comparison of the three image plane sharpness metrics.  $S_2$  uses a mask size of 20 pixels.

### 8.5.2 Camera at the Fourier Plane

The imaging camera was placed at the Fourier plane and the sharpness metric  $S_3$  was used to measure the sharpness value. Masking was done digitally and a mask size of 20 pixels was used for all objects except the circle object where a mask size of 10 pixels was used. Sharpness versus aberration strength plots for astigmatism, coma, and spherical aberration can be seen in table 8.12. Adding higher order aberrations like astigmatism and coma causes the optical axis to move throughout the optical system causing the Fourier plane distribution to translate relative to the stationary camera. Spherical aberration, like defocus, also causes the location of the Fourier plane to move

along the optical axis causing the distribution captured by the Fourier plane camera to change in size. Since the mask is digital and fixed the portion of the Fourier distribution that is masked varies as these aberrations increase causing the distribution to translate and change size. This is most noticeable with the circle where there is a minimum at zero waves of aberration because the mask is centered according to the distribution at zero wavefront error and as aberrations increase and the Fourier distribution translates, more intensity passes by the mask increasing the sharpness value. For the extended objects if the mask is large enough to mask out the DC term then just the high spatial frequencies pass. Since the most of the intensity is located in the DC term then the motion of the Fourier distribution is no longer a factor if the mask is large enough. This can be seen in the results of the extended bar chart and start pattern objects where the sharpness metric  $S_3$  was successful in producing either a local or absolute maximum at zero waves of aberration.

Object	Astigmatism	Coma	Spherical Aberration
Bar Chart - High Frequency	<p>Sharpness vs Astigmatism (waves)</p>	<p>Sharpness vs Coma (waves)</p>	<p>Sharpness vs Spherical Aberration (waves)</p>
Bar Chart - Medium Frequency	<p>Sharpness vs Astigmatism (waves)</p>	<p>Sharpness vs Coma (waves)</p>	<p>Sharpness vs Spherical Aberration (waves)</p>

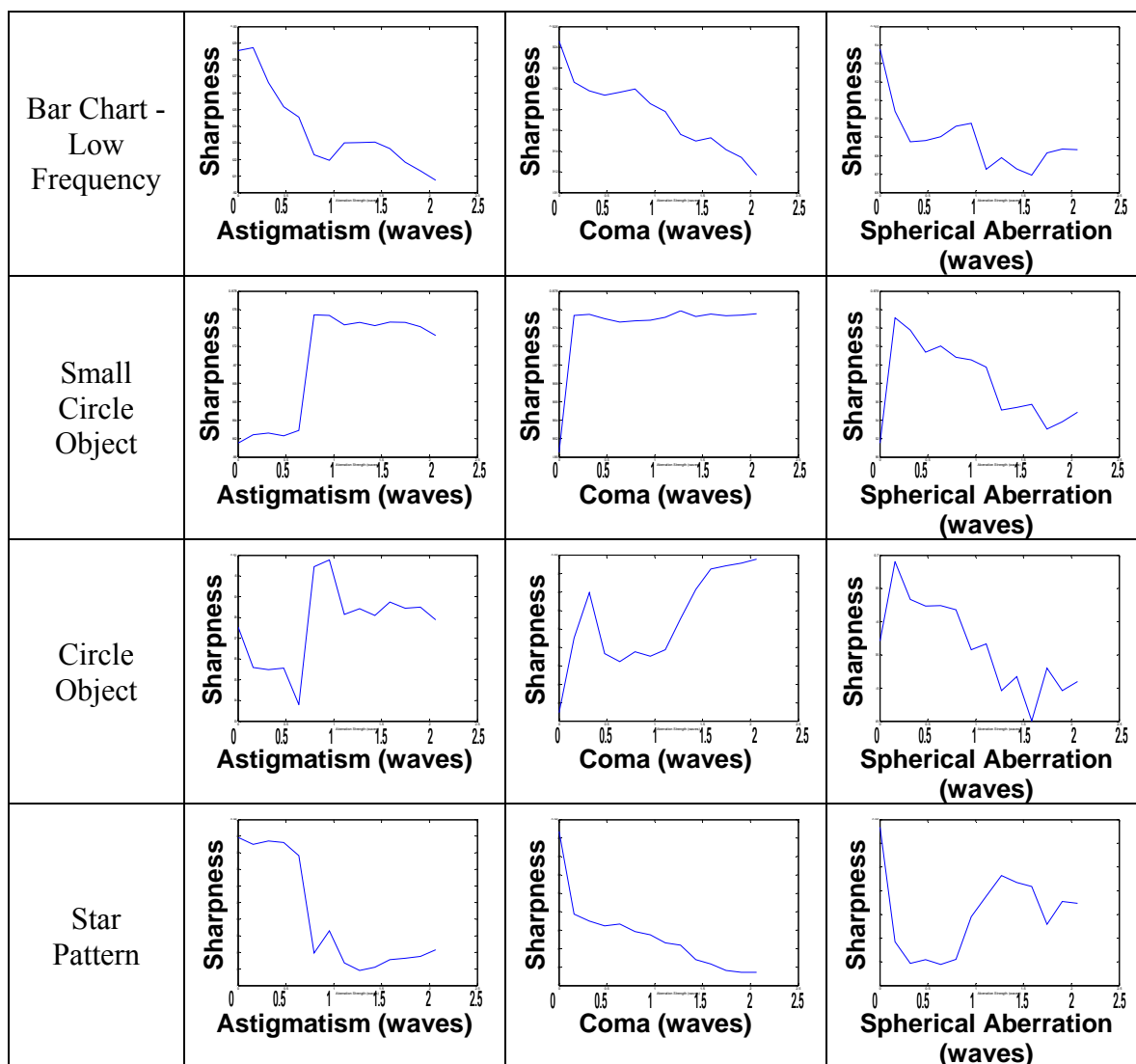
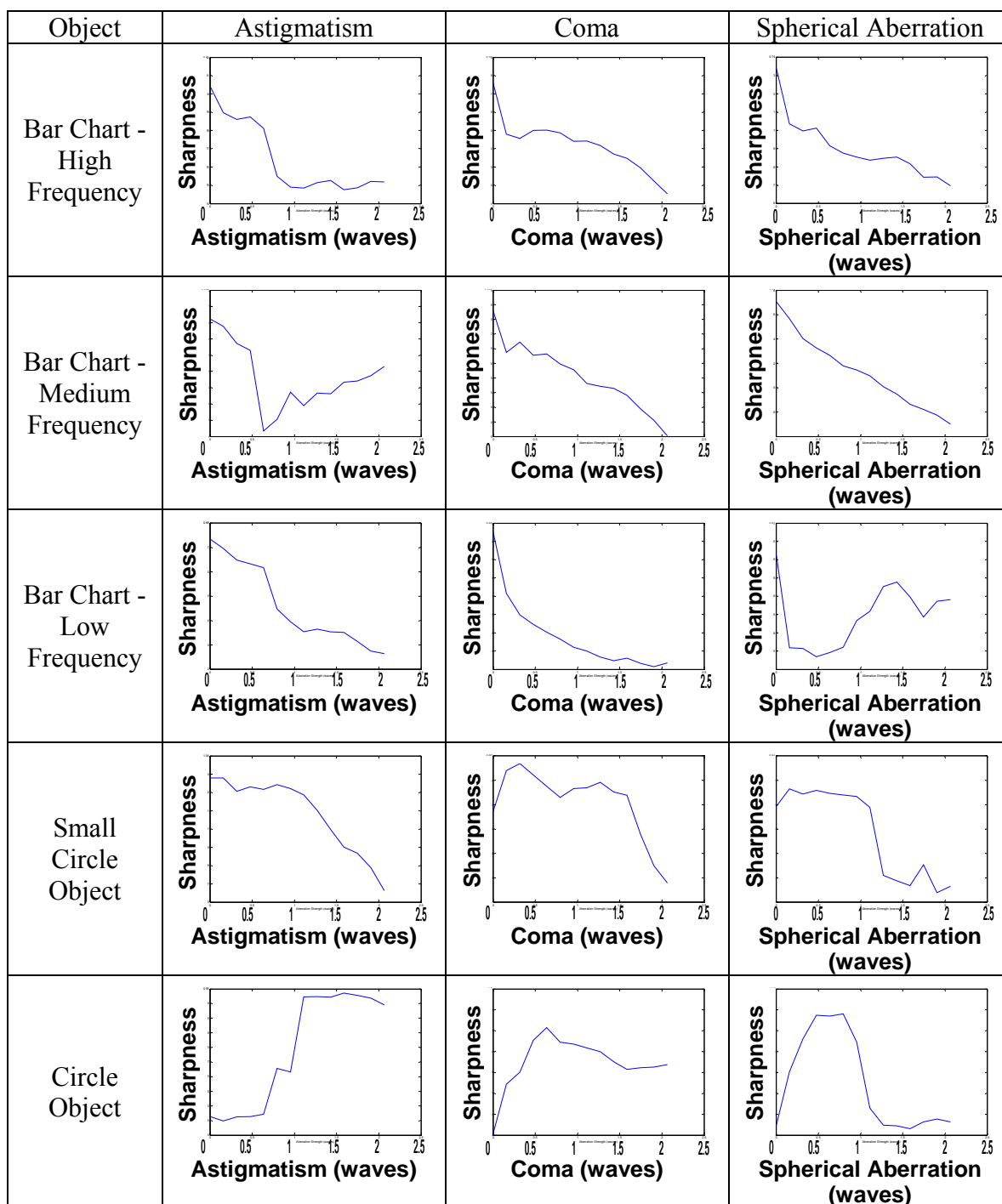


TABLE 8.12: Sharpness vs. aberration strength plots for a coherent source and optics table setup with all higher order aberrations. Use of sharpness metric  $S_2$  with a mask size of 20 pixels (10 pixels for circle object).

### 8.5.3 Physical mask at the Fourier plane

Finally, the higher-order aberrations were applied to the spatial filtering configuration to measure the sharpness using metric  $S_4$ . As with the  $S_3$  metric, the circle objects failed due to the motion of the optical axis as higher order aberrations were added causing the Fourier distribution to translate with respect to the stationary physical mask and different portions to be masked out. Table 8.13 shows the sharpness versus

aberration strength plots for all objects and aberrations. For the extended objects this sharpness metric performed very well since the DC term was masked out causing the decrease in high spatial frequencies to be seen as the aberration strength increased.



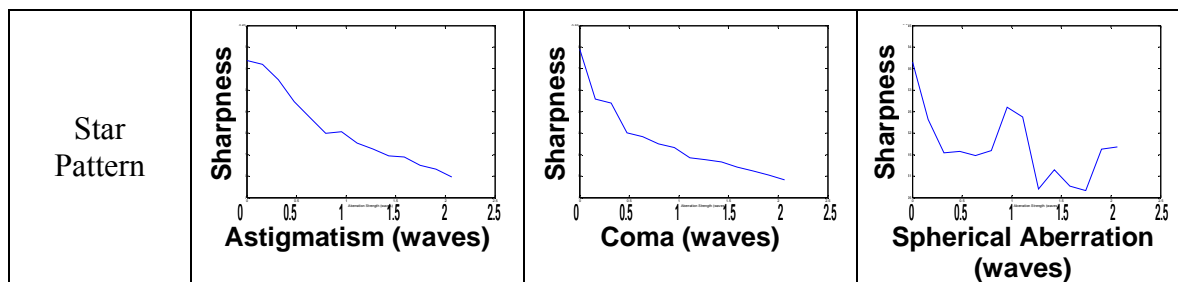


TABLE 8.13: Sharpness vs. aberration strength plots for a coherent source and optics table setup with all higher order aberrations. Sharpness metric  $S_4$  was used.

In summary, for the extended bar chart and star pattern objects, all the sharpness metrics were successful as higher order aberrations were added. There were some exceptions with the  $S_{12}$  and  $S_1$  metrics where there was a local maximum instead of an absolute maximum at zero waves of aberration. For the circle objects the image plane sharpness metrics,  $S_{12}$ ,  $S_1$ , and  $S_2$  were successful but the  $S_3$  and  $S_4$  metrics failed due to the motion of the optical axis causing the Fourier transform distribution to translate as aberrations were added causing the masked portions to change and not give an accurate sharpness value.

## 8.6 Performance in a closed-loop system

The first three image plane metrics with the camera at the image plane were implemented in a preliminary, manual, closed-loop system using the same method described in section 7.6. Using the high frequency bar chart object and the optics table setup the captured images and corresponding sharpness values can be seen in table 8.14. Absolute maxima are indicated with bold text and local maxima are in italics. There was slight disagreement in the OKO DM actuator values for the absolute maximum sharpness values for all three metrics. It appears that  $S_2$  identifies the image that is most visibly in focus.

















 <p> <math>S_{i2} = 8.228 \times 10^{-6}</math>  <math>S_1 = 223.21</math>  <math>S_2 = 0.9712</math>            OKO Actuator = 0         </p>	 <p> <math>S_{i2} = 8.087 \times 10^{-6}</math>  <math>S_1 = 220.95</math>  <math>S_2 = 0.9718</math>            OKO Actuator = .05         </p>	 <p> <math>S_{i2} = 8.245 \times 10^{-6}</math>  <math>S_1 = 222.97</math>  <math>S_2 = 0.9719</math>            OKO Actuator = -.05         </p>	 <p> <math>S_{i2} = 8.349 \times 10^{-6}</math>  <math>S_1 = 226.13</math>  <math>S_2 = 0.9722</math>            OKO Actuator = -.1         </p>
 <p> <math>S_{i2} = 8.384 \times 10^{-6}</math>  <math>S_1 = 226.99</math>  <math>S_2 = 0.9724</math>            OKO Actuator = -.15         </p>	 <p> <math>S_{i2} = 8.342 \times 10^{-6}</math>  <math>S_1 = 236.68</math>  <math>S_2 = 0.9742</math>            OKO Actuator = -.2         </p>	 <p> <math>S_{i2} = 8.314 \times 10^{-6}</math>  <math>S_1 = 246.39</math>  <math>S_2 = 0.9755</math>            OKO Actuator = -.25         </p>	 <p> <math>S_{i2} = 8.185 \times 10^{-6}</math>  <math>S_1 = 254.76</math>  <math>S_2 = 0.9770</math>            OKO Actuator = -.3         </p>
 <p> <math>S_{i2} = 8.233 \times 10^{-6}</math>  <math>S_1 = 264.51</math>  <math>S_2 = 0.9783</math>            OKO Actuator = -.35         </p>	 <p> <math>S_{i2} = 8.278 \times 10^{-6}</math>  <math>S_1 = 272.03</math>  <math>S_2 = 0.9793</math>            OKO Actuator = -.4         </p>	 <p> <math>S_{i2} = 8.322 \times 10^{-6}</math>  <math>S_1 = 275.00</math>  <math>S_2 = 0.9797</math>            OKO Actuator = -.45         </p>	 <p> <math>S_{i2} = 8.354 \times 10^{-6}</math>  <math>S_1 = 279.95</math>  <math>S_2 = \mathbf{0.9801}</math>            OKO Actuator = -.5         </p>
 <p> <math>S_{i2} = 8.451 \times 10^{-6}</math>  <math>S_1 = \mathbf{280.52}</math>  <math>S_2 = 0.9797</math>            OKO Actuator = -.55         </p>	 <p> <math>S_{i2} = 8.644 \times 10^{-6}</math>  <math>S_1 = 275.15</math>  <math>S_2 = 0.9788</math>            OKO Actuator = -.6         </p>	 <p> <math>S_{i2} = \mathbf{8.737 \times 10^{-6}}</math>  <math>S_1 = 265.98</math>  <math>S_2 = 0.9775</math>            OKO Actuator = -.65         </p>	 <p> <math>S_{i2} = 8.691 \times 10^{-6}</math>  <math>S_1 = 256.59</math>  <math>S_2 = 0.9763</math>            OKO Actuator = -.7         </p>

TABLE 8.14: Closed-loop images of the high frequency object using the image plane sharpness metrics. Mask size of 5 pixels used for  $S_2$ .

The  $S_3$  metric was also implemented in a manual closed loop system where the camera was at the Fourier plane. In table 8.15 the captured images can be seen along with the sharpness values with mask sizes of 15 and 20 pixels. There is agreement in

both mask sizes as to which OKO actuator valued produced an absolute sharpness value and thus indicating when the camera is truly at the Fourier plane.

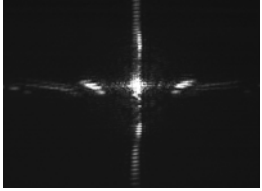
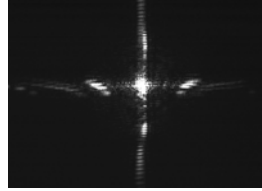
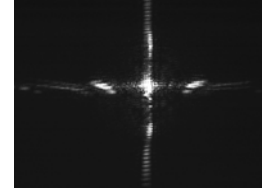
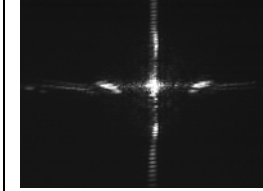
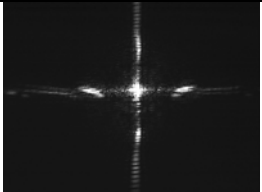
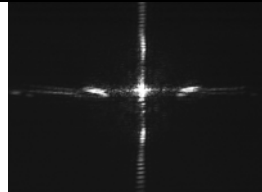
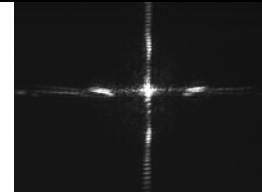
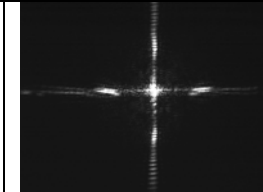
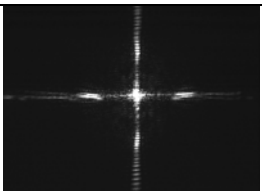
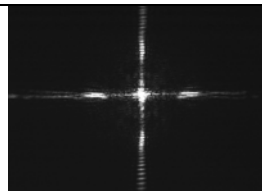
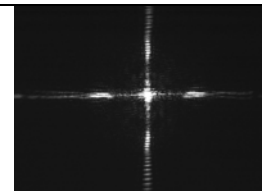
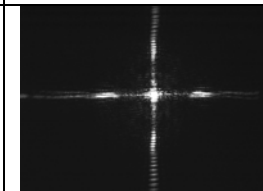
			
$S_3(15) = 0.9801$ $S_3(20) = 0.9678$ OKO Actuator = 0	$S_3(15) = 0.9797$ $S_3(20) = 0.9671$ OKO Actuator = .05	$S_3(15) = 0.9802$ $S_3(20) = 0.9682$ OKO Actuator = -.05	$S_3(15) = 0.9800$ $S_3(20) = 0.9685$ OKO Actuator = -.1
			
$S_3(15) = 0.9804$ $S_3(20) = 0.9694$ OKO Actuator = -.15	$S_3(15) = 0.9806$ $S_3(20) = 0.9697$ OKO Actuator = -.2	$S_3(15) = 0.9811$ $S_3(20) = 0.9705$ OKO Actuator = -.25	<b><math>S_3(15) = 0.9812</math></b> <b><math>S_3(20) = 0.9710</math></b> OKO Actuator = -.3
			
$S_3(15) = 0.9809$ $S_3(20) = 0.9709$ OKO Actuator = -.35	$S_3(15) = 0.9806$ $S_3(20) = 0.9711$ OKO Actuator = -.4	$S_3(15) = 0.9805$ $S_3(20) = 0.9712$ OKO Actuator = -.45	$S_3(15) = 0.9803$ $S_3(20) = 0.9711$ OKO Actuator = -.5

TABLE 8.15: Closed-loop images of the high frequency object using sharpness metric  $S_3$ . Mask sizes of 15 and 20 pixels were used.

## 8.7 Conclusions

In this chapter the performance of all five sharpness metrics in a coherent imaging system was investigated. It was seen that the image plane metrics  $S_{i2}$ ,  $S_1$ , and  $S_2$  were successful for all object types. The Fourier-based metrics  $S_1$  and  $S_2$  were more robust and sensitive than the intensity squared metric  $S_{i2}$  with the  $S_2$  metric being the more sensitive of the two. The Fourier transforming property of a single lens was used for the

sharpness metrics  $S_3$  and  $S_4$  where the Fourier transform was found optically and the Fourier plane was used to calculate the sharpness value. These two metrics were successful with the extended bar chart and star pattern objects but failed with the circular objects. The more detail and high spatial frequencies the object contained the more sensitive these two metrics were.

After comparison with defocus, higher-order aberrations were added to see the affect on the sharpness metric performance. For the image plane sharpness metrics the Fourier-based metrics  $S_1$  and  $S_2$  where successful where the intensity squared  $S_{i2}$  metric failed for several objects. The  $S_3$  and  $S_4$  sharpness metrics were successful with extended objects but not with the circular objects due to the motion of the optical axis and high order aberrations were added.

Finally the sharpness metrics were implemented into a preliminary, manual, closed-loop system. The system successfully arrived at the sharp image and shows promise for use in full higher frequency closed-loop systems run with search algorithm.



## CHAPTER 9: CONCLUSIONS

### 9.1 Discussion

Four novel Fourier-based sharpness metrics were introduced and investigated in this dissertation. For the sharpness metrics,  $S_1$  and  $S_2$ , the Fourier transform was performed digitally from the image plane image and therefore can be used in both incoherent and coherent imaging systems. Metrics  $S_3$  and  $S_4$  can only be used in a coherent imaging system because the Fourier transform found optically using a single lens. All metrics were compared to the intensity squared,  $S_{i2}$ , metric that is most commonly used in image sharpening.

Investigation of the performance of these metrics consisted of measuring and plotting the sharpness value versus changing aberration strength. Defocus was first applied to the system and the metrics were compared before applying higher order aberrations including astigmatism, coma, and spherical aberrations. It was found that all Fourier-based metrics showed very promising results, especially for extended objects. The Fourier-based metrics were successful to produce an absolute or local maximum when the wavefront error for all cases except using metrics  $S_3$  and  $S_4$  on circular objects. Metrics  $S_3$  and  $S_4$  failed for circular objects because adding aberrations caused the optical axis to shift and the Fourier plane location to move along the optical axis. This motion of the Fourier distribution compared to a stationary mask caused the masked portion to change and produce inaccurate sharpness values. For extended objects  $S_3$  and  $S_4$  were

successful because the DC term was masked out and the remaining high spatial frequencies were unaffected by the mask motion. In many cases the Fourier-based metrics were successful where the intensity squared,  $S_{i2}$  metric failed. A summary of all the metrics can be seen in table 9.1.

When selecting a mask size for the  $S_2$ ,  $S_3$ , and  $S_4$  metrics the key is to mask out the DC term so that it is more sensitive to the changes in high spatial frequencies. Mask size selection is also limited by the object contrast and optical system resolution. The sharpness metrics performed with success in a manual closed-loop correction system. These results show great promise for the use of the Fourier-based sharpness sensors in an adaptive optics system.

## 9.2 Future Work

The accuracy of the  $S_3$  metric can be increased by tracking the center of the Fourier distribution and causing the digital mask to move as the optical axis moves so that the mask is always located at the center of the Fourier distribution. In the same sense the accuracy of the  $S_4$  metric can be improved by creating a mechanical system so that the physical mask moves as the optical axis moves so that the mask is always centered as aberrations change. Improving the physical mask so that it is more opaque and defined will also improve the performance of the  $S_4$  metric.

Future work entails the implementation of these sharpness metrics in an automatic closed-loop system. This requires interfacing the components with the computer and the development and application of a search algorithm.

Metric	Camera Location	Light Source	Fourier Transform Method	Masking Method	Time (s)	Standard Deviation	Comments
$S_2 = \frac{\iint I_i^2(x, y) dx dy}{\left(\iint I_i(x, y) dx dy\right)^2}$	Image Plane	Coherent or Incoherent	N/A	N/A	4.04	2.65	Successful for most objects. Failed with incoherent and coherent point sources.
$S_1 = \frac{\iint  \mathcal{F}(I_i(x, y))  df_x df_y}{\iint I_i(x, y) dx dy}$	Image Plane	Coherent or Incoherent	Digitally	N/A	4.40	1.76	Successful for all objects except coherent point sources.
$S_2 = \frac{\sum  \mathcal{F}(I_i(x, y)) _{masked}}{\sum  \mathcal{F}(I_i(x, y)) _{unmasked}}$	Image Plane	Coherent or Incoherent	Digitally	Digitally	4.56	1.59	Successful for all objects, both incoherent and coherent
$S_3 = \frac{\sum  \mathcal{F}(U_i(x, y)) _{masked}^2}{\sum  \mathcal{F}(U_i(x, y)) _{unmasked}^2}$	Fourier Plane	Coherent Only	Optically	Digitally	4.12	0.98	Successful for all extended objects but failed for circular objects.
$S_4 = \frac{\sum I(x, y)_{\text{sharp}}}{\sum I(x, y)}$	Two cameras at image planes	Coherent Only	N/A	Physically	< 1	N/A	Successful for all extended objects but failed for circular objects.

TABLE 9.1: Summary and comparison of all sharpness metrics.

## REFERENCES

- <sup>1</sup> B. L. McGlamery, "Restoration of turbulence-degraded images," *J. Opt. Soc. Am.* **57**, 293-297 (1967).
- <sup>2</sup> R. K. Tyson, *Introduction to Adaptive Optics*, SPIE Press, Bellingham, WA (2000).
- <sup>3</sup> R. K. Tyson, *Principles of Adaptive Optics*, 2<sup>nd</sup> Edition, Academic, Boston (1998).
- <sup>4</sup> J. H. Hardy, *Adaptive Optics for Astronomical Telescopes*, Oxford University Press, New York (1998).
- <sup>5</sup> F. Roddier, *Adaptive Optics in Astronomy*, Cambridge University Press, (1999).
- <sup>6</sup> E. Kibblewhie and W. Wild, *Adaptive Optics*, Wiley, New York (2007).
- <sup>7</sup> D. P. Greenwood and D. L. Fried, "Power spectra requirements for wave-front compensative systems," *J. Opt. Soc. Am.* **66**, 193-206 (1976).
- <sup>8</sup> D. P. Greenwood, "Bandwidth specification for adaptive optics systems," *J. Opt. Soc. Am.* **67**, 390-393 (1977).
- <sup>9</sup> G. A. Tyler, "Bandwidth considerations for tracking through turbulence," *J. Opt. Soc. Am. A*, **11**, 358-367 (1994).
- <sup>10</sup> R. K. Tyson and B. W. Frazier, *Field Guide to Adaptive Optics*, SPIE Press, Bellingham, WA (2004).
- <sup>11</sup> H. W. Babcock, "The Possibility of Compensating Astronomical Seeing," *Publ. Astro. Soc. Pac.* **65**, 229-236 (1953).
- <sup>12</sup> W. B. Bridges, P. T. Brunner, S. P. Lazzara, T. A. Nussmeier, T. R. O'Meara, J. A. Sanguinet, and W. P. Brown Jr., "Coherent Optical Adaptive Techniques," *App. Opt.* **13**, 291-300 (1974).
- <sup>13</sup> J. E. Pearson, W. B. Bridges, S. Hansen, T. A. Nussmeier, and M. E. Pedinoff, "Coherent optical adaptive techniques: design and performance of an 18-element visible multidither COAT system," *App. Opt.* **15**, 611-621 (1976).
- <sup>14</sup> J. E. Pearson, "Atmospheric turbulence compensation using coherent optical adaptive techniques," *App. Opt.* **15**, 622-631 (1976).
- <sup>15</sup> C. L. Hayes, R. A. Brandewie, W. C. Davis, and G. E. Mevers, "Experimental test of an infrared phase conjugation adaptive array," *J. Opt. Soc. Am.* **67**, 269-277 (1977).

- <sup>16</sup> J. W. Hardy, J. E. Lefebvre, and C. L. Koliopoulos, "Real-time atmospheric compensation," *J. Opt. Soc. Am.* **67**, 360-369 (1977).
- <sup>17</sup> R. A. Muller and A. Buffington, "Real-time correction of atmospherically degraded telescope images through image sharpening," *J. Opt. Soc. Am.* **64**, 1200-1210 (1974).
- <sup>18</sup> A. Buffington, F. S. Crawford, R. A. Muller, A. J. Schwemin, and R. G. Smits, "Correction of atmospheric distortion with an image-sharpening telescope," *J. Opt. Soc. Am.* **67**, 298-303 (1977).
- <sup>19</sup> J. W. Hardy, "Adaptive optics – a progress review," *Proc. SPIE* **1542**, 2-17 (1991).
- <sup>20</sup> C. A. Primmerman, D. V. Murphy, D. A. Page, B. G. Zollars, and H. T. Barclay, "Compensation of atmospheric turbulence optical distortion using a synthetic beacon," *Nature (London)*, **353**, 141-143 (1991).
- <sup>21</sup> R. Q. Fugate, D. L. Fried, G. A. Ameer, B. R. Boeke, S. L. Browne, P. H. Roberts, R. E. Ruane, and L. M. Wopat, "Measurement of atmospheric wavefront distortion using scattered light from a laser guide star," *Nature (London)*, **353**, 144-146 (1991).
- <sup>22</sup> J. W. Hardy, "Active Optics: A new technology for the control of light," *Proc. IEEE*, **66**, 651-697 (1978).
- <sup>23</sup> H. W. Babcock, "Adaptive Optics Revisited," *Science*, **249**, 253-257 (1990).
- <sup>24</sup> D. P. Greenwood and C. A. Primmerman, "The history of adaptive-optics development at the MIT Lincoln Laboratory," *Proc. SPIE*, **1920**, 220-234 (1993).
- <sup>25</sup> R. K. Tyson, "Adaptive Optics compensation of atmospheric turbulence: the past, the present, and the promise," *Proc. SPIE*, **2222**, 404-412 (1994).
- <sup>26</sup> R. Benedict, Jr., J. B. Breckinridge, and D. L. Fried, "Atmospheric-Compensation Technology: Introduction to the feature issue," *J. Opt. Soc. Am. A*, **11**, 257-260 (1994).
- <sup>27</sup> J. A. Perreault and A. Wirth, "Survey of Adaptive Optic Techniques," *Proc. SPIE*, **5903**, 55-62 (2005).
- <sup>28</sup> A. Greenaway, "Adaptive Optics: Astronomy and Beyond," *Optics & Photonics News*, **17**, 22-27 (2006).
- <sup>29</sup> L. C. Andrews and R. L. Phillips, *Laser Beam Propagation through Random Media*, SPIE Press, Bellingham, WA (1998).
- <sup>30</sup> R. K. Tyson, "Adaptive optics and ground-to-space laser communications," *App. Opt.* **35**, 3640-3646 (1996).

- <sup>31</sup> B. M. Levine, E. A. Martinsen, A. Wirth, A. Jankevics, M. Toledo-Quinones, F. Landers, and T. L. Bruno, "Horizontal line-of-sight turbulence over near-ground paths and implications for adaptive optics correction in laser communications," *App. Opt.* **37**, 4553-4560 (1998).
- <sup>32</sup> R. K. Tyson, "Bit-error rate for free-space adaptive optics laser communications," *J. Opt. Soc. Am. A*, **19**, 753-758 (2002).
- <sup>33</sup> J. Liang, B. Grimm, S. Goelz, and J. F. Bille, "Objective measurement of wave aberrations of the human eye with use of a Hartmann-Shack wave-front sensor," *J. Opt. Soc. Am. A*, **11**, 1949-1957 (1994).
- <sup>34</sup> J. Liang and D. R. Williams, "Aberrations and retinal image quality of the normal human eye," *J. Opt. Soc. Am. A*, **14**, 2873-2883 (1997).
- <sup>35</sup> J. Liang, D. R. Williams, and D. T. Miller, "Supernormal vision and high-resolution retinal imaging through adaptive optics," *J. Opt. Soc. Am. A*, **14**, 2884-2892 (1997).
- <sup>36</sup> A. Roorda, F. Romero-Borja, W. J. Donnelly, H. Queener, T. J. Hebert, and M. C. W. Campbell, "Adaptive optics scanning laser ophthalmoscopy," *Opt. Exp.* **10**, 405-412 (2002).
- <sup>37</sup> B. Hermann, E. J. Fernandez, A. Unterhuber, H. Sattmann, A. F. Fercher, W. Drexler, P. M. Prieto, and P. Artal, "Adaptive-optics ultrahigh-resolution optical coherence tomography," *Opt. Lett.* **29**, 2142-2144 (2004).
- <sup>38</sup> J. Carroll, D. C. Gray, A. Roorda, and D. R. Williams, "Recent advances in retinal imaging with adaptive optics," *Optics & Photonics News* **16**, 36-42 (2005).
- <sup>39</sup> J. Porter, H. Queener, J. Lin, K. Thorn, and A. A. S. Awwal, *Adaptive Optics for Vision Science: Principles, Practices, Design, and Applications*, John Wiley & Sons, Hoboken, NJ (2006).
- <sup>40</sup> M. J. Booth, "Adaptive optics in microscopy," *Phil. Trans. R. Soc. A*, **365**, 2829-2843 (2007).
- <sup>41</sup> O. Albert, L. Sherman, G. Mourou, and T. B. Norris, "Smart microscope: an adaptive optics learning system for aberration correction in multiphoton confocal microscopy," *Opt. Lett.* **25**, 52-54 (2000).
- <sup>42</sup> M. A. A. Neil, R. Juškaitis, M. J. Booth, T. Wilson, T. Tanaka, and S. Kawata, "Adaptive aberration correction in a two-photon microscope," *J. Microscopy*, **200**, 105-108 (2000).
- <sup>43</sup> L. Sherman, J. Y. Ye, O. Albert, and T. B. Norris, "Adaptive correction of depth-induced aberrations in multiphoton scanning microscopy using a deformable mirror," *J. Microscopy*, **206**, 65-71 (2002).

- <sup>44</sup> P. N. Marsh, D. Burns, and J. M. Girkin, "Practical implementation of adaptive optics in multiphoton microscopy," *Opt. Exp.* **11**, 1123-1130 (2003).
- <sup>45</sup> M. Rueckel, J. A. Mack-Bucher, and W. Denk, "Adaptive wavefront correction in two-photon microscopy using coherence-gated wavefront sensing," *Proc. Natl. Acad. Sci.* **103**, 17137-17142 (2006).
- <sup>46</sup> M. J. Booth, M. A. A. Neil, R. Juskaitis, and T. Wilson, "Adaptive aberration correction in a confocal microscope," *Proc. Natl. Acad. Sci.* **99**, 5788-5792 (2002).
- <sup>47</sup> A. J. Wright, D. Burns, B. A. Patterson, S. P. Poland, G. J. Valentine, and J. M. Girkin, "Exploration of the Optimisation Algorithms used in the Implementation of Adaptive Optics in Confocal and Multiphoton Microscopy," *Microsc. Res. and Tech.* **67**, 36-44 (2005).
- <sup>48</sup> B. Potsaid, Y. Bellouard, and J. T. Wen, "Adaptive Scanning Optical Microscope (ASOM): A multidisciplinary optical microscope design for large field of view and high resolution imaging," *Opt. Exp.* **13**, 6504-6518 (2005).
- <sup>49</sup> M. A. A. Neil, M. J. Booth, and T. Wilson, "New modal wave-front sensor: a theoretical analysis," *J. Opt. Soc. Am. A*, **17**, 1098-1107 (2000).
- <sup>50</sup> M. J. Booth, M. A. A. Neil, and T. Wilson, "New modal wave-front sensor: application to adaptive confocal fluorescence microscopy and two-photon excitation fluorescence microscopy," *J. Opt. Soc. Am. A*, **19**, 2112-2120 (2002).
- <sup>51</sup> M. Feierabend, M. Ruckel, and W. Denk, "Coherence-gated wave-front sensing in strongly scattering samples," *Opt. Lett.* **29**, 2255-2257 (2004).
- <sup>52</sup> M. A. A. Neil, R. Juškaitis, M. J. Booth, T. Wilson, T. Tanaka, and S. Kawata, "Active Aberration Correction for the Writing of Three-Dimensional Optical Memory Devices," *App. Opt.* **41**, 1374-1379 (2002).
- <sup>53</sup> M. Schwertner, M. J. Booth, and T. Wilson, "Adaptive optics for microscopy, optical data storage and micromachining," *Proc. SPIE*, **6306**, 63060A (2006).
- <sup>54</sup> E. Theofanidou, L. Wilson, W. J. Hossack, and J. Arlt, "Spherical aberration correction for optical tweezers," *Opt. Comm.* **236**, 145-150 (2004).
- <sup>55</sup> K. D. Wulff, D. G. Cole, R. L. Clark, R. DiLeonardo, J. Leach, J. Cooper, G. Gibson, and M. J. Padgett, "Aberration correction in holographic optical tweezers," *Opt. Exp.* **14**, 4169-4174 (2006).
- <sup>56</sup> F. Gonte, A. Courteville, and R. Dandliker, "Optimization of single-mode fiber coupling efficiency with an adaptive membrane mirror," *Opt. Eng.* **41**, 1073-1076 (2002).
- <sup>57</sup> R. J. Noll, "Zernike polynomials and atmospheric turbulence," *J. Opt. Soc. Am.* **66**, 207-211 (1976).

- <sup>58</sup> M. Born and E. Wolf, *Principles of Optics*, 7<sup>th</sup> Edition, Cambridge University Press, Cambridge (1999).
- <sup>59</sup> J. M. Geary, *Introduction to Wavefront Sensors*, SPIE Press, Bellingham, WA (1995).
- <sup>60</sup> F. Roddier, "Curvature sensing and compensation: a new concept in adaptive optics," *App. Opt.* **27**, 1223-1225 (1988).
- <sup>61</sup> R. Ragazzoni, "Pupil plane wavefront sensing with an oscillating prism," *J. Modern Opt.* **43**, 289-293 (1996).
- <sup>62</sup> R. A. Gonsalves, "Phase retrieval by differential intensity measurements," *J. Opt. Soc. Am. A*, **4**, 166-170 (1987).
- <sup>63</sup> G. D. Love, "Wavefront correction and production of Zernike modes with a liquid crystal spatial light modulator," *App. Opt.* **36**, 1517-1524 (1997).
- <sup>64</sup> J. Gourlay, G. D. Love, P. M. Birch, R. M. Sharples, and A. Purvis, "A real-time closed-loop liquid crystal adaptive optics system: first results," *Opt. Comm.* **137**, 17-21 (1997).
- <sup>65</sup> M. Yellin, "Using membrane mirrors in adaptive optics," *Proc. SPIE*, **75**, 97 (1976).
- <sup>66</sup> R. P. Grosso and M. Yellin, "The membrane mirror as an adaptive optical element," *J. Opt. Soc. Am.* **67**, 399-406 (1977).
- <sup>67</sup> L. M. Miller, W. J. Kaiser, T. W. Kenny, M. L. Agronin, and R. L. Norton, "Fabrication and characterization of a micromachined deformable mirror for adaptive optics applications," *Proc. SPIE*, **1954**, 421-430 (1993).
- <sup>68</sup> G. V. Vdovin and P. M. Sarro, "Flexible mirror micromachined in silicon," *App. Opt.* **34**, 2968-2972 (1995).
- <sup>69</sup> G. V. Vdovin, P. M. Sarro, and S. Middelhoek, "Technology and applications of micromachined adaptive mirrors," *J. Micromech. Microeng.* **9**, R8-R20 (1999).
- <sup>70</sup> W. J. Smith, *Modern Optical Engineering*, 3<sup>rd</sup> Edition, McGraw-Hill, New York, (2000).
- <sup>71</sup> V. N. Mahajan, "Strehl ratio for primary aberration: some analytical results for circular and annular pupils," *J. Opt. Soc. Am.* **72**, 1258-1266 (1982).
- <sup>72</sup> J. P. Hamaker, J. D. O'Sullivan, and J. E. Noordam, "Image sharpness, Fourier optics, and redundant-spacing interferometry," *J. Opt. Soc. Am.* **67**, 1122-1123 (1977).



- <sup>73</sup> M. C. Roggemann, C. A. Stoudt, and B. M. Welsh, "Image-spectrum signal-to-noise-ratio improvements by statistical frame selection for adaptive-optics imaging through atmospheric turbulence," *Opt. Eng.* **33**, 3254-3264 (1994).
- <sup>74</sup> M. A. Vorontsov, G. W. Carhart, D. V. Pruidze, J. C. Ricklin, and D. G. Voelz, "Image quality criteria for an adaptive imaging system based on statistical analysis of the speckle field," *J. Opt. Soc. Am. A*, **13**, 1456-1466 (1996).
- <sup>75</sup> J. R. Fienup, "Synthetic-aperture radar autofocus by maximizing sharpness," *Opt. Lett.* **25**, 221-223 (2000).
- <sup>76</sup> J. R. Fienup and J. J. Miller, "Aberration correction by maximizing generalized sharpness metrics," *J. Opt. Soc. Am. A*, **20**, 609-620 (2003).
- <sup>77</sup> J. W. Goodman, *Introduction to Fourier Optics*, McGraw-Hill., New York, (1968).
- <sup>78</sup> E. Abbe,, "Beiträge zur Theorie des Mikroskops und der mikroskopischen Wahrnehmung," *Archiv. Mikroskopische Anat.*, **9**, 413-468 (1873).
- <sup>79</sup> A. B. Porter, "On the Diffraction Theory of Microscope Vision," *Phil. Mag.*, **11(61)**, 154-166 (1906).
- <sup>80</sup> N. Doble, "Image Sharpening Metrics and Search Strategies for Indirect Adaptive Optics" Ph.D. Dissertation, University of Durham (2000).
- <sup>81</sup> L. P. Murray, "Smart Optics: Wavefront sensor-less adaptive optics – Image correction through sharpness maximization," Ph.D. Dissertation, NUI Galway (2007).
- <sup>82</sup> K. Bush, A. Marrs, and M. Schoen, "Electrostatic Membrane Deformable Mirror Characterization and Applications," *Proc. SPIE*, **5894**, 124-138 (2005).